

**Identification of Prostate Cancer Metabolomic Markers by
¹H HRMAS NMR Spectroscopy and
Quantitative Immunohistochemistry**

Dissertation

zur Erlangung des akademischen Grades

Doctor medicinae

an der Medizinischen Fakultät

der Universität Leipzig

eingereicht von:

Franziska Löbel

Geburtsdatum / Geburtsort:

12.02.1985 / Jena

angefertigt in:

Leipzig

Einrichtung:

Medizinische Fakultät der Universität Leipzig

Institut für Medizinische Physik und Biophysik

Betreuer:

Prof. Dr. Daniel Huster

Beschluss über die Verleihung des Doktorgrades vom:

24.03.2015

Bibliographische Beschreibung

Löbel, Franziska

Identification of Prostate Cancer Metabolomic Markers by ^1H HRMAS NMR Spectroscopy and Quantitative Immunohistochemistry

Universität Leipzig, Dissertation

98 S.¹, 112 Lit.², 40 Abb.³, 11 Tab.⁴, 3 Anl.⁵

Referat:

Die vorliegende Studie präsentiert und evaluiert einen diagnostischen Ansatz zur quantitativen Bestimmung von metabolischen Markern von Prostatakrebs, basierend auf der Durchführung von " ^1H High Resolution Magic Angle Spinning Nuclear Magnetic Resonance Spectroscopy" (^1H HRMAS NMR Spektroskopie) und quantitativer Immunhistochemie.

Durch Untersuchung von Gewebeproben von Prostatakrebspatienten mittels ^1H HRMAS NMR Spektroskopie und anschließender Korrelation der Ergebnisse mit quantitativ bestimmten Resultaten immunhistochemischer Färbeverfahren können die Metaboliten Phosphocholin und Ziträt in der vorliegenden Patientenkohorte als potentielle metabolische Marker von Prostatakrebs identifiziert werden. Eine Validierung der vorgestellten diagnostischen Methode erfolgt durch vergleichende Analysen qualitativer und quantitativer konventioneller histopathologischer Untersuchungen.

Die Anwendung des präsentierten diagnostischen Ansatzes erfolgt zusätzlich zur Bestimmung von potentiellen metabolischen Markern von rezidivierenden Prostatakrebskrankungen.

¹ Seitenzahl insgesamt

² Zahl der im Literaturverzeichnis ausgewiesenen Literaturangaben

³ Anzahl der in der Arbeit veröffentlichten Abbildungen

⁴ Gesamtanzahl der abgebildeten Tabellen

⁵ Anzahl der Anhänge

Part of this work was presented at the “Annual meeting of the Society for European Magnetic Resonance in Medicine and Biology (ESMRMB)” in Lisbon, October 2012

Table of Contents

Table of Contents	3
Glossary.....	5
1 Introduction.....	7
1.1 Prostate Cancer.....	7
1.2 Detection of Prostate Cancer – State of the Art.....	7
1.2.1 Prostate- Specific Antigen Test and Digital Rectal Examination.....	8
1.2.2 Radiographic Methods in PCa Detection	8
1.2.3 Transrectal Core Biopsies and Histopathological Analysis.....	10
1.2.4 Histopathological Grading of Prostate Cancer: GLEASON Score	11
1.3 Challenges and Need for New Approaches in PCa Diagnostic Management	12
2 Scientific Background I: Nuclear Magnetic Resonance, ¹ H HRMAS NMR Spectroscopy and Metabolomic Profiles	13
2.1 Nuclear Magnetic Resonance	13
2.1.1 Spin Precession.....	15
2.1.2 Magnetic Resonance.....	16
2.1.3 Chemical Shift and J- coupling	16
2.2 Nuclear Magnetic Resonance Spectroscopy.....	19
2.2.1 Magic Angle Spinning and ¹ H HRMAS NMR Spectroscopy	19
2.2.2 MAS Spinning Rates and Spinning Side Bands.....	20
2.3 Metabolomics, Metabolite Profiles and Clinical Utility.....	22
3 Scientific Background II: Immunohistochemistry of Prostate Cancer	26
4 Aims of the Study.....	29
5 Material and Methods.....	31
5.1 Prostate Tissue Samples and Patient Demographics	31
5.2 ¹ H HRMAS NMR Spectroscopy	31
5.2.1 Sample Preparation.....	32
5.2.2 Spectroscopy Scan.....	32
5.2.3 Data Processing	33
5.3 Immunohistochemistry	37
5.3.1 Immunohistochemistry Material and Equipment	37
5.3.2. Immunohistochemistry Protocol	37
5.3.3 Prostate Immunomarker Stability after ¹ H HRMAS NMR Spectroscopy.....	41
5.3.4 Qualitative IHC Analysis	42
5.3.5 Quantitative IHC Analysis	43

5.3.5.1	Quantitative IHC Slide Review	43
5.3.5.2	Computer-Automated Quantitative IHC Analysis	43
5.3	Quantitative Histopathology	49
5.4	Identification of Prostate Cancer Metabolomic Markers	50
5.5	Patient Outcomes and Recurrence Categories	50
5.6	Statistical Analysis	51
6	Results	52
6.1	Patient demographics	52
6.2	Spectroscopy Results	53
6.3	Immunohistochemistry	56
6.3.1	Evaluation of Prostate Immunomarker Stability after ¹ H HRMAS MRS	56
6.3.2	Qualitative Immunohistochemistry	59
6.4	Quantitative Immunohistochemistry	65
6.4.1	Quantitative IHC Slide Review	65
6.4.2	Computer-Automated Quantitative IHC Evaluation using QIAP	67
6.5	Quantitative Histopathology	69
6.6	Identification of Prostate Cancer Metabolomic Markers using QIAP	72
6.7	Patient Outcomes and Recurrence	74
7	Discussion	77
8	Summary / Abstract	86
9	Zusammenfassung	89
10	References	92
11	Erklärung über die eigenständige Abfassung der Arbeit	99
12	Danksagung	100
13	Lebenslauf und Publikationsverzeichnis	101
Appendix	103
A.1	Immunostaining protocols	103
A.2	Spectral Intensities Measured by ¹ H HRMAS MRS in 51 Samples	105
A.3	Graphs for Correlations of Spectral Intensities and CaE% determined by QIAP in 34 Additional Regions of Interest	110

Glossary

ABC	Avidin-Biotin-Peroxidase-Complex
ADC	Apparent diffusion coefficient
ADT	Androgen deprivation therapy
Ala	Alanine
AMACR	Alpha-Methylacyl-CoA-Racemase
BCIP	5-Bromo-4-chloro-3-indolyl phosphate
BPH	Benign Prostate Hyperplasia
Cit	Citrate
CK	Cytokeratin
CPMG	Carr- Purcell-Meiboom-Gill pulse sequence
Cr	Creatine
DAB	3,3'-Diaminobenzidine
DANTE	Delay alternating with nutation for tailored excitation
DAPI	4',6-Diamidino-2-phenylindole
DER	Digital Rectal Examination
EDTA	Ethylenediaminetetraacetic acid
FID	Free induction decay
FLAIR	Fluid attenuated inversion recovery
fMRI	Functional Magnetic Resonance Imaging
GBM	Glioblastoma multiforme
GC-MS	Gas-chromatography mass spectrometry
GPC	Glycerophosphocholine
GS	Gleason score
H&E	Hematoxlin & Eosin
HIER	Heat Induced Epitope Retrieval
HMWCK	High Molecular Weight Cytokeratin
HRMAS	High Resolution Magic Angle Spinning
IHC	Immunohistochemistry
IRB	Institutional Review Board
Lac	Lactate
LC-MS	Liquid-chromatography mass spectrometry
MAS	Magic Angle Spinning

MGH	Massachusetts General Hospital
MRI	Magnetic Resonance Imaging
MRS	Nuclear Magnetic Resonance Spectroscopy
NBT	Nitro blue tetrazolium chloride
NMR	Nuclear Magnetic Resonance
OS	Overall survival
PBS	Phosphate Buffered Saline
Pcho	Phosphocholine
PCa	Prostate Cancer
PIER	Proteolytic Induced Epitope Retrieval
PIN	Prostate Intraepithelial Neoplasia
PSA	Prostate Specific Antigen
QIAP	Quantitative Immunohistochemistry Analysis Program
SD	Standard deviation
SSB	Spinning side bands
T1	Spin-lattice relaxation time
T2	Spin-spin relaxation time
TE	Transient Echo
TMS	Trimethylsilan
TRIS	Trisaminomethane
TRUS	Transrectal Ultrasound Guided Biopsy

1 Introduction

1.1 Prostate Cancer

Prostate cancer (PCa) is the most frequently diagnosed malignant disease among adult males in the USA and the second leading cause of cancer-related deaths in men [1]. Worldwide, the 5-year prevalence of PCa has been calculated at more than 3.9 million cases [2]. The distribution of incidence is very heterogeneous and highest rates are found in industrialized countries, especially of Northern America, Western and Northern Europe and Australia. With 233,000 newly diagnosed cases and about 29,480 cancer associated deaths among males in the USA estimated for 2013, PCa presents a tremendous and significant health problem [1]. The lifetime risk of developing PCa for American men is approximately 15%. However, autopsies have revealed microscopic prostate carcinomas in up to 29% in the age group of 30- 40 year old men and 64% in age group 60- 70 years. At 80 years of age, as many as 80% of all men show small carcinomas [3]. The risk of developing PCa is known to be related to genetic factors, diet, lifestyle and androgens. Furthermore, studies indicated that infection or inflammation of the prostate may also trigger PCa development and that environmental carcinogens might promote PCa progression [3]. High risk groups have been identified within the population, including African Americans as well as men with one or more first-degree relatives diagnosed with PCa at an early age [1].

Histology indicates that more than 95% of PCas are unevenly distributed, epithelially derived adenocarcinomas of which more than 75% are located in the peripheral zone, 10-15% in the transition zone and less than 15% in the central zone of the prostate [4]. This cancer tends to metastasize to the bones, especially the lumbar spine, pelvis and femur. Bone metastases can be found in up to 70% of patients with advanced PCa [5]. In general, this malignancy is characterized by a relatively slow growth rate of the primary tumor, compared to malignant transformations of other organs [6]. Given the mostly indolent clinical behavior of PCa, an early and accurate diagnosis is crucial, in order to provide an adequate treatment for this highly prevalent disease.

1.2 Detection of Prostate Cancer – State of the Art

The detection of PCa according to the screening guidelines of the American Cancer Society includes a serum Prostate-Specific Antigen (PSA) test and annual Digital Rectal Examination (DRE) for men older than 50 years. High risk groups are subjected to earlier screening tests at

an age of 45 years [7]. Clinical tools that are administered to symptomatic patients in order to detect PCa are transrectal ultrasound (TRUS) and, less frequently, Magnetic Resonance Imaging (MRI) [4]. The gold standard of modern PCa diagnosis, however, is the histopathological examination of transrectal ultrasound-guided core biopsies [8].

1. 2. 1 Prostate- Specific Antigen Test and Digital Rectal Examination

Despite the high prevalence of PCa in the USA, the 5-year relative survival rate for localized or locally advanced disease is nearly 100% [7]. This is mainly due to the development of prostate-specific antigen (PSA) screening tests in the 1990s, which resulted in a remarkable increase in the incidence of early diagnosed PCas [9]. PSA is a glycoprotein produced by the cells of the prostate gland and added to the ejaculate, where it functions as a liquefier of the semen. Although there is no true PSA cut-off point distinguishing cancer from non-cancerous conditions, an elevated level of PSA (> 4 ng/ml) in the serum has been shown to correlate with the occurrence of PCa. However, while PSA is prostate specific, it is not cancer specific: benign prostate hyperplasia (BPH) and prostatitis are conditions that are known to increase serum PSA levels, thereby leading to diagnostic uncertainty [10, 11]. While significantly increasing the number of early PCa diagnoses, the PSA screening lacks the ability to distinguish more aggressive and malignant tumors from indolent cases, leading to overdiagnosis and overtreatment [12, 13]. Even though studies indicated that PSA-based screening might reduce mortality rates [14, 15], recent systematic reviews failed to find significant evidence for that [16].

DRE, a routine clinical method used to screen for suspicious prostate structures, is another insufficient diagnostic tool, due to its lack of specificity and high investigator-dependence. Benign conditions, such as BPH, can cause abnormal test results, leading to further diagnosis and, oftentimes, unnecessary intervention. Only about 25-50% of abnormal findings in DRE can ultimately be verified as PCa [10].

1.2.2 Radiographic Methods in PCa Detection

Radiographic methods for PCa diagnostics are commonly conducted on patients with elevated PSA levels and abnormal findings in DRE.

Magnetic Resonance Imaging (MRI) represents a non-invasive approach to obtain images of anatomical structures in the prostate. For that, the patient is placed in a large superconducting magnet- the MRI scanner- at field strengths of 1.5 or 3 Tesla. A combination of pelvic and

endorectal coils is used for induction of a current that can then be translated into anatomical images. More detailed information on the scientific background of magnetic resonance is illustrated in Chapter 2. Cancerous prostate tissue is typically assessed using conventional MRI sequences, such as T2-weighted (spin-spin relaxation time) imaging and T1-weighted (spin-lattice relaxation time) sequences before and after the injection of a gadolinium-based contrast agent (Figure 1). Due to an increase of cell density in pathologic cells and a consecutive decrease in water content, prostate cancer tissue appears with decreased signal intensity on T2-weighted imaging.

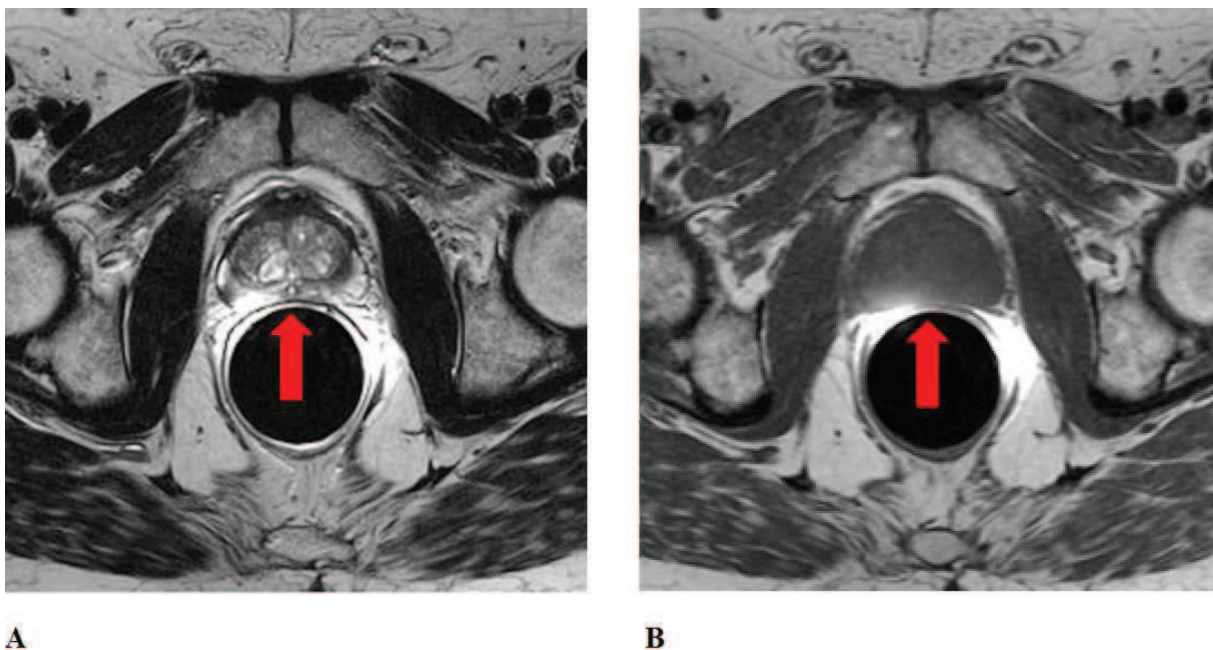


Figure 1: MRI scans of a human prostate with a cancerous lesion: (A) Axial T1-weighted and (B) axial T2-weighted images. The red arrows point at the malignant neoplasm, which is located in the peripheral zone [17].

However, the interpretation of MR images can be biased by non-malignant conditions, and even large tumors ($> 0.5\text{cm}^3$) can be detected by MRI in only approximately 70% [18]. Thus, prostate MRI serves to increase the accuracy of histopathology by identifying a specific target area for biopsy, rather than presenting an alternative diagnostic method [19]. The use of advanced MRI techniques, such as diffusion weighted imaging (DWI), perfusion weighted imaging (PWI) or the use of the apparent diffusion coefficient (ADC) to predict prostate cancer volume, could aid in increasing diagnostic accuracy in the future [20].

Nuclear Magnetic Resonance Spectroscopy (MRS) adds additional information to anatomical imaging by identifying metabolites in biological tissues. Malignant conditions, like PCa, can thus be distinguished from benign conditions due to metabolic changes (Figure 2). However,

none of these technologies fully reveal the extent of prostate cancer. At present, the focus shifts to multi-parametrical imaging to improve the diagnostic sensitivity and specificity. The evaluation and interpretation of these data sets depend on the contributions of expert radiologists and MRI scientists. Novel objective radiological methods that can be employed for routine diagnostics in a clinical setting are highly needed.

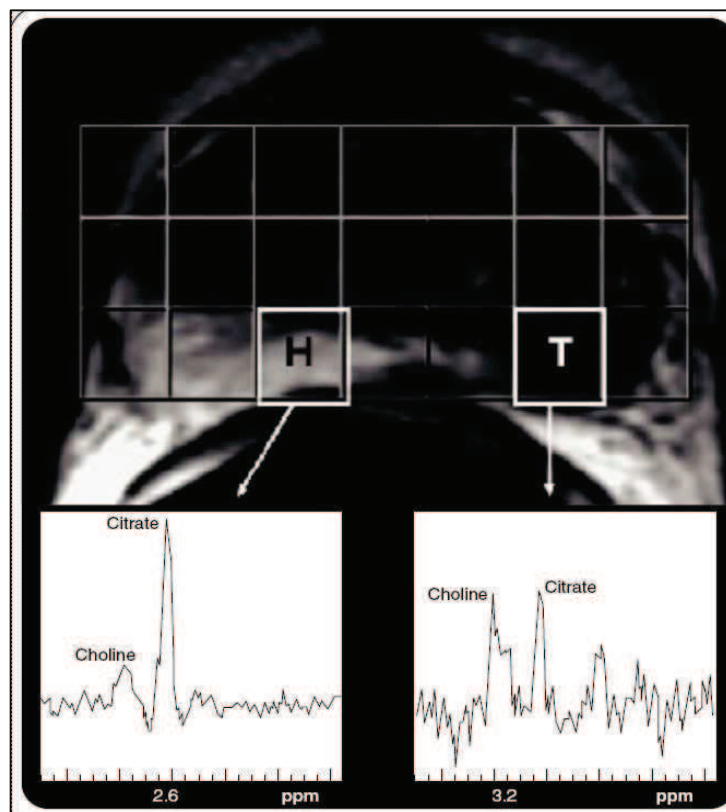


Figure 2: Magnetic resonance spectroscopy of a prostate cancer. The left panel (H) shows a spectrum acquired from the right peripheral zone with a prominent citrate peak and relatively low choline signal, indicative of healthy tissue. The right panel (T) shows a reduced citrate signal and an increase in choline in tumor tissue of the left peripheral zone [21].

1.2.3 Transrectal Core Biopsies and Histopathological Analysis

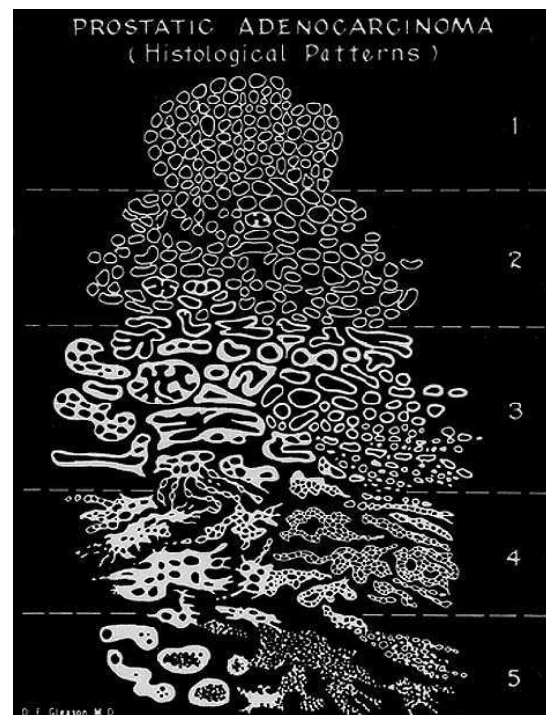
The gold standard of modern PCa detection is the performance of transrectal ultrasound-guided biopsies (TRUS) with subsequent histopathological analysis of the obtained tissue samples. This invasive method, first described in 1937 by Astraldi [22], is conducted to confirm suspicious findings in the clinical tests, such as elevated levels of PSA or an abnormal DRE. For initial biopsies, an ultrasound probe is inserted through the lining of the rectum to guide several small needles through the rectum wall into suspicious areas of the prostate. Traditionally, six or twelve tissue cores are obtained in one intervention [10].

Unfortunately, this method shows low sensitivity, a high sampling error and high false-negative rates, detecting PCa in only 22-34% of the initial biopsy [23, 24]. For the histopathological evaluation of core biopsies, the GLEASON score is used and will be further described in the subsequent section.

1.2.4 Histopathological Grading of Prostate Cancer: GLEASON Score

The GLEASON score describes a histopathological grading system developed by Donald Gleason, which is used in prostate cancer staging, to determine prognosis and guide therapy[25]. Based on tissue obtained from prostate biopsies or prostatectomies, histological grades are assigned to the most common and second most common patterns that appear in the tissue. Both grades are added to obtain the final GLEASON score. The GLEASON patterns are associated with characteristic features, ranging from well differentiated (Grade 1) to poorly differentiated (Grade 5, Figure 3). The GLEASON grading system is currently the most widely used clinical grading system worldwide. Its clinical importance is due to the fact that the GLEASON score has been shown to be a prognostic marker, found to be closely associated with malignancy, overall survival and recurrence of disease [26, 27].

Grade	Description
1	Tissue closely resembles normal tissue. Prostate glands appear small, well-formed and closely packed.
2	Prostate glands appear well-formed but enlarged and more spaced out.
3	Glands are distinguishable but cells appear darker and begin to invade surrounding tissue.
4	Glands are distinguishable but cells appear darker and begin to invade surrounding tissue.
5	No recognizable glands, sheets of cells.



A

B

Figure 3: The GLEASON score is a histopathological grading system used for PCa staging. Description (A) and illustration (B) of the histological appearance of the GLEASON grades as determined by Donald Gleason 1966 [25, 28].

1.3 Challenges and Need for New Approaches in PCa Diagnostic Management

About 158,000 prostatectomy procedures are performed each year in the USA because of clinical suspicion of PCa [29]. Radical treatment procedures, like prostatectomies, often result in impotence and /or incontinence of urine, causing enormous impact on the quality of life for patients [30].

While routine diagnostic methods, most importantly the PSA screening test, have greatly improved early diagnosis and led to a tremendous increase in early onset of treatment, they are also responsible for a substantial number of unnecessary interventions in a tumor type that often exhibits indolent, slow growth. About 67% of the cancers managed with radical procedures would never have led to the patient's death and, therefore, would not have required such a radical treatment [31-33].

None of the currently available diagnostic tools has the potential to accurately distinguish between highly aggressive and malignant tumors, which require consequent treatment, and indolent low malignant cases, which can be managed by regular observation without reaching clinical significance during the patient's lifetime.

Therefore, new diagnostic methods to determine biological status, malignant potential, and extent of the disease are urgently needed in order to optimize diagnosis and ultimately minimize healthcare costs.

“High Resolution Magic Angle Spinning Nuclear Magnetic Resonance Spectroscopy”

(¹H HRMAS MRS), a method introduced for intact biological tissue analysis in 1996 [34, 35], has proven to be a candidate to address the current challenges present in PCa diagnostics [36]. This method measures metabolomic profiles while preserving tissue architecture for subsequent evaluations of histopathology [37]. To date, metabolomic profiles established by ¹H HRMAS MRS have been evaluated and validated using conventional histopathology as the reference standard. In contrast to conventional histopathology, immunohistochemistry (IHC) presents an objective and observer-independent diagnostic method [38, 39]. Since IHC has the potential to provide more objective, accurate and quantitative measures of tissue pathology than routine histopathology, the present study attempted to establish a novel quantitative and observer-independent diagnostic approach by exploring the potential of prostate cancer immunomarkers to quantify metabolomic profiles established by ¹H HRMAS MRS.

2 Scientific Background I: Nuclear Magnetic Resonance, ¹H HRMAS NMR Spectroscopy and Metabolomic Profiles

2.1 Nuclear Magnetic Resonance

Nuclear magnetic resonance (NMR) describes a physical phenomenon that is based on the fact that several atomic nuclei have intrinsic magnetic moments and can therefore absorb and re-emit electromagnetic radiation when placed in a magnetic field.

All subatomic particles (protons, electrons and neutrons) have an intrinsic quantum mechanical property, the **spin I**. Associated with the spin is a **nuclear angular momentum l** which has the total amplitude of:

$$l_{tot} = \sqrt{I(I + 1)} \frac{h}{2\pi}$$

The constant **h** necessary for the calculation of the nuclear angular momentum is called **Planck's constant** and equals $6.6262 \cdot 10^{-34}$ Js.

If the number of neutrons and protons in an atomic nucleus are both even, the overall nuclear spin I equals 0, as an even number of spins in an atom pair up and cancel each other. However, if either the number of neutrons or protons are odd, a non-vanishing overall spin results, which is either an integer number - if both proton and neutron numbers are odd- or a half-integer number- if the sum of numbers of protons and neutrons is odd. Isotopes with an overall spin have an intrinsic **magnetic moment μ**. The magnetic moment is proportional to the nuclear angular momentum.

$$\mu = l\gamma = mh\gamma$$

The **gyromagnetic ratio γ** is a characteristic constant for each nucleus.

For protons, $\gamma = 2.675 \times 10^8 \text{ s}^{-1}\text{T}^{-1}$.

Without an external magnetic field, a nuclear state with a spin quantum number I is (2I+1) - fold degenerate, which means it has (2I+1) nuclear spin levels with the same energy. Therefore, at thermal equilibrium, the distribution of magnetic moments is completely isotropic, meaning that the number of atoms in each of the states will be equal.

However, if an **external magnetic field B_0** is applied to a nuclear state with an overall spin quantum number I , a splitting into $(2I+1)$ nuclear spin levels with different energy occurs. This phenomenon is called **Zeeman Splitting** or **Zeeman Effect** (Figure 4).

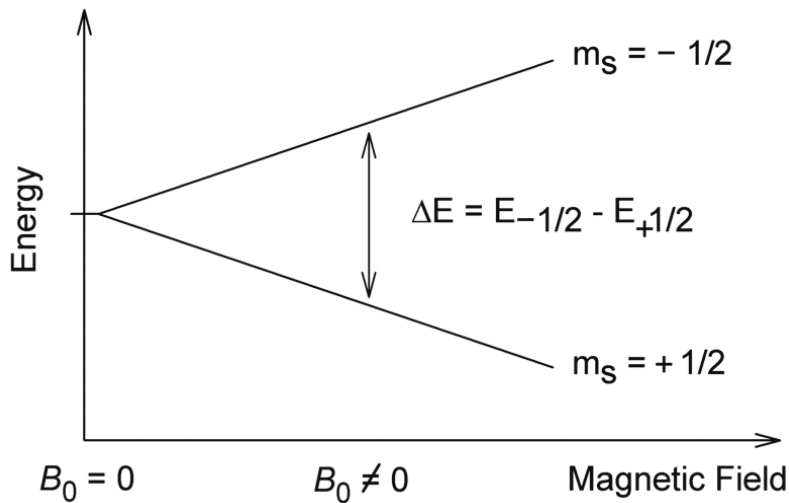


Figure 4: Energy level diagram of a spin $\frac{1}{2}$ in the presence of an external magnetic field. Illustration of the phenomenon of Zeeman-splitting: In an external magnetic field B_0 , a splitting into different nuclear energy levels ($m = \pm 1/2$) occurs for a proton spin [40].

The energy E in each level can be calculated as follows:

$$E = -\gamma \frac{mh}{2\pi} B_0$$

In nuclei with an overall spin I of one-half, like protons (^1H , but also ^{13}C , ^{15}N , ^{19}F and ^{31}P), a Zeeman splitting into two distinct energy levels (nuclear spin levels) occurs:

$$m = \frac{1}{2} \text{ or } m = -\frac{1}{2}.$$

The intrinsic magnetic moment will align either with (parallel) or against (anti-parallel) the magnetic field B_0 . The energetically preferred parallel spin state $m = \frac{1}{2}$ is called **α -state**, while the anti-parallel oriented higher energy level is referred to as **β -state**.

Boltzmann has described the distribution of atoms into the energy states at thermal equilibrium.

The number of atoms N_1 in the anti-parallel state β and N_0 in the parallel state α at a designated temperature T can be calculated through the Boltzmann distribution equation:

$$\frac{N_1}{N_0} = e^{-\frac{\gamma h B_0}{\pi k T}}$$

The **Boltzmann constant** k equals $1.3806 \cdot 10^{-23}$ J/K.

For positive γ , the lower-energy state α is slightly more populated than the higher-energy level β . The sum of the angular momentums creates a macroscopic magnetization, which is used in NMR spectroscopy. The differences in the population of the α and β energy levels is called spin polarization, and represents a necessary requirement for NMR spectroscopy. Higher γ , lower temperature and a greater magnetic field strength B_0 contribute to a greater energy level separation and enhance the sensitivity of the NMR spectra.

2.1.1 Spin Precession

The rotational axis of a spin in an external magnetic field cannot align itself exactly with the direction of the field. Instead, only the z-component of the spin is aligned with the external field B_0 and the x and y components are not defined according to the Heisenberg's uncertainty principle [41]. Consequently, the field exerts a torque on the magnetic moment of a spin, causing it to move around the field on a cone in a constant angle between the magnetic moment and the external magnetic field (Figure 5).

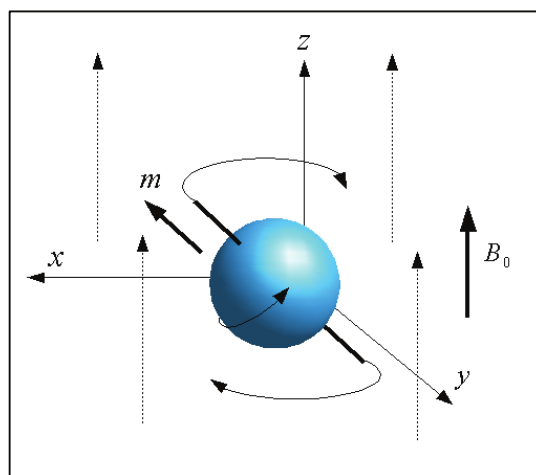


Figure 5: Cartoon representation of nuclear spin precession induced by the external magnetic field. B_0 represents the direction of the field, m the rotational axis of the spin [42].

This motion is called precession and its frequency is referred to as **Larmor frequency** ω_0 .

$$\omega_0 = -\gamma B_0$$

2.1.2 Magnetic Resonance

In the presence of a static magnetic field, which produces spin polarization, a radio frequency field of a proper frequency can induce a transition of a nucleus from the lower energy level to the higher energy state. This transition, also referred to as “spin flip”, requires absorption of radio frequency energy. The absorption of energy, called “resonance”, can only occur at a resonance frequency equal to the Larmor frequency ω_0 . The resonance frequency is directly proportional to the field strength of the external magnetic field B_0 . The spectrometer used in the present study operated at the field strength of 14.1 Tesla, providing a resonance frequency of 600 MHz.

During an NMR experiment, the excess spins in an orientation parallel to the external magnetic field give rise to a microscopic magnetization. This magnetization is flipped into the x-y-plane and due to the rotation, caused by the Larmor frequency, induces a voltage in the receiver coil, which can then be read off as the NMR signal. This produces a radio frequency signal that is measured in NMR spectroscopy. During the relaxation process, the transverse magnetization relaxes back into equilibrium, leading to the characteristic decreasing voltage in the receiver coil, called free induction decay (FID). Subsequently, a Fourier transformation produces the NMR spectrum that can then be used for qualitative or quantitative evaluation.

2.1.3 Chemical Shift and J- coupling

The use of NMR spectroscopy in organic chemistry is based on the close relationship between information that can be obtained through NMR spectra and the molecular structures of the chemical compounds. Two quantities are measurable in NMR spectroscopy, the “chemical shift” and “J coupling”. These parameters explain a characteristic change of resonance frequency of a chemical compound that is the basis for molecular structure analysis. Each nuclear isotope in a homogenous magnetic field would be expected to provide a single narrow peak at the Larmor frequency of that field. However, the Larmor frequency of a given nucleus is influenced by the electronic structure of its atomic environment. Electrons surrounding the proton in a covalent bond are magnetic. They, therefore, in response to the external magnetic field, generate a secondary field which shields the nucleus from the external field. Thus,

different magnetically inequivalent nuclear spins resonate at slightly different field strengths. This phenomenon is called **chemical shift**. Chemical shifts are very small compared to the actual field strength of the external magnetic field and are commonly referred to as parts per million (ppm). They are displayed in relative units, using a reference compound. Most commonly, tetramethylsilane (TMS) serves as reference compound; its chemical shift equals zero by definition. TMS spins have a very strong shielding. Because of that, the vast majority of chemical compounds have a positive chemical shift when referenced to TMS.

In Figure 6, the structure formula and an exemplary ^1H NMR spectrum of lactate are displayed. Lactate is one of the most common and best analyzed metabolites present in the spectrum of PCa, mainly because of its distinguished peak pattern. Its accumulation is due to increased metabolism in cancer and is a sign of high malignancy. The electro-negative oxygen-atoms in the chemical compound of lactate exert a shielding and are the origin of the chemical shift in this molecule. The methyl compound ($-\text{CH}_3$) is shielded more than the methin compound ($-\text{CH}$), causing a lower Larmor frequency and resonance at 1.33 ppm as opposed to 4.1 ppm. The different chemical shifts and Larmor frequencies cause the distinct peak pattern of lactate with a peak at 4.1 ppm and a 3- fold higher peak at 1.33 ppm.

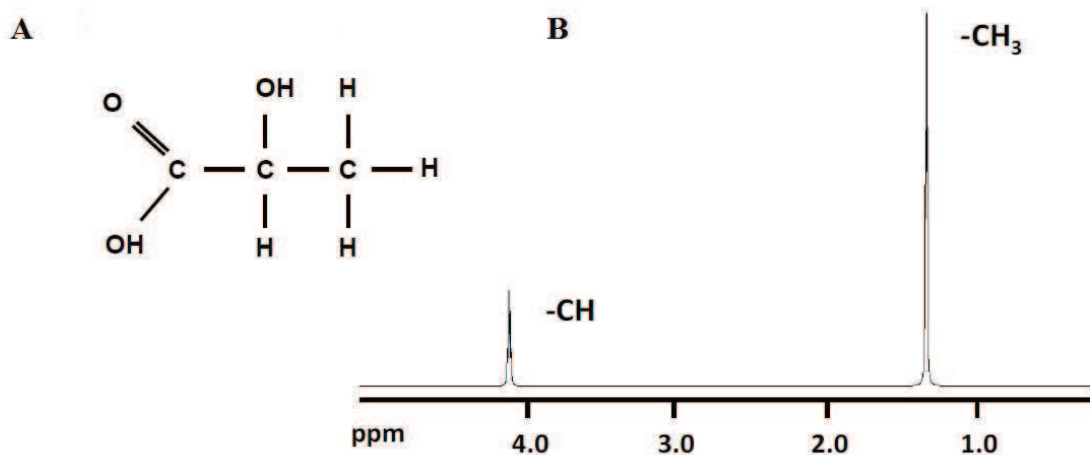


Figure 6: Molecular structure (A) and ^1H NMR spectrum (B) of the metabolite lactate: the methyl compound ($-\text{CH}_3$) is shielded more than the methin compound ($-\text{CH}$), causing a distinct peak pattern with a peak at 4.1 ppm and a 3- fold higher peak around 1.33 ppm [43].

J coupling or **spin-spin coupling** describes the phenomenon that single peaks are split into multiple peaks (multiplets) because of small interactions, ‘coupling’, through the chemical bonds between neighboring protons in a chemical compound. A proton spin in a proton group

in the chemical compound can have two possible orientations, either aligned or opposed to an applied magnetic field. Opposed spins have the effect of altering the magnetic field experienced by the neighboring protons. Therefore, a single peak is split into two peaks by one single coupling proton. In case of a greater number of coupled equivalent protons in a neighboring group, the variety of spin direction combinations increases. Hence, two coupling protons result in a triplet peak with an intensity ratio of 1:2:1, as there is only one spin combination of the two spins causing an upfield and a downfield shift, whereas there are two ways of generating the inner peak, characterized by no shift. Coupling to three protons results in eight possible spin combinations and produces a quartet split with an intensity ratio of 1:3:3:1. In general, if a nuclear spin is coupled to n equivalent spins of one-half, its peak is split into an $(n+1)$ - fold multiplet with an amplitude ratio proportional to the binomial coefficients ${}_nC_r$ ($r = 0, 1, \dots, n$). The spacing between the peaks of a multiplet is always constant, characterized by the **coupling constant J** , which is independent of the applied magnetic field. Therefore, a multiplet can always be recognized by its closely spaced chemical shift peaks. Equivalent nuclei (spins of a distinct proton group with equivalent binding characteristics) do not interact with each other and do not cause a splitting. Below in Figure 7, the characteristic structure of the lactate NMR spectrum is demonstrated. The proton of the methin-compound ($-\text{CH}$) is coupling to the methyl-compound ($-\text{CH}_3$). It therefore splits into a quartet peak with an amplitude ratio of 1:3:3:1. The lactate methyl peak is split into a doublet peak by coupling to the methin compounds.

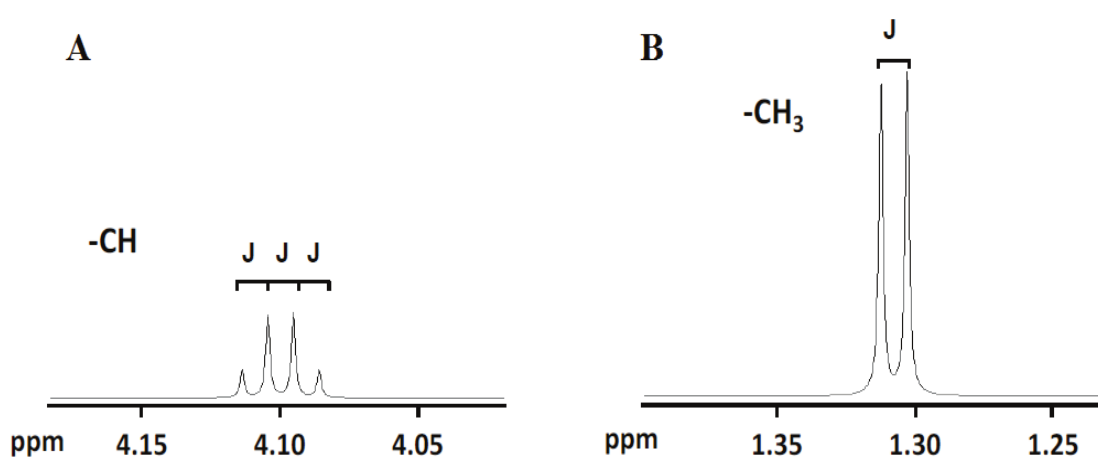


Figure 7: Illustration of scalar coupling of NMR lines of lactate: (A) Splitting of the methin peak into a quartet with intensity ratio of 1:3:3:1 by coupling with the methyl group, (B) splitting of the methyl peak into a doublet with an intensity ratio of 1:1 (B) [43].

2.2 Nuclear Magnetic Resonance Spectroscopy

In nuclear magnetic resonance (NMR) spectroscopy, radio-frequency signals emitted by spins that are transitioning back to their original low-energy state are being displayed in a spectrum, as a function of their resonance frequency. Peak integrals in the spectrum correlate with the number of spins in the sample giving rise to this specific signal. Therefore, quantitative information about the chemical compounds present in a scanned sample can be obtained through NMR spectroscopy. High field NMR spectrometers have been shown to provide spectra with a high resolution and a low signal-to-noise-ratio.

2.2.1 Magic Angle Spinning and ^1H HRMAS NMR Spectroscopy

“Magic Angle Spinning” (MAS) was first described in 1958 by E. Andrew, A. Bradbury, and R. Eades [44] and independently in 1959 by I. J. Lowe [45], and is a technique that was originally developed for solid-state NMR spectroscopy studies.

In NMR of liquid samples, anisotropic interactions between nuclei are usually averaged out by the isotropic rotational diffusion. In more solid-like structures, such as biological tissues, the molecules undergo motions in restricted geometries, which give rise to anisotropic effects, such as dipolar couplings, quadrupolar interactions or chemical shift anisotropy. These effects result in spectral line broadening, that renders a clear distinction of different metabolites impossible.

By mechanically rotating (spinning) the sample at an angle of $\theta = 54.74^\circ$ with respect to the direction of the external magnetic field, the anisotropic interactions can be averaged to zero, as all anisotropic interaction Hamiltonians are scaled by the factor $\frac{1}{2}(3\cos^2\theta-1)$. This procedure mimics the fast isotropic tumbling of the molecules in solution that leads to the averaging of all anisotropic interactions. The angle of $\theta = 54.74^\circ$ is called the “magic angle”. Rapid spinning of a sample at the magic angle can reduce the spectral line-broadening and results in highly resolved spectra (Figure 8). This spectroscopy method is therefore named “ ^1H High Resolution Magic Angle Spinning Nuclear Magnetic Resonance Spectroscopy” (^1H HRMAS MRS).

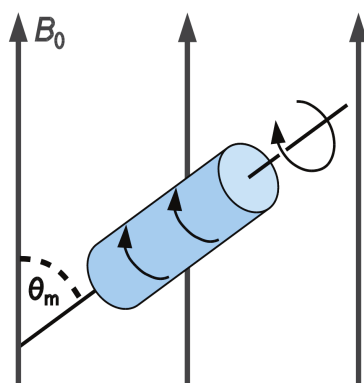


Figure 8: Principle of magic-angle spinning: The sample (blue) is rotated with high frequency within the external magnetic field (B_0). The axis of rotation is tilted by the magic angle θ_m with respect to the direction of B_0 [42].

In 1996, Cheng et al. reported the use of ^1H HRMAS MRS on intact human tissue samples for the first time [34]. They were able to show that using this method on biological tissue samples, it is possible to omit the destruction of tissue architecture, while at the same time spectral line-broadening can be minimized and spectral resolution can be increased [46].

Subsequent histopathological analysis can be performed following an ^1H HRMAS MRS experiment to investigate correlations between these biochemical spectra and the pathology of a sample [47, 48]. Since 1997, multiple studies have been performed in order to improve the technique of ^1H HRMAS MRS and evaluate its clinical applicability. This method has been shown to be highly reproducible, with the potential to be computer- automated [34, 35, 47, 49,50].

2.2.2 MAS Spinning Rates and Spinning Side Bands

Fast spinning at the magic angle is necessary to average out anisotropic effects and decrease spectral line broadening. Spinning rates for ^1H HRMAS MRS on biological tissues are commonly around 1 kHz or higher. With the smallest rotors, a spinning rate up to 70kHz and higher is possible. However, fast spinning increases the risk of destructing tissue architecture. To preserve a better tissue quality for subsequent pathological evaluation, a reduction of sample spinning rates has proven to be useful. Spinning rates of 600Hz or 700Hz have been shown to minimize the destruction of tissue architecture through HRMAS centrifugation while at the same time providing equally good spectral information as higher spinning rates [37].

At slow-rate spinning, single pulse spectra are dominated by a large water peak and its “spinning sidebands”, originating from the oriented water in the tissue. Spinning sidebands describe signals that appear as additional peaks in the spectrum on either side of a large genuine peak. They are caused by the chemical shift anisotropy and appear at distances to the genuine peak that are multiples of the spinning frequency [51]. In biological tissues, residual anisotropic interactions are very weak and spinning side bands are typically not observed. However, if present, special rotor-synchronized suppression methods, like the TOSS pulse sequence protocol, can be used to effectively suppress spinning sidebands. Also, by applying a simple minimum function ($\text{Min}(A, B)$, described below) on two spectra acquired at different but close spinning rates (for example 600Hz and 700Hz), spinning-sideband-free spectra can be produced [52].

In biological tissues, water is normally three orders of magnitude more abundant than other metabolites. In order to recover metabolites that overlap the strong baseline of the water resonance, suppression of the water signal is necessary during the acquisition of NMR spectra. The elimination of the water signal without losing other resonances is challenging [53]. Various water suppression protocols have been suggested, among them a DANTE (delay alternating with nutation for tailored excitation) pulse sequence protocol.

While preventing tissue damage by HRMAS centrifugation, slow-rate spinning has been shown to be sensitive enough for the purpose of disease diagnosis.

2.3 Metabolomics, Metabolite Profiles and Clinical Utility

Metabolomics has been defined as the study of the metabolome, which represents “the complete set of metabolites or low-molecular-weight intermediates, which are context dependent, varying according to the physiological, developmental or pathological state of the cell, tissue, organ or organism” [54]. This evolving field of science uses fundamental analytical techniques to study the global variation of metabolites by examining the underlying biochemistry of cellular processes. It profiles the metabolites present at the very moment of analysis. Metabolites can best be described as molecules that are products, reactants, intermediates or waste products generated during the execution of signals that a cell is receiving. Thus, each cellular process has its own metabolic signature and the analysis of metabolite concentrations can be used to create a metabolic profile that may function as a biomarker for the process [21]. Different techniques can be used to explore the metabolome and create metabolic profiles, including Mass Spectrometry (MS) and NMR spectroscopy. While MS is a highly sensitive method that rapidly provides extensive metabolic information, it requires extensive sample preparation (separation, extraction). NMR, on the other hand, has the ability to rapidly identify and quantify the majority of metabolites present in a sample, with only minimal sample preparation. Due to the characteristic chemical shift of a given chemical compound, the spectral peak pattern is uniquely characteristic for that metabolite, making it possible to identify and quantify the metabolites present in a sample. The metabolite concentration can be determined by measuring the area under the associated peaks. Certain metabolites play a crucial role in the characterization of malignant transformations in the prostate and can be assessed by using MR spectroscopy. For instance, in healthy prostate tissue and the corresponding fluid, high levels of citrate (Figure 9, concentration 8,000-15,000 nmol/g, compared to 150- 450 nmol/g in other soft tissues). In malignant prostate tissue, a pathological citrate oxidation can be found, resulting in a decrease of citrate levels (1,000-2,000 nmol/g) in the organ.

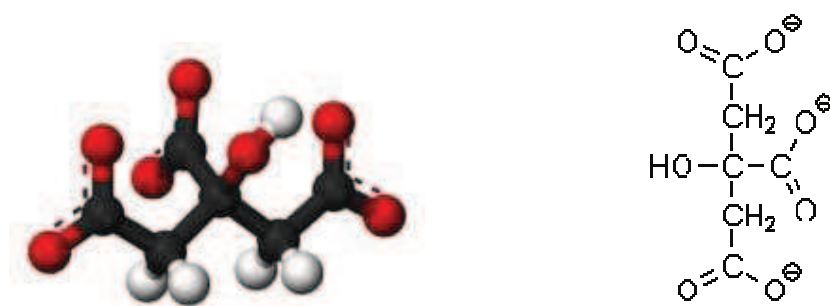


Figure 9: Molecular structure and chemical formula of the metabolite citrate [55].

Another important metabolite in the differentiation of cancerous versus non-cancerous tissue is choline (Figure 10). Choline, as well as its derivatives phosphocholine and glycerophosphocholine, is associated with alterations in cell membrane synthesis during malignant transformation [56, 57].

The levels of these metabolites are found to be elevated in prostate cancer tissue [59, 60].

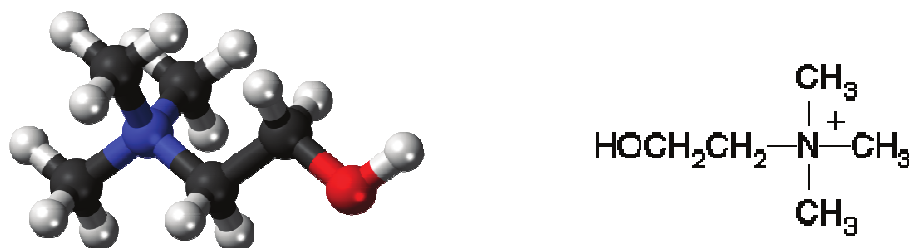


Figure 10: Molecular structure and chemical formula of the metabolite choline [58].

Polyamines, such as spermine, spermidine and putrescine, play an important role in sperm fusion and protein adhesion in the seminal fluid and have been found to be decreased in malignant tissue [21, 47]. Concentrations of lactate and alanine- as indicators for an elevated energy metabolism- show a highly significant increase in malignant tissue, whereas they are found to be very low in benign tissue [61]. The metabolite ethanolamine is decreased in cancerous tissue, while the concentrations of phosphoethanolamine as well as glycerophosphoethanolamine are found to be increased [62, 63]. In routine clinical diagnostics, the metabolites most commonly analyzed are citrate, choline and creatine (Figure 9-11).

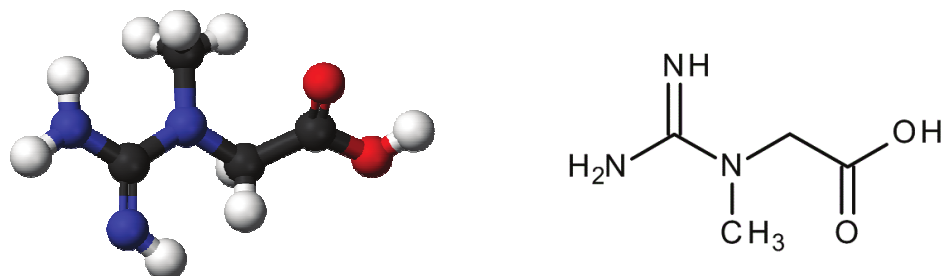


Figure 11: Molecular structure and chemical formula of the metabolite creatine [64].

Because absolute quantification is challenging, and overlapping of resonances in regions of interest is common, metabolite ratios are often used instead of individual metabolite

concentrations. The ratio most relevant in the clinical application of MRS of the prostate is choline + creatine to citrate ((Cho+Cr)/Cit). It has been shown to correlate with the Gleason score and can therefore be used for *in vivo* clinical classification of prostate samples [21, 60]. A ratio ranging two standard deviations above average is classified as suspicious and a ratio of three standard deviations as very suspicious for malignant transformation [65]. Other metabolite ratios can be used in the differentiation of cancerous versus non-cancerous tissue. In malignant prostate tissue, the ratios of total choline to citrate (tCho/Cit), choline to creatine (Cho/Cr), glycerophosphocholine plus phosphocholine to creatine ((GPC+PC)/Cr) and lactate to alanine (Lac/Ala) have been shown to be significantly increased, while the ratio of citrate to creatine (Cit/Cr) has been found significantly decreased, compared to benign tissue [60]. A significant correlation with the Gleason score has been demonstrated for certain metabolite ratios, including choline to creatine (Cho/Cr), choline to citrate(Cho/Cit), citrate to creatine (Cit/Cr) and glycerophosphocholine plus phosphocholine to creatine ((GPC+PC)/Cr).

Table 1 summarizes the observed changes in single metabolites (1a) and metabolite ratios (1b) in benign versus malignant human prostate tissue.

Table 1a: Observed changes in single metabolite concentrations in malignant versus benign human prostate tissue samples [66].

Metabolite	Change	Reference
Lactate	Increase	[60]
Alanine	Increase	[60]
Citrate	Decrease	[59]
Choline	Increase	[59]
Phosphocholine	Increase	[59, 62]
Glycerophosphocholine	Increase	[59, 62]
Ethanolamine	Decrease	[62]
Phosphoethanolamine	Increase	[62]
Glycerophosphoethanolamine	Increase	[62]
Polyamines	Decrease	[59]

Table 1b: Observed changes in metabolite ratios in malignant versus benign human prostate tissue samples [66].

Metabolite Ratio	Change	Reference
Choline / Creatine	Increase	[60]
Lactate / Alanine	Increase	[60]
(Glycerophosphocholine + Phosphocholine) / Creatine	Increase	[60]
Citrate / Creatine	Decrease	[60]
(Choline + creatine) / Citrate	Decrease	[60]
Phosphocholine / Glycerophosphocholine	Increase	[62]
Phosphocholine / Phosphoethanolamine	Increase	[62]
Phosphoethanolamine / Ethanolamine	Increase	[62]
Glycerophosphoethanolamine / Ethanolamine	Increase	[62]

To make MR spectroscopy results more applicable to clinical use, metabolite profiles, also referred to as metabolomics profiles, were created. Instead of observing only the change in a single metabolite caused by malignant processes, large ensembles of metabolites were analyzed [50, 62, 67, 68]. The resulting profiles of PCa have the potential to be effective tools in the *in vivo* diagnosis of cancer of the prostate. The diagnostic utility of PCa metabolomics profiles has been studied extensively in the past years using ¹H HRMAS MRS. Spectroscopy results obtained from prostatectomy tissue samples of biopsy-proven PCa patients were evaluated using principle component analysis and correlated to the results of subsequent histopathology. The resulting metabolite profiles of PCa appear to be sensitive in differentiating benign from malignant tissue and furthermore, to correlate with patients serum PSA-level. Previous results indicated that prostate metabolic profiles may reflect cancer status even more sensitively than currently available histopathological parameters [50].

Besides studying prostate cancer, other malignant transformations have been investigated successfully, using ¹H HRMAS MRS. Metabolite spectra have been obtained from samples of human glioblastoma multiforme [47] and other brain tumor species [49], human breast ductal carcinomas [69], Alzheimer's disease [70] or pediatric brain tumors [71]. Current research efforts aim at creating and improving metabolomics profiles of different malignant transformations and evaluating their diagnostic utility for future *in vivo* use.

3 Scientific Background II: Immunohistochemistry of Prostate Cancer

Immunohistochemistry (IHC) refers to a scientific method that is based on the principle of antibodies binding specifically to antigens in biological tissues [72]. IHC staining is widely used in medical research to detect and diagnose biomarkers, specific proteins or abnormal cells (for example in malignant transformations). An antibody-antigen interaction is visualized by the conjugation of the antibody to an enzyme (like peroxidase or phosphatase) that catalyzes a color-producing reaction or a fluorophore (most commonly fluorescein or rhodamine) that produces immunofluorescence. For antibodies, both monoclonal and polyclonal antibodies can be used. In contrast to polyclonal antibodies, monoclonal show specificity for a single epitope and are therefore more valuable to target a specific antigen. Antibodies can be directly labeled with an IHC reporter that is able to detect the target with an enzyme- or chromophore- reaction. This direct IHC method is simple and rapid but shows a low sensitivity. To improve sensitivity, an indirect method can be used, where an unlabeled primary antibody binds to the target antigen and a labeled secondary antibody is used to detect the primary antibody. Due to the binding of several secondary antibodies to each primary antibody, signal amplification can be achieved and sensitivity improved. To further signal amplification, secondary antibodies are often conjugated with biotin molecules that can recruit avidin-, streptavidin- or neutravidin proteinbound complexes. IHC reporter molecules are chromophore or fluorophore enzyme labels that react with the substrate to produce a color (chromogenic reaction) or fluorescence. Alkaline phosphatase and horseradish peroxidase are the most commonly used labels in chromogenic IHC. A wide range of substrates is available for different color reactions. Most often, 3,3'-Diaminobenzidine (DAB) is used to produce a brown color, but other substrates like 5-Bromo-4-chloro-3-indolyl phosphate (BCIP) and nitro blue tetrazolium chloride (NBT), producing a dark blue or purple color, are available as well. As immunological reactions are highly susceptible to external influences, IHC requires a careful sample preparation. Tissue samples are commonly micro-sectioned, formalin-fixed and embedded in paraffin. In order to make epitopes available for antibody binding, several steps like deparaffinization and antigen retrieval have to be carried out. To ensure a good staining quality, endogenous biotins or enzymes need to be blocked or quenched prior to staining. Nonspecific binding that results in background stain and can mask the detection of target antigens can be reduced by incubating the samples with a buffer that blocks the reactive sites. After all steps of the IHC method have been carried out, a counterstain can be applied to

provide a contrast that helps to enhance the detection of the primary stain. Common counterstains include Hematoxylin, 4',6-diamidino-2-phenylindole (DAPI) or Methyl Green. Immunohistochemical methods have been proven useful in the diagnosis of different malignant transformations, including prostate cancer [38, 39,73] and have been increasingly incorporated in basic diagnosis.

A cytoplasmic protein involved in the beta-oxidation of branched-chain fatty acids, *P504S*, also known as *AMACR* (alpha-methylacyl-CoA racemase), shows high expression in prostate cancer and a modest expression in benign prostate tissue. It can therefore be used as an immunomarker to differentiate between cancerous and non-cancerous glands [74-76]. Another protein, *CK903*, also known as *34-beta-E12* (high molecular weight cytokeratin), is highly expressed in the cytoplasm of basal cells of healthy prostate glands, whereas it cannot be found in cancerous tissue. It functions as a marker of benign prostate tissue [77]. The tumor suppressor protein p63 is a basal cell marker that can be used to stain nuclei of benign prostate gland epithelium. p63 belongs to the same family of tumor suppressor proteins like p53 and p73 and has been suspected to be the original family member, with p53 and p73 being derived from it [78]. p63 gene encodes for 2 protein isoforms, one of which (TAp63) plays an important role in apoptotic function [79]. With the help of p63-antibodies it is possible to differentiate between prostate adenocarcinoma and benign prostate tissue, as malignant glands do not have basal cells that could be stained. Also, p63 immunostaining can be used to differentiate between urothelial cancer (high expression) and PCa (no expression) in cases where a clinical differentiation seems difficult [80]. By combining IHC stainings of P504S with those of CK903 and p63, cancerous prostate samples can be differentiated from both normal prostate tissue and benign lesions. While P504S has a positive expression in both PCa and Prostate Intraepithelial Neoplasia (PIN), the stainings for both CK903 and p63 are negative in PCa and positive in PIN, making a differentiation between cancer and PIN possible. Benign prostate hyperplasia (BPH) is a benign transformation of the prostate. BPH is a relatively common disease in older men and is not classified as precancerous lesion. While non-cancerous prostate tissue stains positive for CK903 and p63, BPH does not [81]. Therefore, IHC is a useful tool for the differentiation of cancerous from non-cancerous conditions, but also malignant from benign transformations or preliminary stages.

Besides using the mentioned immunomarkers separately on suspicious prostate tissue, they can also be combined as a triple-cocktail-staining with a single- or double chromogen

reaction, making it possible to obtain immunohistochemical information from the very same tissue [73, 82].

Compared to conventional histopathologic examinations, IHC has several advantages in the diagnosis of PCa. Conventional histopathologic analysis of suspicious tissue after prostate needle biopsy or prostatectomy is commonly carried out using a Hematoxylin & Eosin staining procedure. Subsequently, the stained tissue slides have to be analyzed by a pathologist with fundamental knowledge on prostate tissue pathology. In contrast, IHC provides objective pathology results, based on the fact that staining occurs only in tissue that expressed the targeted antigens. Using the immunomarkers P504S (AMACR), CK903 and p63, it is possible to obtain an objective differentiation of tissue pathology in suspicious prostate tissue. The chromogenic reaction that is part of the visualization in IHC also yields the opportunity for a computer automated evaluation. DAB produces a dark brown color that provides a good enough contrast between benign and malignant tissue. A specifically designed computer program could be used to measure cancerous and non-cancerous tissue distribution in a sample through the detection of dark versus light tissue areas. IHC therefore has the potential to allow objective and fast evaluation of large numbers of tissue samples, minimizing intra- and inter-observer- variability.

4 Aims of the Study

Current methods for prostate cancer diagnosis are not satisfying and overdiagnosis and overtreatment are very common, due to the insufficiency of state-of-the-art diagnostic tools to accurately distinguish between highly aggressive and malignant cancers and more indolent cases. Novel, observer-independent and quantitative diagnostic methods for PCa are urgently needed. This study aims to establish a novel approach for identification of PCa biomarkers, by quantification of metabolomic profiles measured from prostate tissue by ^1H HRMAS MRS.

It has been demonstrated that ^1H HRMAS MRS does not destroy the tissue architecture of a sample, thus allowing for unbiased subsequent histopathological evaluation of a scanned tissue piece [16, 49]. In previous studies of prostate cancer metabolomics, conventional histopathology was commonly used as reference standard [16], due to its facile utility and broad clinical applicability. Immunohistochemistry, in contrast, presents a more accurate and objective diagnostical method than conventional histopathology, and yields the potential to be computer automated. Therefore, this study aims to explore the potential of three prostate immunomarkers- P504S (Alpha-Methylacyl-CoA-Racemase), CK903 (high-molecular weight cytokeratin) and p63- as tools for quantitative analysis of immunohistochemistry performed on the same tissue samples.

To achieve this aim, a quantitative IHC analysis program was developed to automatically and objectively determine the percentage of cancerous and benign glands in a prostate tissue sample. Additionally, this project aims to confirm the validity of the presented approach by using a conventional histopathological evaluation and a quantitative IHC analysis performed by an experienced pathologist. This study aims to use these quantitative measures of tissue pathology obtained from IHC to identify PCa biomarkers in a metabolomic profile measured with ^1H HRMAS MRS in the same sample. For that, correlations of spectral intensities with the results of quantitative IHC analysis will be examined.

In an attempt to explore the stability and utility of the proposed immunomarkers for use following ^1H HRMAS MRS, the presented project aims to compare the quality and evaluability of immunostainings of tissue sections that have been subjected to ^1H HRMAS MRS to samples from the same prostate that have not undergone spectroscopic procedures, in a subset of the sample cohort.

To further explore the potential of our novel approach, this study aims to investigate the utility of it to identify metabolomic biomarkers of PCa recurrence. For that, patient outcomes

and recurrence five years after initial diagnosis will be obtained and correlated to the results of ^1H HRMAS MRS to identify metabolomic markers of recurrence in the dataset.

5 Material and Methods

Tissue acquisition, medical record review and all experiments performed in this study were approved by the Institutional Review Board (IRB) of the Massachusetts General Hospital (MGH) and in accordance with the Health Insurance Portability and Accountability Act (HIPAA).

5.1 Prostate Tissue Samples and Patient Demographics

Human prostate tissue specimens were prospectively collected from 51 biopsy-proven PCa patients who underwent prostatectomy surgery at the Department of Urology at the MGH in Boston, between January of 2007 and December of 2008. The tissue samples were collected from the operating suite, instantly frozen and stored at a temperature of -80°C prior to the experiments.

The patient medical records were reviewed to determine important demographic information, including: patient's age at surgery, pre-operative PSA-levels, final histopathological diagnosis, including GLEASON grades, and adjuvant treatment, if administered (defined as any additional treatment in a time-period of less than 6 months before or after surgery).

5.2 ^1H HRMAS NMR Spectroscopy

Spectroscopy measurements were carried out on an AVANCE 600MR spectrometer (BRUKER Biospin, Billerica, MA) operating at 600.13 MHz (14.1T). A 4-mm zirconia rotor was used with Kel-F inserts to create a 12 μl -spherical space that confined the tissue to the center of the receiving coil. A small silicone rubber sample, permanently fixed inside one of the Kel-F spacers, functioned as external reference standard for frequency reference (0.06ppm from TMS) and concentration quantification (Figure 12).



Figure 12: BRUKER Biospin AVANCE III 600MHz spectrometer at the “Martinos Center for Biomedical Imaging”, Massachusetts General Hospital / Harvard Medical School, Boston

5.2.1 Sample Preparation

The sample preparation was performed at room temperature in a preparation area adjacent to the spectrometer. The prostate tissue samples were collected from the storage freezer (-80 degrees Celsius). To prevent tissue destruction during the preparation process, the specimens were stored on dry ice at all times during handling. A small piece of tissue (approximately 10mg) was cut from each sample, using a scalpel with a blade size 10, and carefully placed into the rotor. The weight of the sample in the rotor was measured using a micro weight scale. Depending on the total weight of the tissue piece, between 2 and 8 μ l of D₂O were added for ²H field locking. The rotor was carefully closed with a screw and a cap, marked at the bottom with a permanent marker, and placed into the probe.

5.2.2 Spectroscopy Scan

After adjusting the magic angle, MR spectra were recorded at a temperature of 4°C for better tissue preservation, with the resonance frequency centered on the water resonance. Lock and phase adjustments as well as shimming were performed if necessary. The rotor-spinning rate was regulated by a MAS controlling interface. Water suppressed spectra were recorded using spinning frequencies of 600Hz and 700Hz. A rotor synchronized DANTE (delay alternating

with nutation for tailored excitation) pulse sequence (1000 DANTE pulses of $1.5\mu\text{s}$, 8.4° flip angle) [37] for water suppression was used in combination with a Carr-Purcell-Meiboom-Gill (CPMG) pulse sequence at short TE (30ms). A repetition time of 5s and an average 32 transients were used.

The CPMG pulse starts with a 90° pulse which flips the magnetization in the x-y-plane. Then, during the decay that follows, some spins slow down due to lower local field strength, while others speed up. T_2^* decay refers to an exponential decrease in signal strength compared to T_2 decay, due to inhomogeneity of the magnet. In the CPMG pulse sequence, a series of 180° pulses is applied, which make it possible to refocus the T_2^* signal and remove inhomogeneity effects in order to correct pulse-accuracy errors (Figure 13).

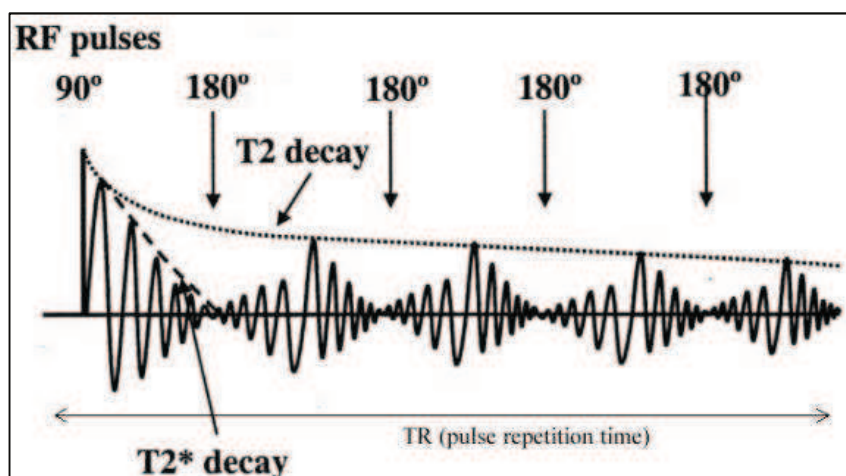
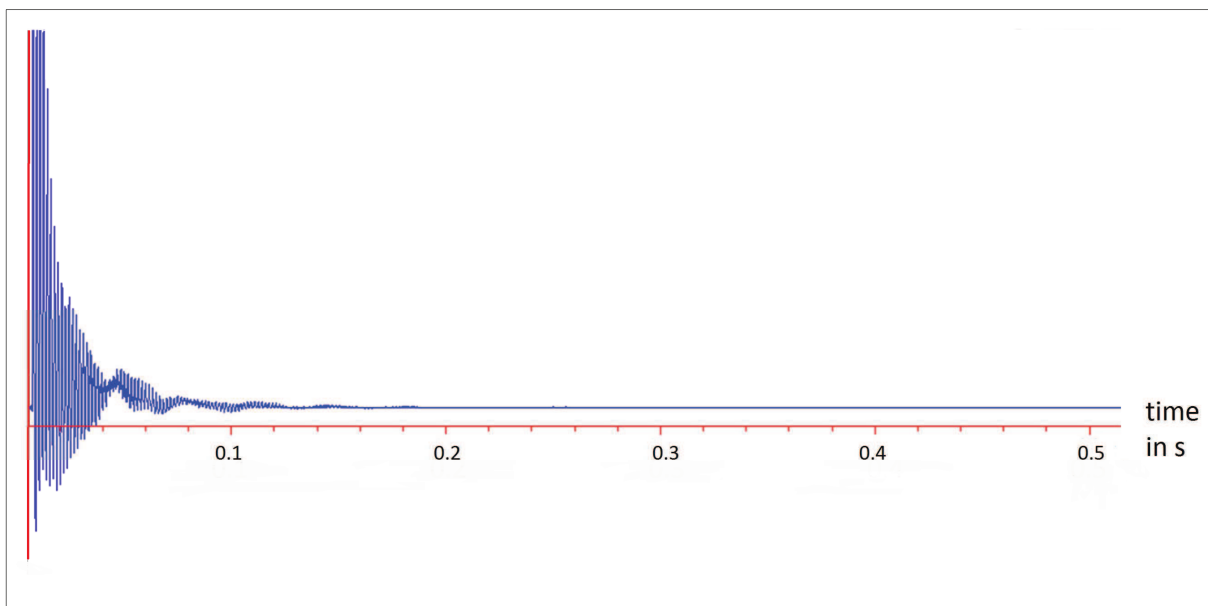


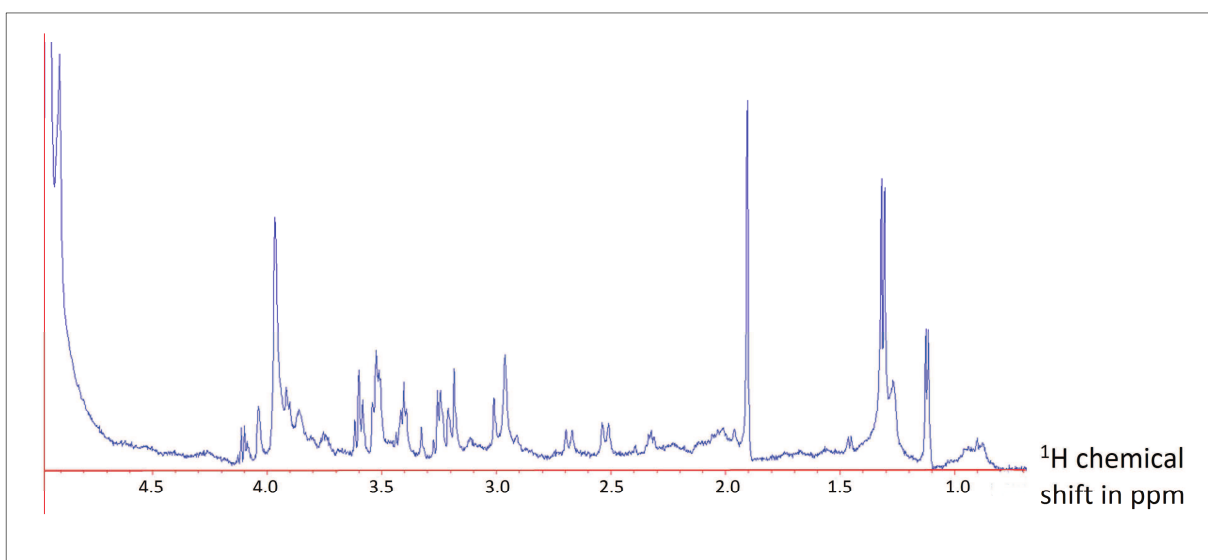
Figure 13: Carr-Purcell-Meiboom-Gill pulse sequence (echo train acquisition): after an initial 90° pulse, multiple 180° pulses are applied to refocus inhomogeneous line broadening of the nuclear spins. This technique is used to self-correct accuracy errors in T_2 - (spin-spin relaxation) weighted imaging [83].

5.2.3 Data Processing

NMR data (BRUKER Biospin 14.1T raw data) was manually processed offline using the commercial software NUTS (Acorn NMR Inc., Livermore, CA). All free induction decays were subjected to 1Hz apodization before Fourier transformation, followed by baseline correction and phase adjustment of both zero and first order. A typical dataset before and after Fourier transformation is illustrated in Figure 14.



A

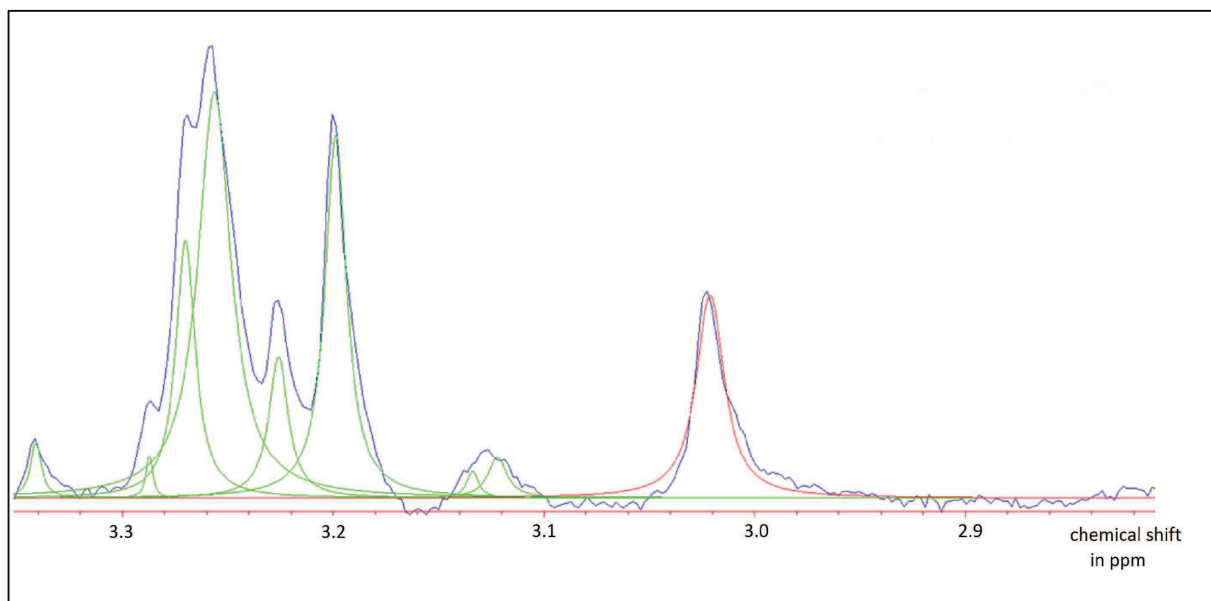


B

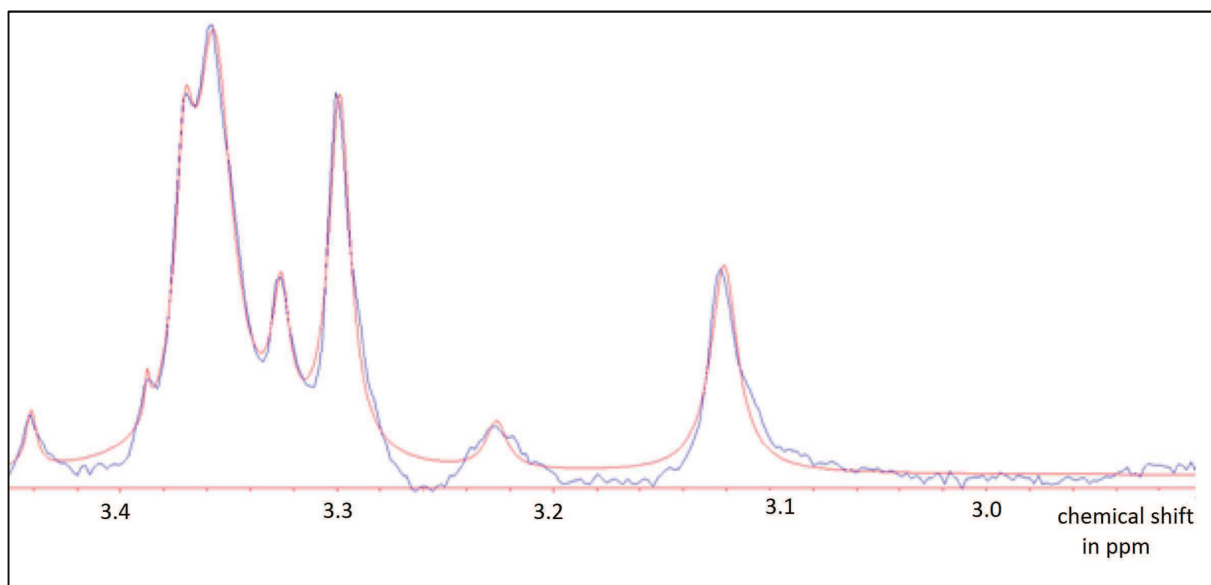
Figure 14: Typical ^1H time (A) and frequency (B) domain data: FID before Fourier transformation (A, x: time in sec, y: signal intensities) and data after Fourier transformation (B, x: chemical shift in ppm, y: signal intensities)

Spectral resonance intensities used for this study represented integrals of curve fittings of either 600 or 700 Hz HRMAS spectra. Spectra at both frequencies were obtained in order to eliminate spinning sidebands (SSB) which appear at different regions in 600 and 700 Hz spectra. Usually, quantification of NMR metabolites by spectral modeling is conducted assuming an ideal *Lorentzian* or *Gaussian* lineshape. However, in reality, experimental

lineshape fit neither of them perfectly. In order to minimize systematic fitting errors, mixed *Lorentzian-Gaussian* line shapes (*Voigt* lineshapes, [84]) were used in this study (Figure 15).



A



B

Figure 15: Curve fitting process in NUTS: Peaks are manually picked by the user, individual integrals are calculated (green lines, A) and multiple iterations are carried out, in order to produce an optimized curve fit (red line, B). Blue line: original spectrum.

In order to produce SSB- free spectra, spectral intensities acquired at 600Hz and intensities recorded at 700Hz from the same sample were subjected to a simple processing scheme called Min (A,B): By calculating the minimum values from both spectra for the entire range of

interest, SSB could be eliminated, as they occurred at different intervals from the water peak [52]. The spectra were referenced using the lactate double peak at 1.34 and 1.32 ppm. Spectral intensities were then measured in 36 regions of interest, known to represent characteristic regions of PCa metabolites, as described previously (the most relevant are displayed in Table 2, [50]). Final spectral intensities were calculated from relative intensities normalized by the overall intensity of the spectral region between 0.5 and 4.5 ppm from the spectrum recorded at 600Hz [37].

Table 2: Spectral regions of interest for prostate cancer metabolites [50].

Spectral region in ppm	Metabolite(s)
4.38	N-acetylaspartate
4.09	Lactate
3.75	L-glutamine
3.74	L-glutamic acid
3.605	Glycerophosphocholine
3.52	Myo-inositol
3.42	Taurine
3.22	Phosphocholine
3.18	Choline
3.05 – 3.14	Spermine
3.02	Creatine / Phosphocreatine
2.52 - 2.71	(Sodium-) Citrate
1.92	Acetate
1.46	Alanine
1.32 /1.34	Lactate
0.9	Lipids

5.3 Immunohistochemistry

5.3.1 Immunohistochemistry Material and Equipment

The immunomarkers P504S, CK903 and p63 were chosen for this study, as their specificity and utility as well as their clinical applicability have been demonstrated multiple times in the literature [73, 82, 85]. As primary antibodies, rabbit monoclonal anti-human AMACR (P504S), mouse monoclonal anti-human CK903 and mouse monoclonal anti-human p63 were used. Biotinylated anti-rabbit IgG and biotinylated anti-mouse IgG were applied as secondary antibodies. For the visualization of the immune reaction, a single color reaction was performed, using 3,3'-Diaminobenzidine (DAB). DAB was chosen for visualization, because of its characteristic dark brown color, which facilitates qualitative evaluation and furthermore, yields the potential for computer-automated quantitative evaluation. A summary of all materials and chemicals used for IHC can be found in Table 3.

5.3.2. Immunohistochemistry Protocol

An IHC staining protocol was established in our laboratory according to antibody/reagent specifications. Effectiveness and specificity experiments were carried out using confirmed PCa tissue as positive control. Different incubation times and antibody dilutions were tested to identify the best possible staining conditions. The following IHC protocol illustrates the optimized algorithm for the immunostaining experiments in this study.

Table 3: IHC Antibodies, Reagents and Equipment*

Antibodies	Chemicals / Reagents	Materials /Equipment
Rabbit monoclonal anti-human AMACR antibody, 1:50 (DAKO)	Formalin (FS)	Microtome (Leica RM2235)
Mouse monoclonal anti-human CK903 antibody, 1:50 (DAKO)	Xylene (FS)	Paraffin embedding station (Leica)
Mouse monoclonal anti-human p63 antibody, 1:50 (DAKO)	Ethanol 100% / 95% / 75% (FS)	Barrier slides (Biogenics)
Secondary biotinylated anti-rabbit IgG, 1:50 (FS)	Paraffin (FS)	Baking oven (GE)
Secondary biotinylated anti-mouse IgG, 1:50 (FS)	Deionized H ₂ O	Microwave with temperature probe, 800W (GE)
	Phosphate buffered saline (PBS), (FS)	Beakers (FS)
	TRIS 7 EDTA buffer, pH 9.0, 10mM, 1mM (FS)	Pipettors + pipette tips (1000µl, 200µl, 20µl) (Gilson, VWR)
	Methanol (FS)	Kim Wipes (KimTech)
	Hydrogenperoxide (H ₂ O ₂), (FS)	Dry Ice and Ice
	Protein Block (DAKO)	Humid Chambers (FS)
	Avidin / Biotin / Peroxidase Complex (Vectastain)	Permanent mounting media (FS)
	Diaminobenzidine 3'3 tablets (Sigma Aldrich)	Slide covers (FS)
	Methyl Green (FS)	
	Hematoxylin (FS)	
	Eosin (FS)	

* FS... purchased from Thermo Fisher Scientific (Hampton, NH)

5.3.2.1 Sample Preparation

After completion of NMR spectroscopy, the prostate tissue samples were removed from the rotor, fixed in a formalin bath overnight and embedded in paraffin. Small tissue sections (5µm) were cut using a microtome and transferred instantly on barrier glass slides.

The slides had to be baked at a temperature of 60°C for 2 hours, in order to insure tissue adherence. They were then deparaffinized and rehydrated according to the following steps:

- Xylene 3 x 5 min
- Ethanol 100% 2 x 5 min
- Ethanol 95% 1 x 5 min
- Ethanol 70% 1 x 5 min
- Deionized H₂O 2 x 5 min

To ensure hydration and prevent tissue sections from drying out, slides were either incubated with a target solution or kept in a buffer solution at all times. Three adjacent slides were used for immunostaining with the designated primary antibodies. A fourth adjacent slide was left for staining with Hematoxylin & Eosin (see section Qualitative Histopathology).

5. 3.2.2 Antigen Retrieval, Quenching of Endogenous Peroxidases and Protein Block

To improve the demonstration of antigens, an antigen retrieval step was required prior to the application of the primary antibodies. During formalin-fixation, methylene bridges are formed that cross-link proteins, therefore masking antigenic sites. Antigen retrieval, a method discovered in the early 1990's [86] is a non-enzymatic pretreatment to break down these protein-cross links, thereby uncovering hidden epitopes [87, 88]. The technique most commonly used is called "Heat Induced Epitope Retrieval (HIER)". Formalin-fixed, paraffin-embedded tissue slides are heated in a specific antigen retrieval solution for a designated time. Microwave, steamer, autoclave or water bath serve as suitable heating devices. Citrate buffer (pH 6.0) and TRIS/EDTA (pH 9.0) or EDTA (pH 8.0) buffer solutions are suitable for most antigens [89]. An alternative approach for unmasking antigenic sites is "Proteolytic Induced Epitope Retrieval (PIER)" which uses enzyme digestion. Effective reagents include proteinase K, trypsin, chymotrypsin, pepsin and other proteases. The enzymatic method tends to be much gentler, but sometimes may destroy tissue morphology [90].

Heat induced epitope retrieval using TRIS/EDTA buffer solution (pH 9.0,10mM/1mM) for P504S (AMACR) and citrate buffer (pH 6.0, 0.1M) for CK903 and p63 respectively were

identified as suitable antigen retrieval solutions for this study in preliminary experiments. Deparaffinized and rehydrated tissue slides had to be immersed into the determined retrieval solutions and heated in a commercial microwave (800W, 199°C) for 30 minutes. Afterwards, the slides had to cool down in a tap water bath for 15 minutes.

Endogenous peroxidase activity in cells or tissue sections used for IHC may cause high, non-specific background staining, due to catalyzation of chromogenic or chemiluminescent substrates. To improve the staining quality in this study, the non-specific background staining was reduced by quenching (irreversible inactivation) of endogenous peroxidases. For that, tissue slides were immersed into deionized H₂O and PBS for 5 minutes each. Then, 3% H₂O₂ in methanol was applied to sections for 10 minutes. Slides were washed in deionized H₂O again for 5 minutes.

To enhance the detection of a target antigen in IHC procedures, an Avidin-Biotin-Complex (ABC) has been proven useful. Biotin, a coenzyme in many biological reactions, has a strong binding affinity with avidin and can thus be conjugated to antibodies for labeling purposes. However, free or labeled avidin not only binds to conjugated biotin but also to endogenous biotin, thus causing high background staining in tissues rich in endogenous biotin [91]. Therefore, a biotin block (protein block step) is necessary to ensure good staining quality. Protein blocking was performed using a commercially available protein block solution. As protein block is highly susceptible to high temperatures, the block solution had to be stored on ice during use and kept refrigerated. Tissue slides were incubated with the protein block solution in a closed humid chamber for 10 minutes at room temperature. The solution was shaken off after the incubation.

5.3.2.3 *Antibody Application*

During the entire immunostaining process, all antibodies had to be stored on ice to prevent destruction. Three adjacent tissue slides were incubated for 75 minutes with the primary antibodies (200µl). Following the primary incubation, the liquids were tapped off, slides were rinsed and then buffer washed with PBS for 5 minutes. The next incubation step involved staining with biotinylated secondary antibodies for 30 minutes. The third incubation step, an Avidin-/Biotin-/Peroxidase- complex (ABC) was applied to all three slides for 30 minutes

5.3.2.4 *Visualization and Counterstain*

All tissue slides were incubated with 250µl DAB per slide for 10 minutes. For best color results, the DAB solution had to be prepared 24 hours prior to use and stored in a dark

environment, as DAB is highly light-sensitive. After DAB-application, the tissue slides were rinsed in deionized H₂O (3x 6 dips) and counterstained with Methyl Green for 2 minutes. Tissue dehydration was performed using the following solutions:

- Ethanol 100% 10 dips
- Ethanol 100% 10 dips
- Ethanol 100% 10 dips
- Xylene 5 min
- Xylene 5 min

All slides were covered with permanent mounting media and slipped with cover slides while still wet. The slides were left to dry overnight, before they could be examined with a microscope. Table A1 in the Appendix section summarizes the staining process for the three antibodies used in this study.

5. 3. 3 Prostate Immunomarker Stability after ¹H HRMAS NMR Spectroscopy

Previous studies demonstrated that ¹H HRMAS MRS does not destroy the tissue architecture of a sample, thus allowing for unbiased subsequent histopathological evaluation of a scanned tissue piece [16, 49]. However, until now, the immunohistological potential and quality of previously scanned tissue has not been evaluated.

In an attempt to verify that the quality and assessability of the proposed prostate immunomarkers, P504S, CK903 and p63, was not impacted by prior performance of ¹H HRMAS MRS, and that these markers were suitable for post-spectroscopic IHC, 28 paired prostate tissue sections from 14 samples were studied. Of each sample, one tissue section (“scanned”) was subjected to ¹H HRMAS MRS scanning before subsequent performance of IHC, using the designated immunomarkers on three adjacent tissue slides. The second section of each sample (“unscanned”) was processed with IHC, without prior ¹H HRMAS MRS. To ensure comparability of the IHC results, the “scanned” and “unscanned” sections from each sample were processed and immunostained simultaneously. Following the IHC procedure, the immunostaining quality and evaluability was judged for each tissue slide by an experienced pathologist using a 5-point scale (1 = poorest possible staining quality, 5 = highest possible staining quality). The evaluation of quality was based on staining intensity, preservation of tissue architecture and amount of background staining. Ultimately, the quality scores of all

immunostainings were compared for of each pair of matched “scanned” and” unscanned” slides.

5.3.4 Qualitative IHC Analysis

Qualitative analysis of the immunostainings was performed using an Olympus BX41 Microscope Imaging System (Olympus American, Inc., Melville, NY). All three adjacent slides of each individual sample were evaluated for presence (+) or absence (-) of staining. The samples were then histopathologically classified (Table 4). Presence of P504S-staining with absence of CK903- and p63- positive glands was considered characteristic of a cancerous tissue sample. In contrary, absence of P504S and presence of the benign tissue markers was classified as non-cancerous condition. Benign Prostate Hyperplasia (BPH) is characterized by (mostly incomplete) loss of positivity of the benign immunomarkers and concurrent absence of P504S-staining. A Prostate Intraepithelial Neoplasm (PIN) can be identified by positive P504S-immunostaining as well as positivity for benign immunomarkers, such as CK903 and p63.

All slides were centrally reviewed by a board-certified pathologist, to ensure correct evaluation.

Table 4: Qualitative Evaluation Diagnostic Table

P504S	CK903	p63	Diagnosis
+	-	-	cancerous
-	+	+	non-cancerous
-	-	-	BPH
+	+	+	PIN

5.3.5 Quantitative IHC Analysis

5.3.5.1 Quantitative IHC slide review

The IHC tissue slides were reviewed and evaluated by a board-certified pathologist to quantitatively determine the presence of immunostaining for each immunomarker. Intervals of 5% were used to judge the amount of stained glands in each cross-section.

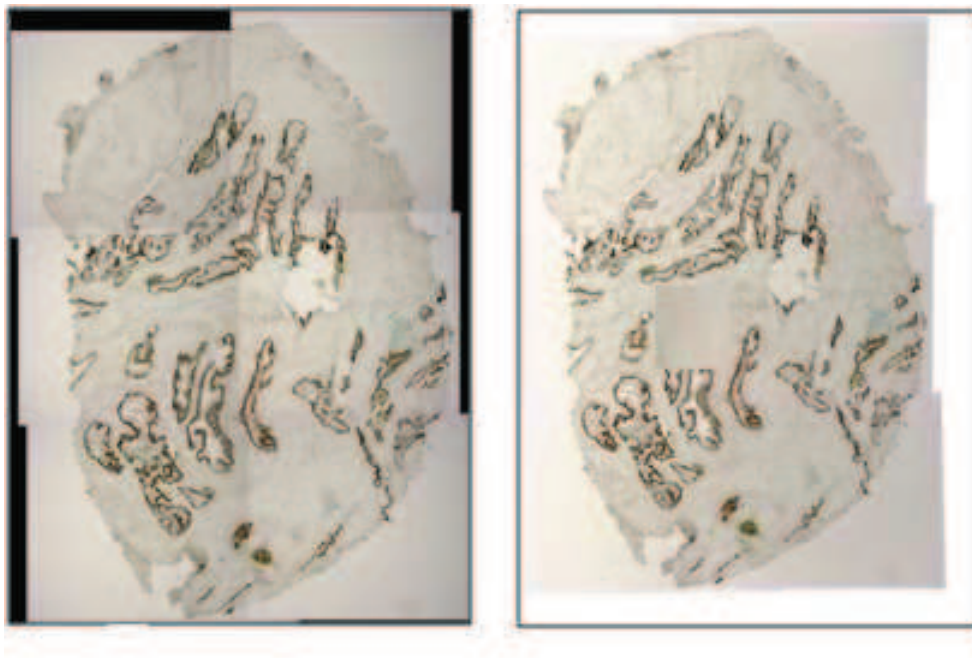
5.3.5.2 Computer-automated quantitative IHC analysis

To allow for an observer-independent, objective and time-efficient quantitative IHC analysis, a Quantitative Immunohistochemistry Analysis Program (QIAP) was developed for this study with the help of software engineer Yannick Berker (University of Aachen, Germany).

This program, based on the commercial software MATLAB (Version R2010a, Mathworks, Natick, MA, USA), was designed to automatically and objectively determine absolute and relative values of positively stained prostate gland epithelium, gland lumen area and stroma area in digital images of IHC tissue cross-sections.

5.3.5.2.1 Image generation and alignment

Digital images of IHC tissue slides were generated using an Olympus BX41 Microscope Imaging System (Olympus American, Inc., Melville, NY) in conjunction with the image analyzer MicroSuite™ (Soft Imaging System Corporation, Lakewood, CO). A 10-fold magnification was used. In order to capture an entire tissue slide, multiple photographs were taken of each cross-section. The individual images were aligned to create a single picture of each slide, using the open-source panorama photo stitching and merging software HUGIN (Version 0.8.0,[92]). The HUGIN software accomplishes stitching by using control points in several overlapping photos taken from the same source to align and transform the photos, so that they can be blended together- creating one larger image of an entire tissue slide. The stitching quality of HUGIN is superior over other alignment programs, including the MicroSuite™ multiple image alignment feature, as demonstrated in Figure 16.



A

B

Figure 16: Microscopic images of the same prostate tissue cross-section at 10-fold magnification-direct comparison of image alignment procedures: (A) MicroSuite™: less homogenous alignment, (B) HUGIN stitching software: homogenous alignment.

5.3.5.2.2 Image Analysis using QIAP

The image evaluation with QIAP included the following steps: 1. background detection and fitting, 2. total tissue area calculation, 3. epithelium detection, 4. lumen detection and 5. stromaarea calculation. The quantitative image analysis with QIAP was facilitated by an interactive user interface.

1. Background detection and fitting:

QIAP allowed the user to choose a picture from a designated file source via the interactive user interface. Each color image was then converted to a 8-bit grey-scale image with values between 0 and 255, with black being represented by 0. Background detection was then accomplished by assigning blocks with relatively homogenous, structure-less appearance as background.

The next step involved a fitting of background image intensities for correction of inhomogeneous illumination. This lighting correction was necessary to reduce inhomogeneity caused by microscopic digital imaging, and even more, the photo-stitching and alignment procedures. Overexposed pixels in the uncorrected images were excluded to avoid their impact on the illumination model. Next, the grey-level image intensities of non-overexposed background pixels were fitted to a polynomial surface model of variable degree. Starting with

a model with degree 4 along both x and y directions, the degree was automatically lowered iteratively if the fit failed. The surface model was then evaluated for every image pixel and the result was subtracted from the initial gray-scale image; overexposed image pixels were set to 0. Image intensities were then normalized by subtracting the mean value and dividing by the range to yield the corrected image C. Figure 18 shows the program output screens after the background detection (A) and fitting (B) steps.

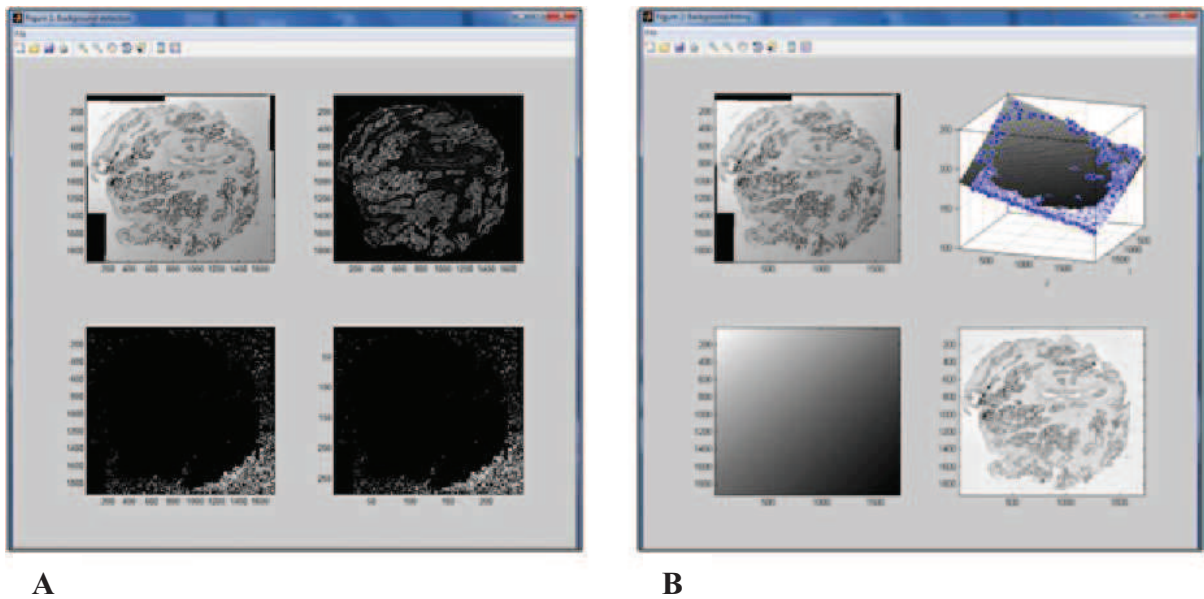


Figure 18: QIAP output screens for the background detection (A) and background fitting (B) steps

2. Total tissue area calculation:

A specific tissue-detection step was implemented by thresholding of a standard deviation image. In this image, each pixel was assigned the standard deviation of a block of 7x7 pixels containing it. Pixels with a standard deviation value greater than an empirically determined threshold (2.2) were then considered tissue. The resulting binary image was then post-processed by successive morphological operations, specifically 1) hole filling, 2) opening with a disc-shaped structuring element of radius 5 pixels, and 3) opening by reconstruction with a disc-shaped structuring element of radius 25 pixels. The tissue area was calculated by counting pixels in the resulting binary image. The total tissue value was displayed in the evaluation window (Figure 19).

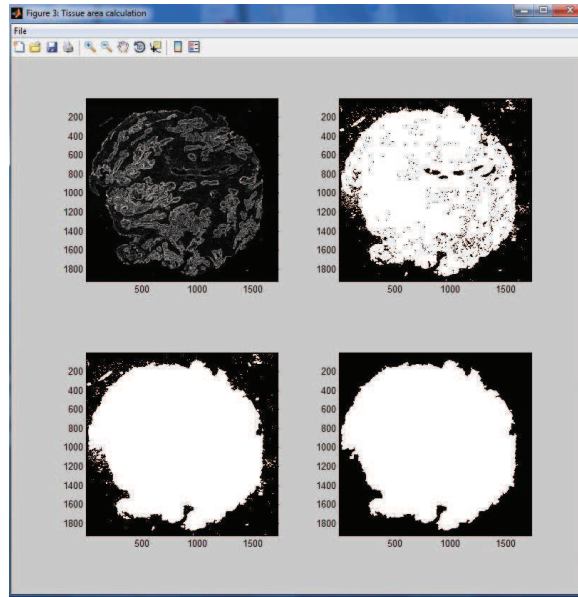


Figure 19: QIAP output screen for the tissue area detection and calculation steps

3. Detection and calculation of epithelium points:

Visualization with DAB causes a dark brown color in positively stained gland epithelia, which makes it possible to detect epithelium cells that express the respective immunomarker. Using a brightness threshold T , all picture points with gray-values below T threshold were classified as positive for staining in QIAP. A preset threshold can be adjusted interactively by the user via the user interface, if necessary. Threshold changes were instantly made visible by the program in the evaluation window, to facilitate determination of the ideal threshold. To obtain the most accurate results, the user needed to change the threshold to a value at which the tissue points that are determined to be positive by QIAP closely matched the stained epithelium in the original image.

After the detection of epithelium points, a correction step was performed to reduce artifacts (Figure 20). Assuming that actual tissue points are interconnected, all white picture point clusters with a diameter of less than a certain number N of points were removed. The value of N is preset to 5, but could be adjusted manually by the user to increase accuracy. Subsequently, all detected epithelium points were added and the total epithelium value as well as the percentage of epithelium points in the entire picture (total epithelium value divided by total tissue area) was calculated and displayed in the evaluation window (Figure 20).

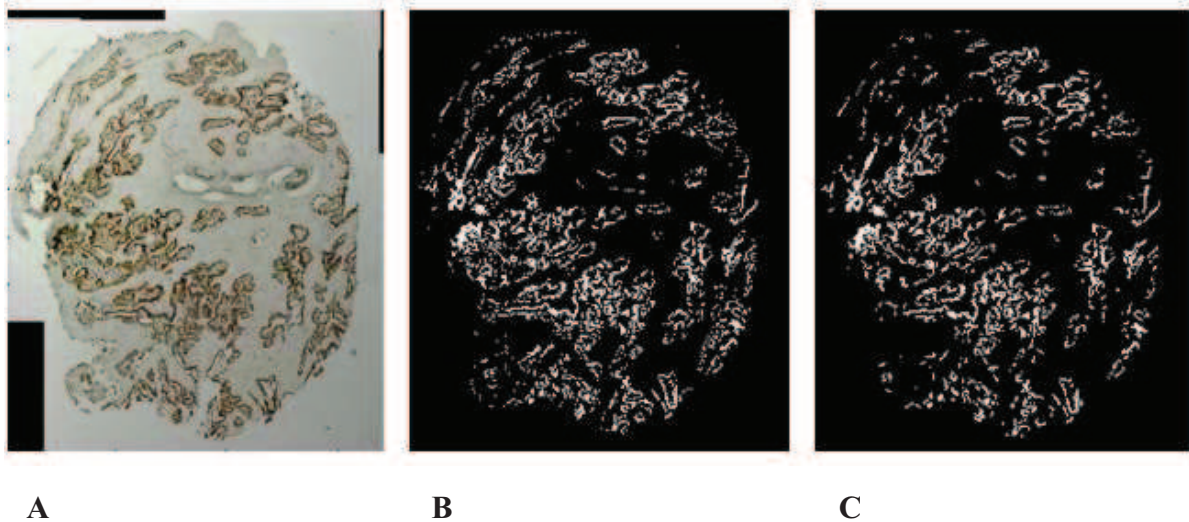


Figure 20: Output screens for the epithelium detection steps of QIAP: (A) original image, (B): after epithelium detection: all points considered epithelium points are displayed in white, (C) after artifact removal: epithelium points displayed in white, small independent white points have been eliminated.

4. Detection and calculation of lumen points:

In order to detect the luminal areas of the displayed prostate glands, the tissue boundaries needed to be as continuous as possible. In most cases however, due to staining issues or tissue rupture, detected boundary points did not quite align. Therefore, QIAP reconstructed the tissue boundaries by enlarging each boundary point to a diamond with a diameter of a number M of points. M was preset to 5, but its value could be adjusted manually by the user. Subsequently, diamond epithelium points that connect with other diamond points were bridged. Removing the diamond points, only epithelium points and bridges were left. In this way, a continuous tissue boundary was created, while keeping the number of epithelium points as accurate as possible (Figure 21). Next, the area between gland boundaries was filled to simulate the gland lumen. Picture points inside the boundaries were counted as lumen area. To reduce artifact effects on the image analysis, all white point clusters with less than a number K of points in diameter were again eliminated, as they were unlikely to belong to the prostate gland lumen. K was preset to 5, but could be manually adjusted by the user.

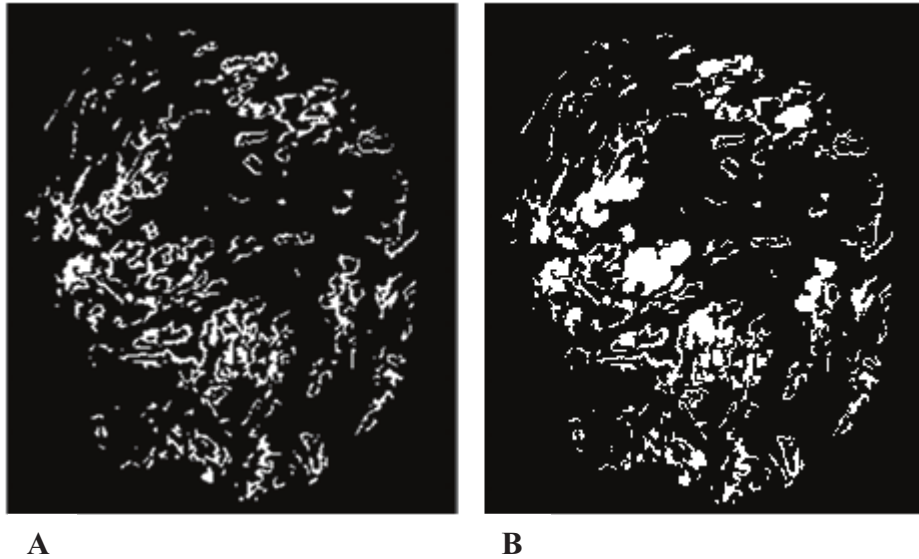


Figure 21: Output screens of QIAP: (A) after bridging step: white epithelium points are connected to near points, (B) after gland lumen detection and filling: all points belonging to gland lumina or epithelia are displayed in white.

The remaining lumen points were then counted and displayed in the evaluation window, as absolute and relative (lumen points divided by total tissue points) values.

5. Calculation of stroma area

The stroma area in the section can then be calculated from the total tissue value by subtracting the lumen points and epithelium point values. The stroma points value was displayed in the evaluation window as absolute and relative (stroma points divided by total tissue points) values. In summary, during a complete run, QIAP determined the tissue boundaries, detected and corrected the gland epithelium, detected and measured the gland lumen size and calculated the stroma area of the cross-section. All results were displayed in the output window (Figure 22).

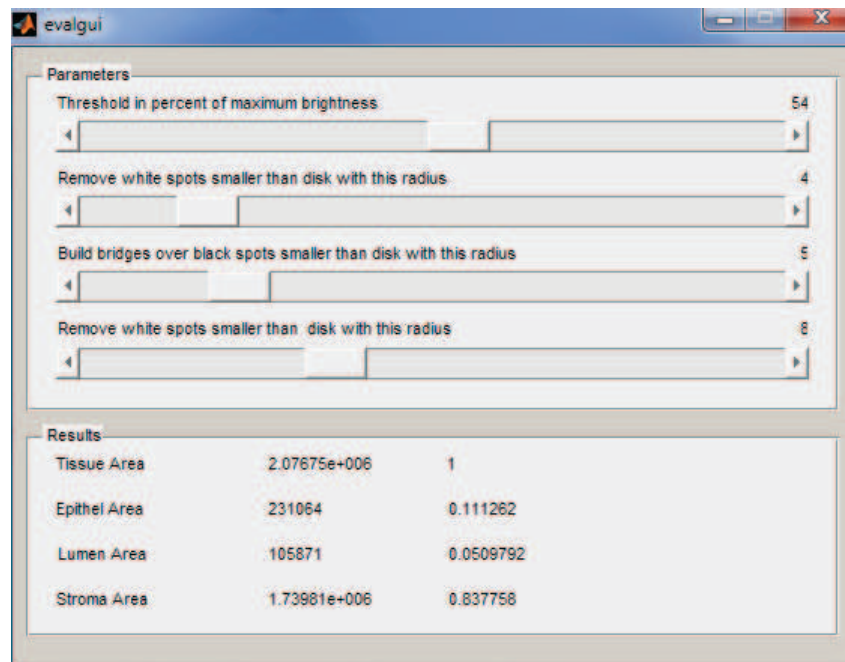


Figure 22: Interactive user interface of QIAP with adjustable parameters and results output section

The QIAP was designed to facilitate the quantitative evaluation of immunostained tissue slides, by automatically and objectively determining absolute and relative values of positively stained prostate gland epithelium, gland lumen area and stroma area. Cancerous epithelium as well as benign epithelium absolute value and percentage were determined by analyzing two adjacent slides stained with P504S and CK903 respectively, with the program. Ultimately, a cancer ratio C was calculated, specified by cancer epithelium as a ratio of all epithelium (cancerous + benign), which could be used for further analysis.

5.3 Quantitative histopathology

Conventional histopathology, using Hematoxylin & Eosin (H&E) - staining, presents the gold standard of prostate tissue pathological analysis. For reference standardization purposes, a quantitative analysis of conventional histopathology was included in this study. All tissue slides of each individual sample, except the three cross-sections used for IHC, were stained, using a standard H&E-staining procedure (Table A2, Appendix section). An experienced pathologist was asked to judge the percentages (in 5%- intervals) of cancerous glands, benign glands and stroma present in each slide. The percentages derived from each slide were averaged for each case, resulting in quantitative measures of cancer and benign prostate glands in the samples.

For future referencing purposes, a quantitative analysis of each complete sample is not time-efficient and manageable. Therefore, one aim of this study was to determine whether it would be feasible to use only one adjacent tissue slide of each case for referencing purposes. For that, the results of quantitative histopathology analysis of a single adjacent slide were compared to the averaged percentages of the corresponding case.

5.4 Identification of Prostate Cancer Metabolomic Markers

In order to identify potential metabolomic markers of prostate cancer, relative spectral intensities obtained from ^1H HRMAS MRS had to be referenced against histopathological results obtained from the corresponding tissue samples. In previous studies, conventional histopathology was commonly used as reference standard [16], due to its broad clinical utility and applicability. The present study shows a novel approach to identify metabolomic markers of PCa, by using quantitative IHC as reference standard instead of conventional histopathology.

For that, the spectral intensities of 36 regions of interest (described in 4.2.3.) of each case were correlated with a cancer ratio calculated from quantitative IHC of the same tissue sample. The cancer ratio was defined as percentage of cancer epithelium (as determined by QIAP) divided by the amount of all epithelia, cancerous as well as benign (by QIAP), and served as measure for quantitative pathology as determined by IHC. The correlation between cancer ratio and the corresponding spectral intensities from each sample was performed using a linear regression model.

5.5 Patient Outcomes and Recurrence Categories

Five years after the initial diagnosis and surgery, the patient medical records were reviewed again retrospectively, in order to evaluate the patients' outcome. Any adjuvant treatment administered was recorded as well as clinical signs of recurrence or metastasis. Furthermore, the date of last follow-up, PSA-levels as well as vital status at last follow-up were determined. Overall survival (OS) was calculated as time from initial diagnosis to death, or date of last-follow up in survivors. Recurrence was classified into four categories, according to their presence and absence of PSA-elevation, clinical symptoms and metastases (Table 5).

Table 5: Categories of recurrence

Category	Description
1	no evidence recurrence
2	PSA-elevation without clinical symptoms
3	PSA-elevation with clinical symptoms, no metastasis
4	metastatic disease

The outcome measures ‘category of recurrence’ and OS were correlated with the spectral intensities in order to determine metabolomic markers of recurrence and survival.

5.6 Statistical Analysis

Statistical analysis was performed using the statistical software JMP 10 (SAS institute Inc., Cary, NC, USA) was used.

Linear fits were used to test the correlations between quantitative histopathology and quantitative IHC, as well as between quantitative IHC as determined by a pathologist and as calculated by QIAP. In order to identify metabolomic markers of PCa from the spectral data and quantitative IHC, spectral intensities and cancer epithelium percentages, established by quantitative image analysis, were correlated with paired T-tests. Univariate analysis between the spectral intensities of each of the 36 regions of interest and CaE% as determined by QIAP was performed. Outcome measures were correlated to spectral intensities of the 36 regions.

A p-value of less than 0.05 was considered as significant for all tests.

6 Results

6.1 Patient demographics

The patient cohort was characterized by a mean age of 62.02 years (median 63, range 47-75). The mean pre-operative PSA was 5.79, range 0.6 -19.8, STD 2.88). The histopathological stage was scored as T1c in 9 cases (18.75%), T2a in 7 cases (14.58%), T2c in 20 cases (41.67%), T3a in 9 cases (18.75%) and T3b in 3 cases (6.25%). Only three patients (6.17%) had metastatic disease. The majority of patients had a low GLEASON score of 6 (23, 47.92%) or 7 (22, 45.83%), consistent with a relatively undifferentiated, less malignant pathology, while only one patient had a GLEASON grade 8 (2.08%) and two patients a GLEASON 9 (2, 4.17%) - indicative of well differentiated, malignant pathology (Table 6).

Table 6: Patient demographics

Median age (range) in years	63 (47 -75)
Mean age, SD	62.02, 6.22
Diagnosis (%)	
T1c	9 (18.75)
T2a	7 (14.58)
T2c	20 (41.67)
T3a	9 (18.75)
T3b	3 (6.25)
Metastasis (%)	3 (6.25)
GLEASON score (%)	
6	23 (47.92)
7	22 (45.83)
8	1 (2.08)
9	2 (4.17)
PSA pre-op, mean (range)	5.79 (0.6 – 19.8)
Adjuvant treatment (%)	
Radiotherapy	8 (16.67)
Androgen deprivation therapy	5 (10.42)
Chemotherapy	1 (2.08)

6.2 Spectroscopy Results

Spectra from 46 of the 51 samples studied could be processed for evaluation. Five spectra had to be excluded due to insufficient spectral quality. Representative examples of spectra obtained in this study can be viewed below (Figure 33-37). All spectra were found to have a distinguishable lactate double peak signal, which was used for referencing (peaks set to 1.32 and 1.34). Some spectra showed characteristic features of benign prostate tissue, such as moderate double peak signals at 2.52 and 2.71, representing citrate, and relatively low choline and creatine signals at 3.18 and 3.02, respectively (Figure 33, 37). Other spectra presented features of malignant conditions, such as decreased citrate, elevated choline and creatine signals and elevated lactate (Figure 34, 35). In order to accurately quantify the spectroscopic data, relative spectral intensities were measured from the 46 spectra in the 36 designated regions of interest described in 4.2. A complete table with all relative spectral intensities can be found in the Appendix section.

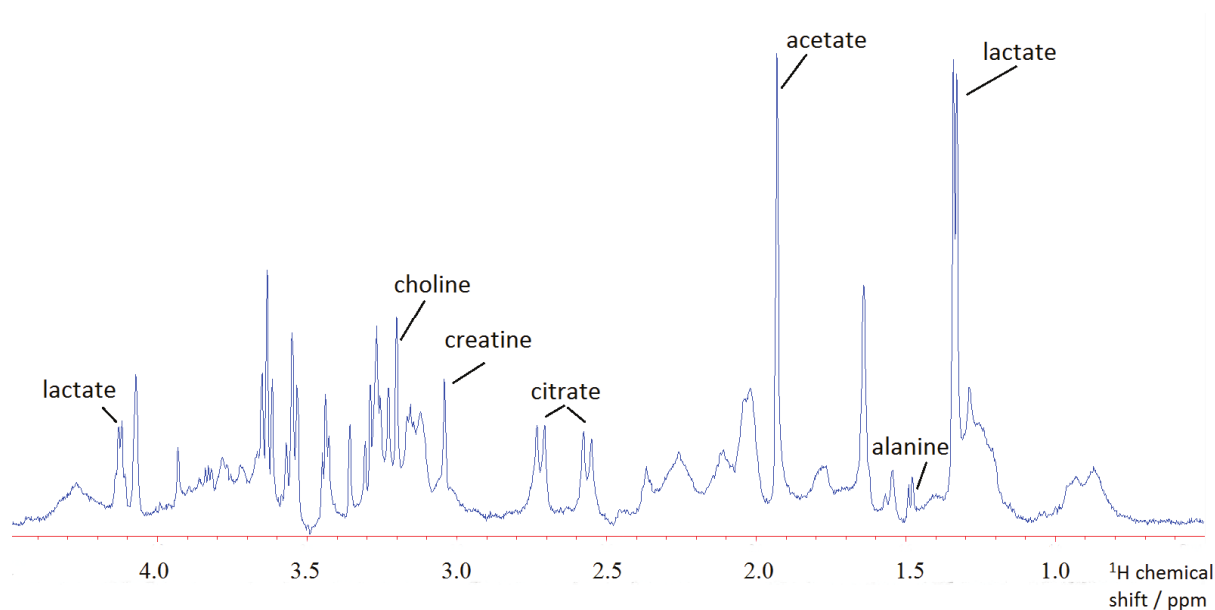


Figure 23: ^1H HRMAS MR spectrum of a prostate tissue sample at 14T: Prominent lactate (1.34 and 1.32 ppm) and acetate (1.92 ppm) peaks, clearly distinguishable citrate doublets (2.52 / 2.71 ppm). This spectrum is suggestive of a predominantly benign prostate tissue sample.

+

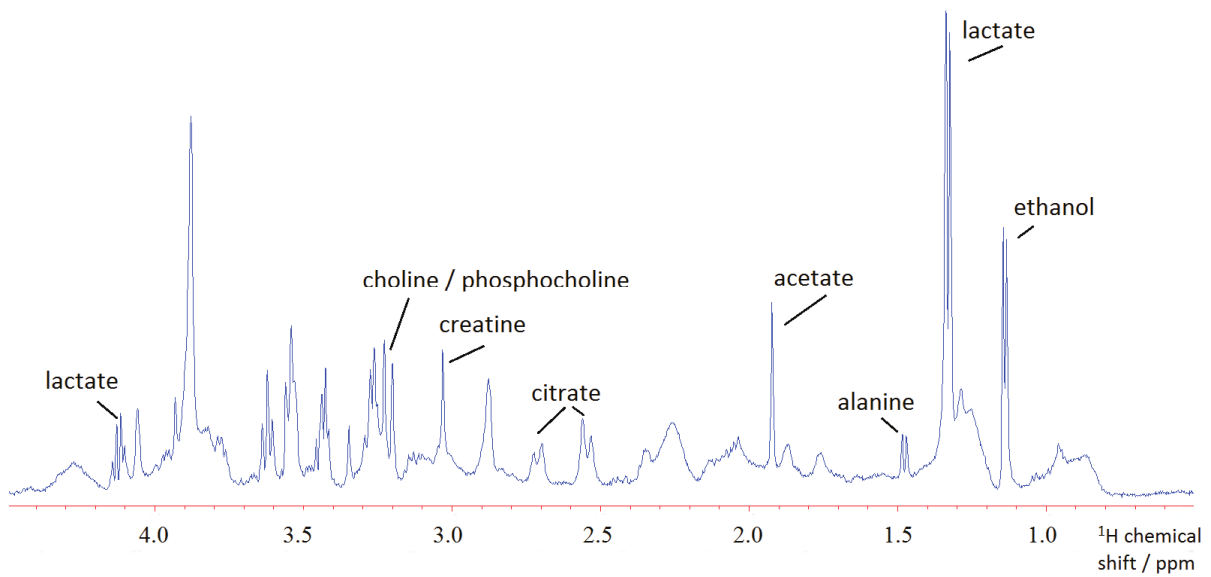


Figure 24: ^1H HRMAS MR spectrum of a prostate tissue sample at 14T: Prominent lactate peak (1.34 and 1.32 ppm) in contrast to the spectrum in figure 23, the acetate peak (1.92 ppm) is much lower and the citrate peaks are decreased. The choline to creatine ratio has decreased. The ethanol peak at 1.15 ppm is most likely caused by contamination during tissue handling. This sample is suggestive of a malignant condition, such as PIN or prostate cancer.

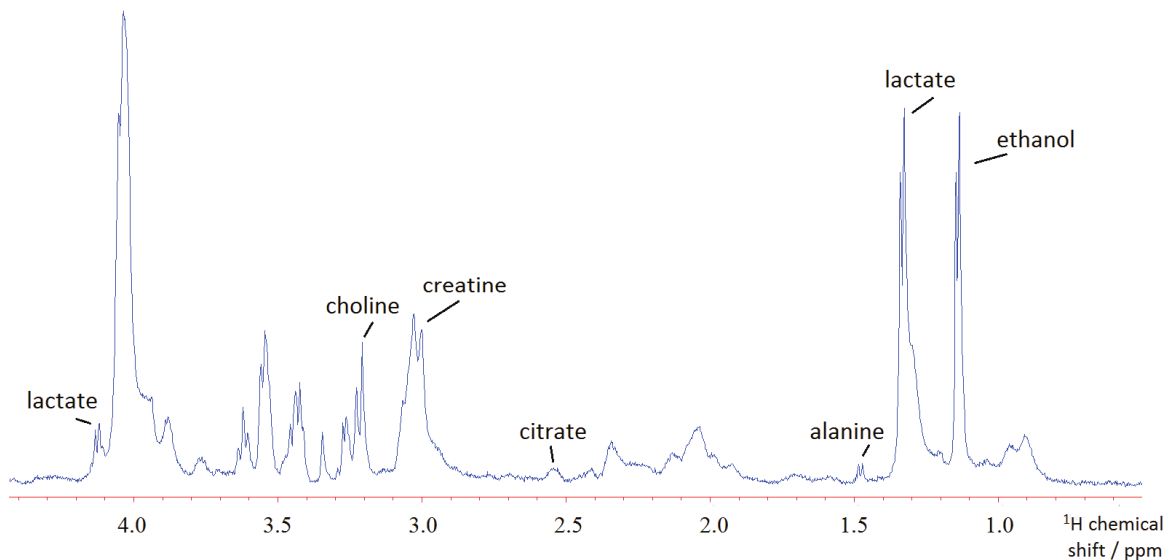


Figure 25: ^1H HRMAS MR spectrum of a prostate tissue sample at 14T: Decreased citrate signals. High signal of ethanol, likely due to contamination. This sample is suggestive of a cancerous condition.

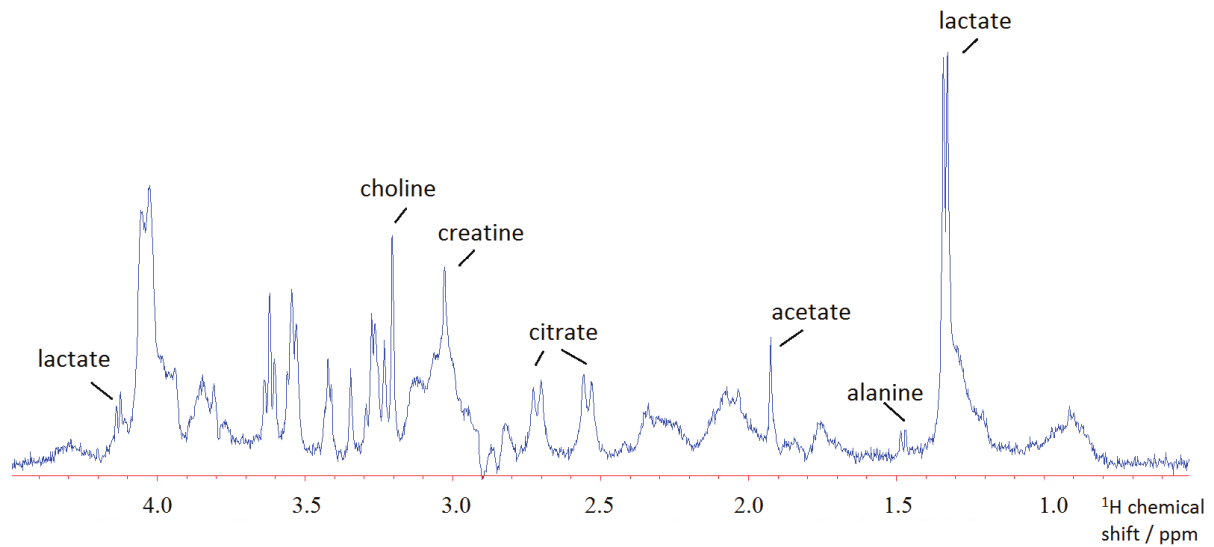


Figure 26: ^1H HRMAS MR spectrum of a prostate tissue sample at 14T: Prominent lactate peak (1.34 and 1.32 ppm), prominent citrate peaks, increased choline to creatine ratio. This spectrum is suggestive of a benign sample or a benign condition such as BPH.

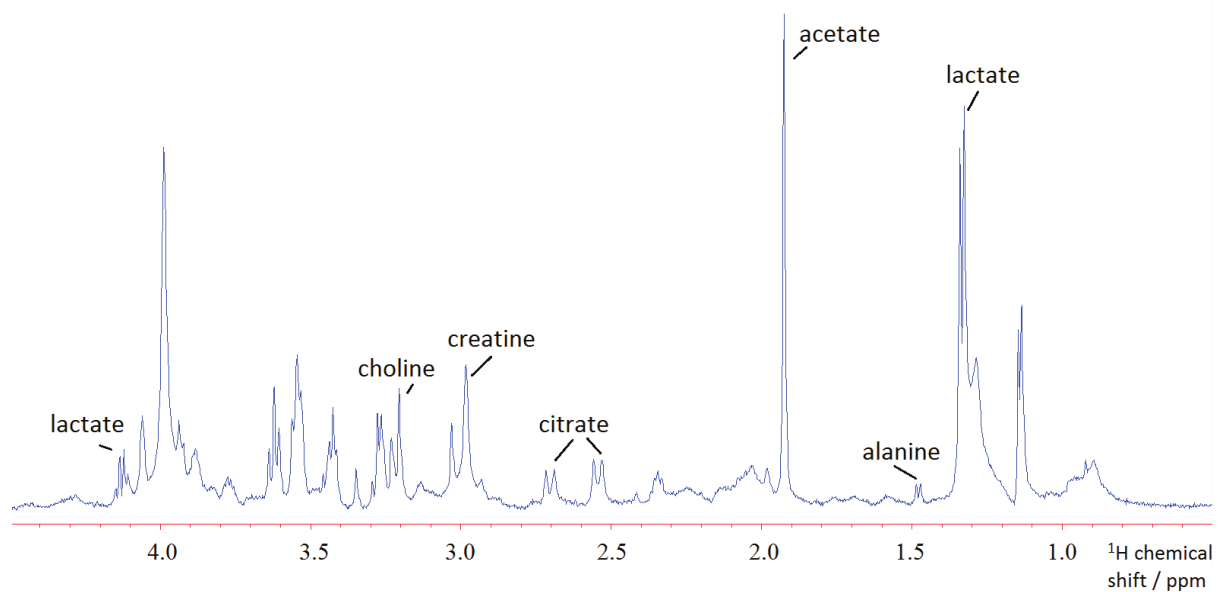


Figure 27: ^1H HRMAS MR spectrum of a prostate tissue sample at 14T: Prominent lactate peaks, (1.34 and 1.32 ppm), extraordinarily prominent acetate peak at 1.92 ppm, distinguished citrate signals and a positive creatine to choline ratio. This is a spectrum indicative of a benign sample.

6.3 Immunohistochemistry

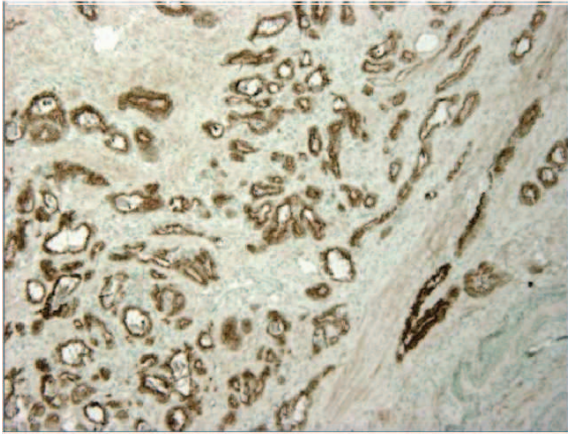
6.3.1 Evaluation of Prostate Immunomarker Stability after ¹H HRMAS MRS

Three cases of 28 paired tissue samples, which were studied for the evaluation of prostate immunomarker stability after ¹H HRMAS MRS, had to be excluded from further analyses due to insufficient gland epithelium in the cross-sections (stroma tissue only).

The remaining 11 cases were used for the evaluation of quality and accessibility by the pathologist.

P504S- positive staining, indicative of cancerous tissue, appeared in a distinct light brown, granular staining pattern in the tissue slides. CK903 on the other hand caused a clear, dark brown staining in the cytoplasm of benign epithelium basal cells, leaving cancerous tissue unstained. P63, known as a basal cell marker, stained nuclei of benign prostate gland epithelium only. Due to its scattered nuclear staining pattern and the extensive background staining in most slides, the evaluation of this marker was complicated. Figure 28 illustrates the appearance of the three chosen prostate immunomarkers, P504S, CK903 and p63, in “unscanned” versus “scanned” tissue sections of the same prostate sample.

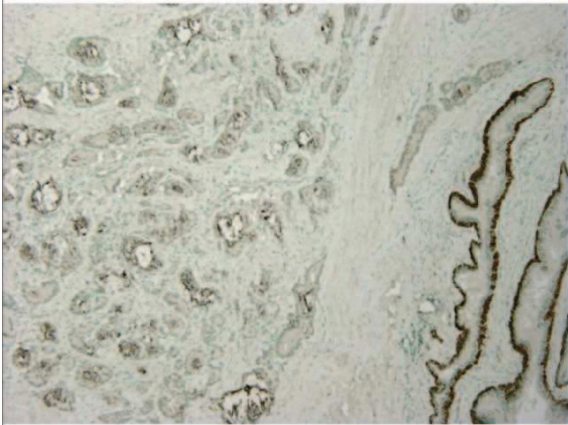
The evaluation of quality was based on staining intensity, amount of background staining and similar criteria, using a 5- point scale. Table 6 summarizes the findings in the 28 paired tissue samples.



A1: Unscanned - P504S



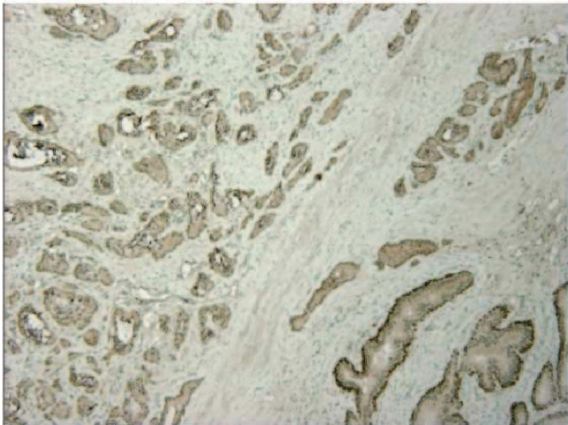
A2: Scanned - P504S



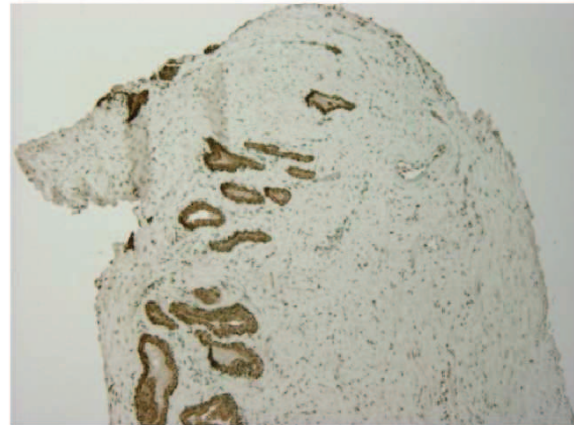
B1: Unscanned - CK903



B2: Scanned - CK903



C1: Unscanned - p63



C2: Scanned - p63

Figure 28: Immunohistochemical staining with the immunomarkers P504S (A1, A2), CK903 (B1, B2) and p63 (C1, C2) in prostate tissue cross-sections following ^1H HRMAS MR spectroscopy ('scanned') and without prior scan ('unscanned').

Table 7: Quality of immunostainings in 14 scanned and matched unscanned tissue samples*

Case number	Unscanned			Scanned			Histopathological diagnosis
	P504S	CK903	P63	P504S	CK903	P63	
1	5	5	5	n	5	3	benign + cancerous
2	5	5	4	5	n	2	benign + cancerous
3	n	5	5	n	5	4	benign
4	n	5	4	n	5	4	benign
5	n	5	4	n	5	4	benign
6	n	5	4	n	5	5	benign
7	n	5	4	n	5	3	benign
8	5	5	5	5	5	4	PIN
9	5	n	n	5	n	n	cancerous
10	n	5	5	5	5	4	benign + cancerous
11	n	5	4	n	5	3	benign
12	n	n	n	n	n	n	no epithelium
13	n	n	n	n	n	n	no epithelium
14	n	n	n	n	n	n	no epithelium

* *n... no staining present in cross-section*

When comparing the quality evaluation scores between “scanned” and “unscanned” tissue samples for each of the three immunomarkers, no differences in the quality and evaluability could be found between the paired samples for both P504S and CK903. The immunostaining quality in the tissue sections stained after ¹H HRMAS MRS was as good as in the instantly stained samples, graded a perfect score of 5 in all cases.

For the third immunomarker p63 however, the quality and accessibility of the immunostainings showed significant differences between the “scanned” and “unscanned” tissue sections of each case (p=0.6728), found significantly decreased in most tissue samples after ¹H HRMAS MRS.

Due to these results, P504S and CK903 were determined stable for IHC use after prior ¹H HRMAS MRS. However, because of its decreased IHC quality and accessibility after ¹H HRMAS MRS, the marker p63 was excluded from all further immunohistochemical analyses.

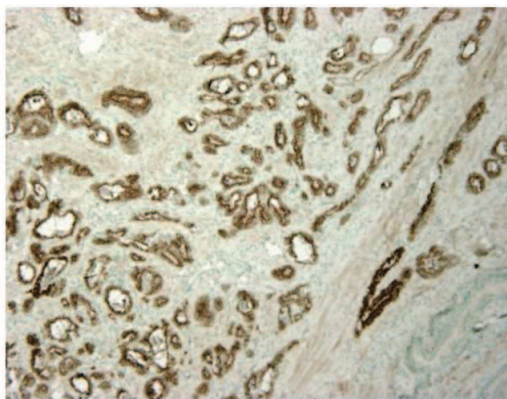
6. 3. 2 Qualitative Immunohistochemistry

Using the immunomarker P504S to identify cancerous glands and CK903 to stain benign tissue, it was possible to distinguish between different histopathological conditions present in the sample cohort. All 51 cases were evaluated for the presence or absence of P504S- and CK903- staining, respectively. The presence of P504S- and absence of CK903- immunostaining in the corresponding tissue slides was considered a positive qualitative diagnosis of PCa in the sample. Absence of P504S and presence of CK903, however, was classified as benign condition. Some of the tissue samples contained both benign and cancerous glands adjacent to each other. These cases were determined “mixed” immunohistopathology. Semi-malignant conditions, such as PIN were characterized by positive P504S- immunostaining as well as presence of staining for CK903. The benign condition BPH could be identified by absence of P504S and loss of CK903- immuno-positivity, mostly incomplete.

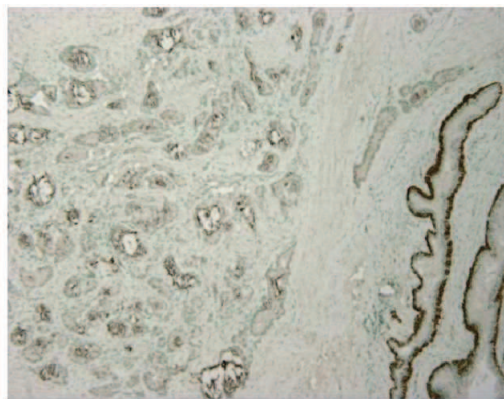
Out of the 51 cases evaluated, six paired samples could not be diagnosed accurately due to the absence of glandular epithelium in the tissue. These cases were classified as “stroma only” and were excluded from further analysis. The remaining 45 cases showed presence of glandular epithelium and a positive color reaction in at least one of the two immunostainings. The following section illustrates the results of the qualitative IHC evaluation.

Pattern 1: “Mixed” immunohistopathology: both benign and cancerous glands

In five cases, positive immunostaining for both P504S and CK903 was found in the glandular epithelia in mutually exclusive glands, suggesting the presence of both cancerous and benign glands in the samples (Figure 29). Light brown, granular staining in the P504S-slide and absence of staining in the exact same glands in the CK903-slide proofed the presence of cancer in the tissue. Other glands that were found to have a dark brown staining in the cytoplasm of the epithelium basal cells showed no signs of a color reaction on the corresponding P504S- slide, validating a benign condition.



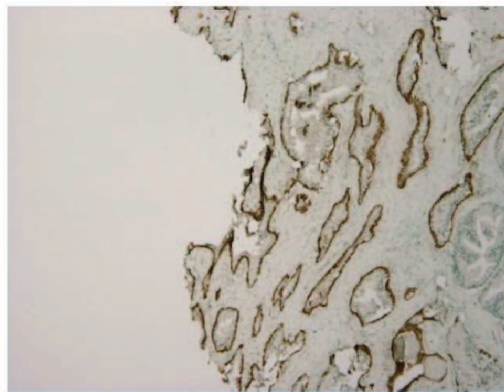
Sample 1: P504S



Sample 1: CK903



Sample 2: P504S



Sample 2: CK903

Figure 29: Co-existence of benign and malignant epithelium in two examples of tissue cross-sections after IHC with P504S (left) and CK903 (right).

Pattern 2: Benign glands only

No signs of a color reaction on the P504S slides but dark brown cytoplasmic staining in glandular basal cells in the corresponding CK903 slides indicated the presence of solely benign glands in the tissue sample (Figure 30). The majority of cases, 28 out of 44, showed this staining pattern indicating a predominantly benign sample cohort.

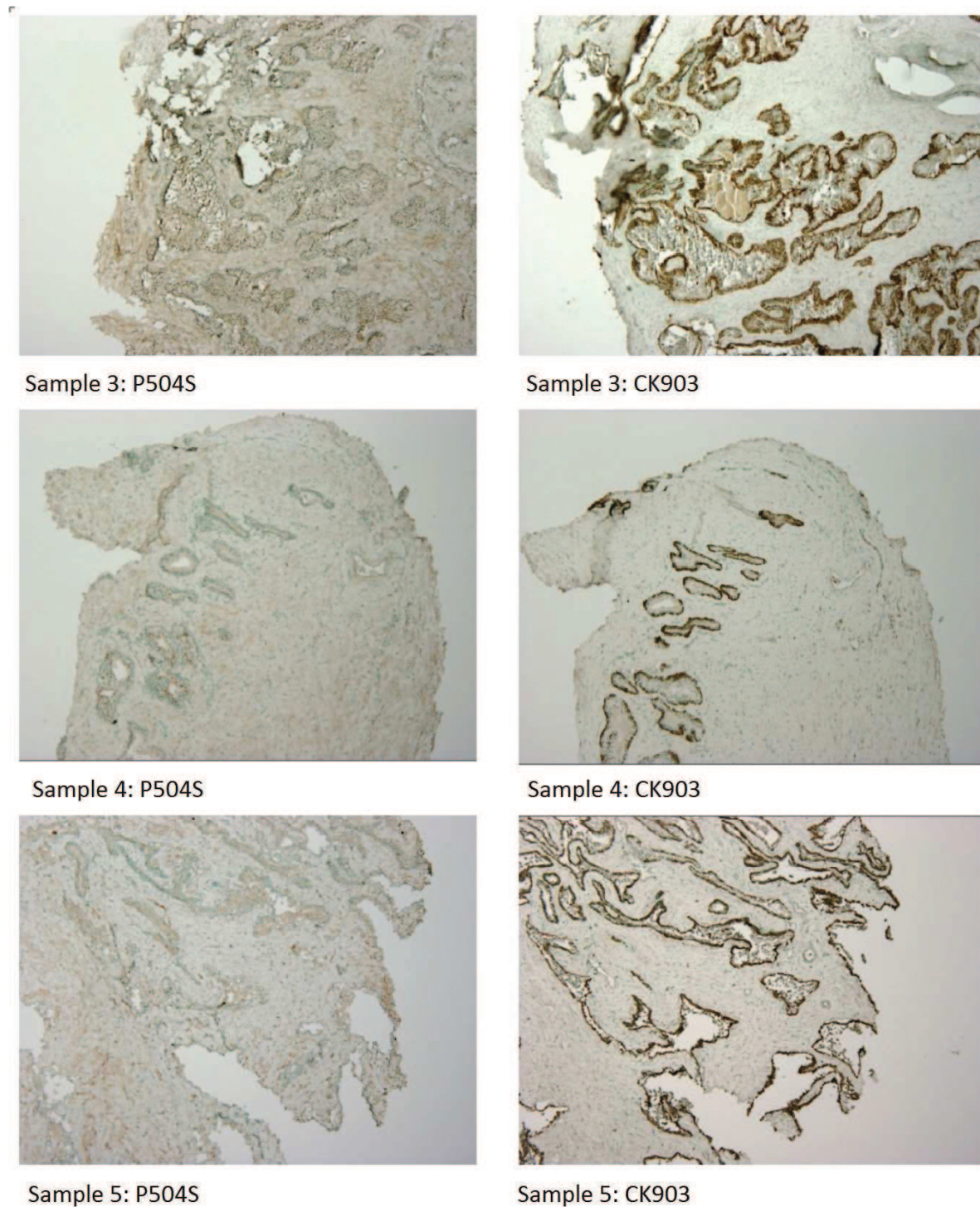
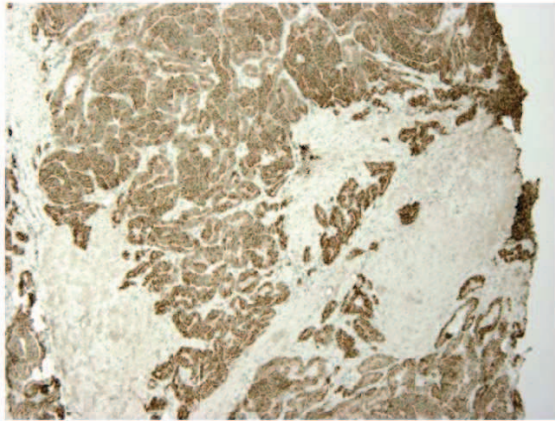


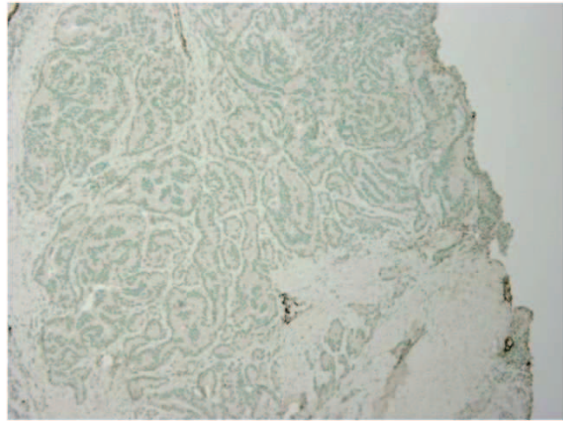
Figure 30: Three prostate tissue samples after IHC showing absence of P504S- staining (left panels) and clearly positive staining for CK903 (right panels), indicative of benign tissue.

Pattern 3: Cancerous glands only

Light brown granular staining in glands of the P504S slide with absence of any color reaction in the corresponding CK903 slide indicated the presence of solely cancerous glands in only one tissue sample in the entire cohort (Figure 31).



Sample 6: P504S

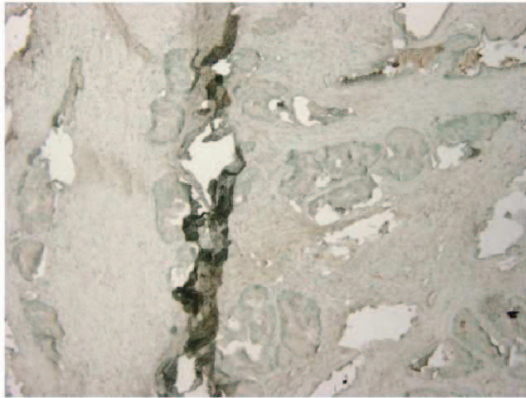


Sample 6: CK903

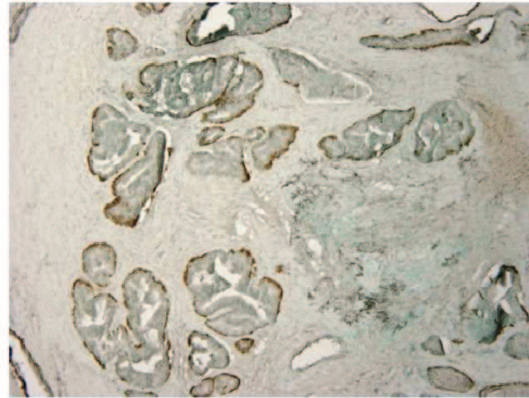
Figure 31: One single case in the cohort showed positive immunostaining for P504S (left) and negative reaction for CK903 (right), indicative of cancerous epithelium.

Pattern 4: Benign Prostate Hyperplasia (BPH)

Five cases in the cohort showed a staining pattern which was characterized by absence of staining in the P504S slides and an incomplete loss of CK903- positivity in the corresponding slides. This pattern was indicative of the benign condition BPH, in which the glands lose their normal cytokeratin expression (Figure 32).



Sample 7: P504S



Sample 7: CK903



Sample 8: P504S



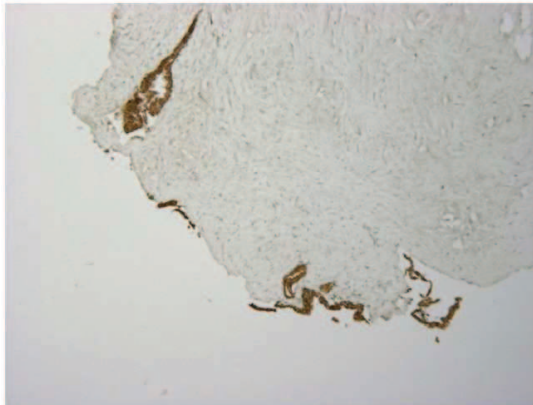
Sample 8: CK903

Figure 32: Two examples of the characteristic IHC- staining pattern indicative of BPH: absence of immunostaining for P504S (left) and partly positive CK903- staining due to loss of cytokeratin-expression (right).

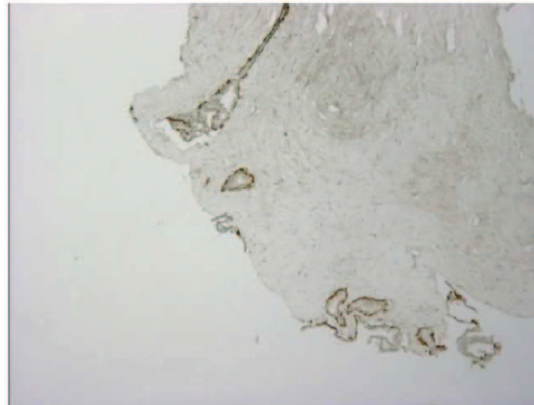
Pattern 5: Prostate Intraepithelial Neoplasia (PIN)

A very distinct staining pattern could be seen in five samples: Partly positive color reaction in the P504S slide with a partly positive staining for CK903 in the same glands in the corresponding slide. This pattern is typical for Prostate Intraepithelial Neoplasia, where the normal cytokeratin expression is reduced and P504S- expression is increased (Figure 33).

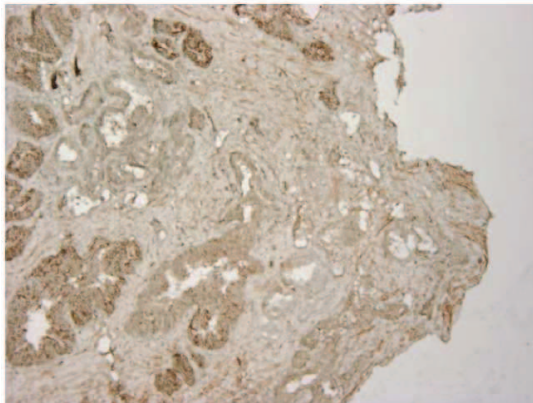
Figure 34 summarizes the distribution of qualitative pathologies in the sample cohort.



Sample 9: P504S



Sample 9: CK903



Sample 10: P504S



Sample 10: CK903

Figure 33: Characteristic pattern of IHC- staining for PIN: Positive staining in both P504S and CK903- stained tissue cross- sections in corresponding gland epithelium.

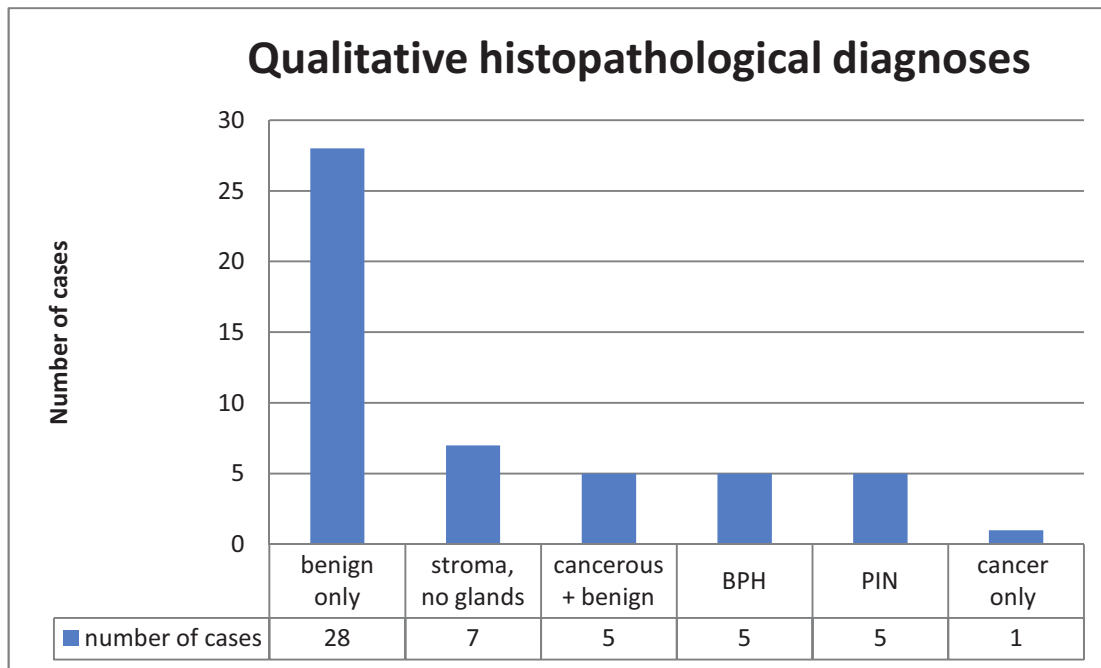


Figure 34: Distribution of qualitative histopathological diagnoses in the sample cohort

6.4 Quantitative Immunohistochemistry

6.4.1 Quantitative IHC Slide Review

Of the 51 evaluated cases, 15 exhibited positive staining for P504S, however, most of them only in a small percentage of tissue (only 5 cases had greater than 20% positively stained tissue). The majority of cases (42) showed CK903- positive tissue, corresponding with the previous findings in the qualitative IHC analysis. Twelve cases showed both positive staining for P504S as well as for CK903. Out of these, seven cases exhibited staining for both markers in the exact same glands in the corresponding slides, indicating the presence of PIN in the tissue. In three cases, mutually exclusive glands showed P504S- and CK903- immunopositivity, indicating the presence of both cancerous and benign tissue. Two cases showed unspecific positive staining for P504S in predominantly benign tissue. Seven cases showed no gland epithelium and therefore, no positivity for immunostaining.

The results of the quantitative IHC slide review can be viewed in Table 8.

Table 8: Centrally reviewed percentages of positively stained tissue

Sample #	P504S-positive (%)	CK903-positive (%)	Stroma (%)
1	0	8	92
2	35	15	50
3	0	30	70
4	0	20	80
5	0	40	60
6	0	60	40
7	25	7.5	75
8	0	15	85
9	0	40	60
10	0	15	85
11	0	0	100
12	0	15	85
13	10	40	50
14	0	20	80
15	40	0	60
16	0	0	100
17	0	5	95
18	5	15	80
19	0	0	100
20	0	12	88
21	15	30	55
22	0	8	92
23	0	0	100
24	8	32	60
25	0	20	80
26	0	28	72
27	4	16	80
28	0	20	80
29	0	10	90
30	5	0	95
31	2	20	80
32	0	15	85
33	0	20	80
34	0	10	90
35	18	42	40
36	20	20	80
37	0	40	60
38	7.5	17.5	75
39	0	10	90
40	0	15	85
41	0	30	70
42	0	50	50
43	0	9	40
44	0	20	80
45	20	0	80
46	0	20	80
47	0	12	88
48	6	15	85
49	0	0	100
50	0	0	100
51	0	0	100

6. 4. 2 Computer-Automated Quantitative IHC Evaluation using QIAP

Observer-independent and objective quantitative IHC analysis was carried out using the MATLAB-based self-developed evaluation program QIAP (described in 4.3.4.2). Absolute and relative values of positively stained prostate gland epithelium, gland lumen area and stroma area in both P504S- and CK903- immunostainings were determined from digital images of IHC- processed cross-sections.

As P504S- staining generally indicates the presence of cancerous epithelium, the percentage of cancer epithelium (CaE%) was estimated from the quantitative values of P504S- positively stained tissue. Similarly, the percentage of benign epithelium (BenE%) was derived from the CK903- positively stained tissue. These estimations were made with the knowledge in mind that some P504S- positive conditions might not be cancer and some actually benign conditions might not express CK903.

Ultimately, for each case, a cancer ratio was calculated from the percentages of cancer epithelium and benign epithelium: In order to determine the value of cancerous tissue in each case, the CaE% was divided by the sum of CaE% and BenE%, representing the entire epithelium in each case. The individual percentages of cancerous and benign epithelia for each case are displayed in Table 9.

Table 9: Results of the quantitative IHC evaluation using QIAP

Sample #	Cancer Epithelium % (CaE%)	Benign Epithelium % (BenE%)
1	0.086	6.012
2	12.031	7.677
3	0.106	13.932
4	1.425	6.485
5	0.541	11.221
6	0.652	12.413
7	0.728	1.539
8	2.581	6.593
9	3.221	12.670
10	0.817	11.406
11	1.241	0.513
12	1.960	8.334
13	2.096	6.821
14	1.801	9.489
15	36.926	0.130
16	0.682	0.721
17	1.762	3.798
18	2.452	6.543
19	1.378	3.500
20	0.848	3.1967
21	1.737	3.088
22	8.263	5.943
23	0.381	4.554
24	0.015	0.046
25	0.020	3.619
26	0.329	1.182
27	4.015	4.832
28	0.040	5.186
29	1.509	3.887
30	0.934	3.163
31	8.876	6.604
32	4.402	6.895
33	0.698	5.719
34	0.188	13.685
35	0.467	4.519
36	0.371	14.235
37	0.329	2.390
38	0.634	6.610
39	0.782	0.646
40	2.532	0.414
41	0.469	4.278
42	0.147	7.660

6.5 Quantitative Histopathology

Quantitative analysis of conventional H&E-stained tissue slides from each of the 51 cases was conducted to determine the percentages of cancerous and benign prostate glands in the cross-sections. The percentages of all slides were averaged for each case (Table 10). To evaluate the utility of using a single adjacent slide as reference standard, the averaged percentages were compared to the quantitative measures of the cross-section directly adjacent to the slides used for IHC in a univariate analysis.

The results of this comparison show that the averaged percentages of an entire case correlated significantly with the percentages obtained from a single adjacent slide for cancerous, benign tissue and stroma ($p < 0.001$ for all three analyses, Figure 35).

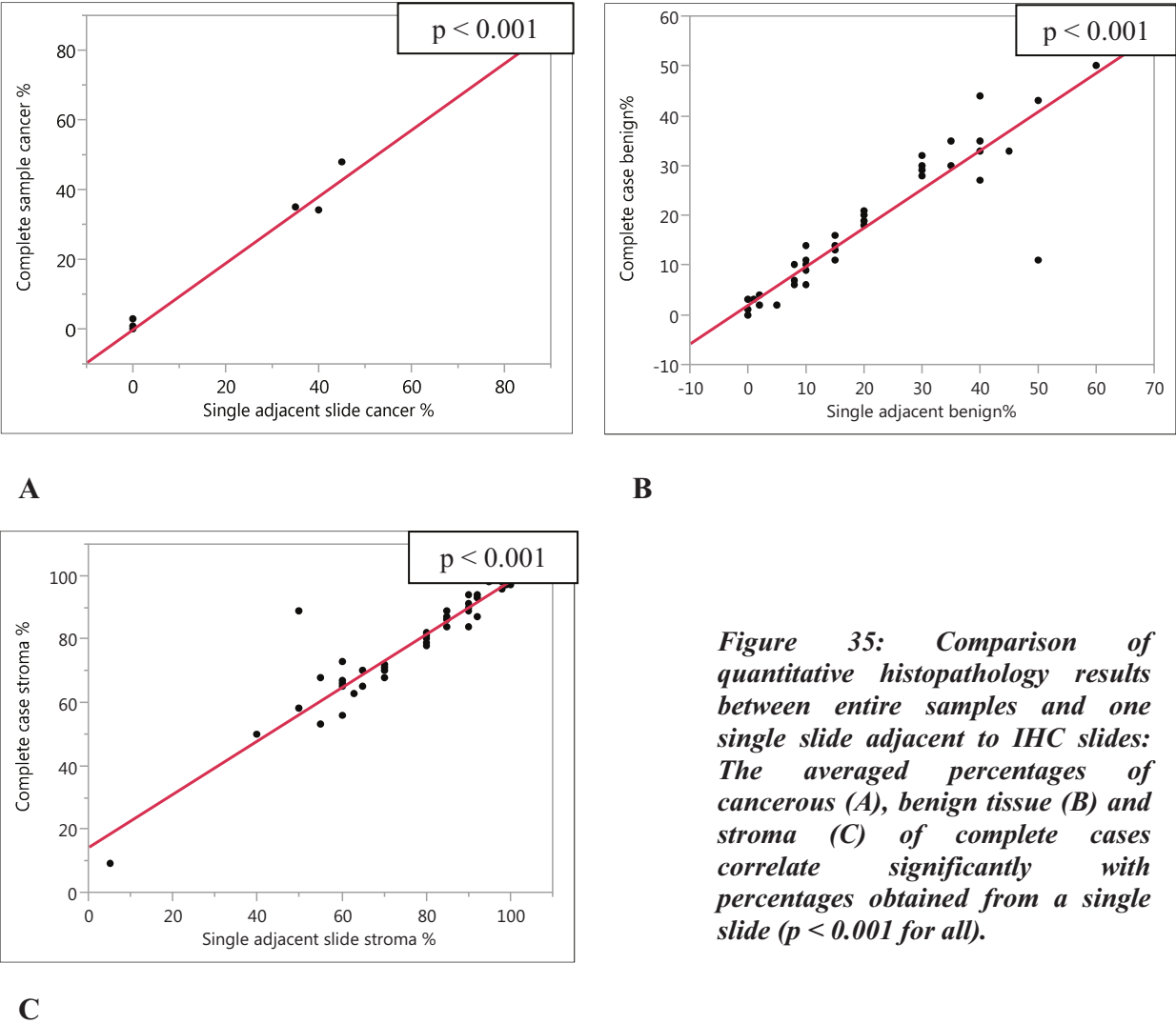


Figure 35: Comparison of quantitative histopathology results between entire samples and one single slide adjacent to IHC slides: The averaged percentages of cancerous (A), benign tissue (B) and stroma (C) of complete cases correlate significantly with percentages obtained from a single slide ($p < 0.001$ for all).

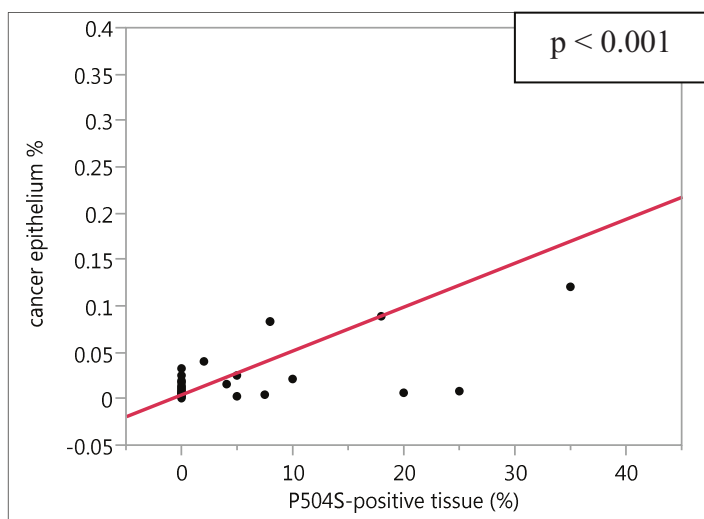
Table 10: Quantitative histopathology evaluation of complete samples and single adjacent slides

Sample #	Cancer %		Benign %		Stroma %	
	Complete	Single	Complete	Single	Complete	Single
1	0	0	9	10	91	90
2	80	85	11	10	9	5
3	0	0	44	40	56	60
4	1	0	21	20	78	80
5	0	0	30	35	70	65
6	0	0	27	40	73	60
7	48	45	0	0	53	55
8	0	0	14	15	86	85
9	0	0	33	45	68	55
10	0	0	14	15	86	85
11	0	0	2	5	99	95
12	0	0	13	15	87	85
13	0	0	35	40	65	60
14	0	0	18	20	82	80
15	35	35	2	2	63	63
16	0	0	0	0	100	100
17	0	0	6	8	94	92
18	3	0	14	10	84	90
19	0	0	3	0	97	100
20	0	0	35	35	65	65
21	0	0	1	0	100	100
22	0	0	2	5	98	95
23	0	0	2	2	98	98
24	0	0	43	50	58	50
25	0	0	11	50	89	50
26	0	0	35	35	65	65
27	0	0	43	50	58	50
28	0	0	16	15	84	85
29	0	0	29	30	71	70
30	0	0	2	2	98	98
31	0	0	10	10	90	90
32	0	0	6	10	94	90
33	0	0	11	10	89	90
34	0	0	4	2	96	98
35	0	0	50	60	50	40
36	0	0	32	30	68	70
37	0	0	21	20	79	80
38	0	0	20	20	80	80
39	0	0	7	8	93	92
40	0	0	10	10	90	90
41	0	0	16	15	84	85
42	0	0	28	30	72	70
43	0	0	33	40	67	60
44	0	0	16	15	84	85
45	0	0	19	20	81	80
46	0	0	10	8	87	92
47	0	0	30	30	70	70
48	0	0	11	15	89	85
49	0	0	0	0	100	100
50	0	0	3	1	97	99
51	34	40	0	0	66	60

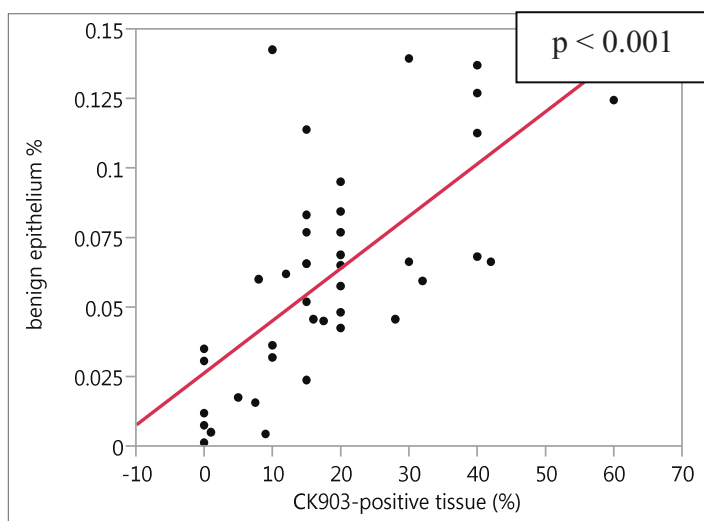
Furthermore, when comparing the results of the quantitative conventional histopathology analysis to the results obtained from the quantitative IHC slide review, the percentages of cancer determined by quantitative histopathology correlated significantly with the percentage of P504S- positive staining in the quantitative IHC slide review ($p < 0.001$). Similarly, the percentages of benign epithelium and stroma correlated between the quantitative histopathology and IHC readings (both $p < 0.001$).

In order to validate the quantitative IHC results obtained with QIAP, the percentages of cancer epithelium and benign epithelium measured with QIAP were correlated to the percentages of P504S- positive and CK903- positive tissue determined by the pathologist, as well as to the results of the quantitative analysis of conventional histopathology.

Cancer epithelium percentage (CaE%) as determined by QIAP showed a significant correlation to the percentage of P504S- positive tissue ($p < 0.001$) as well as to the percentage of cancer in the quantitative conventional histopathology analysis ($p = 0.001$). Similarly, the percentage of benign epithelium (BenE%) calculated by QIAP correlated significantly with the percentage of CK903- positive staining determined by quantitative IHC slide review ($p < 0.001$) and benign tissue percentage in quantitative conventional histopathology ($p = 0.0183$, Figure 36).



A



B

Figure 36:

Comparison between the results of quantitative IHC obtained from QIAP and determined by pathologic slide review: Cancer epithelium percentage by QIAP correlates significantly with the percentage of P504S- positive tissue (A); benign epithelium percentage by QIAP correlates significantly with CK903- positive tissue (B, $p < 0.001$).

6.6 Identification of Prostate Cancer Metabolomic Markers using QIAP

QIAP presents a valid and feasible approach to automatically and objectively determine quantitative IHC results, as demonstrated in 5.4. Furthermore, the use of an automated quantitative IHC analysis yields the advantage of time- efficient, high- throughput objective analysis of immunohistochemistry.

Therefore, in order to identify potential metabolomic markers for PCa, the relative spectral intensities obtained from ^1H HRMAS MRS were correlated to the results of quantitative IHC analysis with QIAP of the exact same tissue sample using a linear regression analysis.

Out of the 36 regions of interest (described in 4.2.3.), only two regions showed a significant correlation between the relative spectral intensities and CaE% as determined by QIAP.

The relative spectral intensities at 3.22 ppm correlated significantly with the CaE% results obtained by QIAP with a p-value of 0.015, identifying this region as metabolomic marker for PCa (Figure 37). The metabolite corresponding to this region is phosphocholine (PCho).

The second region for which a significant correlation of spectral intensities and CaE% was found, was the region 2.68 ppm (p = 0.0144). This region most closely corresponds to the metabolite citrate (Figure 38).

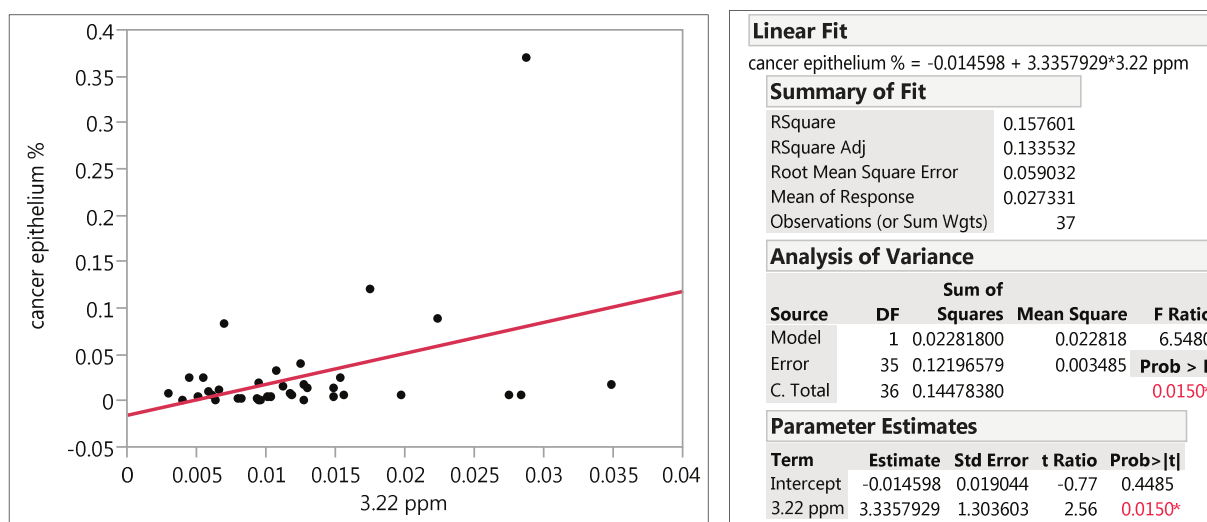


Figure 37: Significant correlation between relative spectral intensities and cancer epithelium percentage (CaE%) determined by quantitative IHC analysis using QIAP at the region 3.22 ppm.

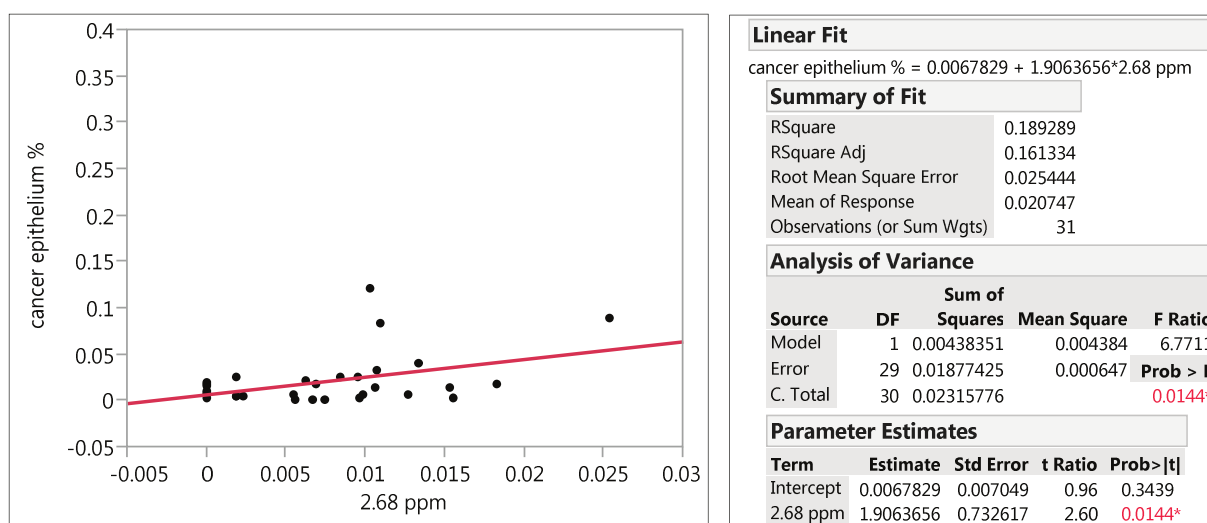


Figure 38: Significant correlation between relative spectral intensities and cancer epithelium percentage (CaE%) determined by quantitative IHC analysis using QIAP at the region 2.68 ppm.

The remaining 34 regions of interest did not show any correlation between spectral intensities and percentage of cancer epithelium. All graphs including the corresponding p- values for the correlation can be found in the Appendix section.

In particular, the spectral intensities at the metabolomic region for lactate (1.32 – 1.34 ppm, $p = 0.5334$) as well as for creatine / phosphocreatine (3.03 ppm, $p = 0.7427$) did not correlate significantly with the percentage of cancer epithelium. Similarly, no significant correlations could be found in other common metabolites in prostate cancer, such as the regions 3.75 ppm, representing glutamine ($p = 0.7545$), 3.74 ppm, representing glutamate ($p = 0.6097$), or 3.05- 3.09 ppm, the metabolomic region of spermine ($p = 0.6025$).

6.7 Patient Outcomes and Recurrence

The outcomes of the patients in our cohort were determined 5 years following the initial diagnosis and prostatectomy surgery. For four patients, no follow- up data was available. Two additional patients were followed for less than one year, considering them lost for follow- up. The remaining 45 patients were followed for an average time of 53.34 months (4.45 years), median follow- up 64.93 months (5.41 years), with a range between 14.53 and 78.43 months (1.21 and 6.54 years). During the follow- up time, 14 patients received adjuvant treatment: radiotherapy in 8 cases (16.67%), androgen-deprivation therapy in 5 cases (10.42%) and chemotherapy in 1 case (2.08%). Table 11 summarizes the outcome results.

Recurrence (PSA-elevation and / or new onset of clinical symptoms) was found in 11 patients (22.92%). However, the vast majority of patients (44, 97.78%) were alive at the time of last follow- up, with only one death found in the cohort. According to the classification of recurrence, 34 patients (75.56%) classified as recurrence category 1 (no recurrence), 7 patients (15.56%) belonged to the category 2 group (PSA-elevation without new clinical symptoms) and 4 patients (8.89%) were classified as category 4 (metastatic disease). No patients exhibited PSA-elevation and new onset of clinical symptoms (category 3, Figure 39).

Table 11: Outcome results

Follow-up (%)	
No follow-up	4 (7.84)
< 12 months follow-up	2 (3.92)
> 12 months follow-up	45 (88.24)
Adjuvant treatment (%)	
Radiotherapy	8 (17.78)
Androgen deprivation therapy	5 (11.11)
Chemotherapy	1 (2.22)
Recurrence (%)	11 (24.44)
Vital status at last follow up (%)	
Alive	44 (97.92)
Dead	1 (2.22)
Median follow-up in months (years)	64.93 (5.41)
Mean follow-up in months (years)	53.34 (4.45)
Follow-up time range (months)	14.53 – 78.43

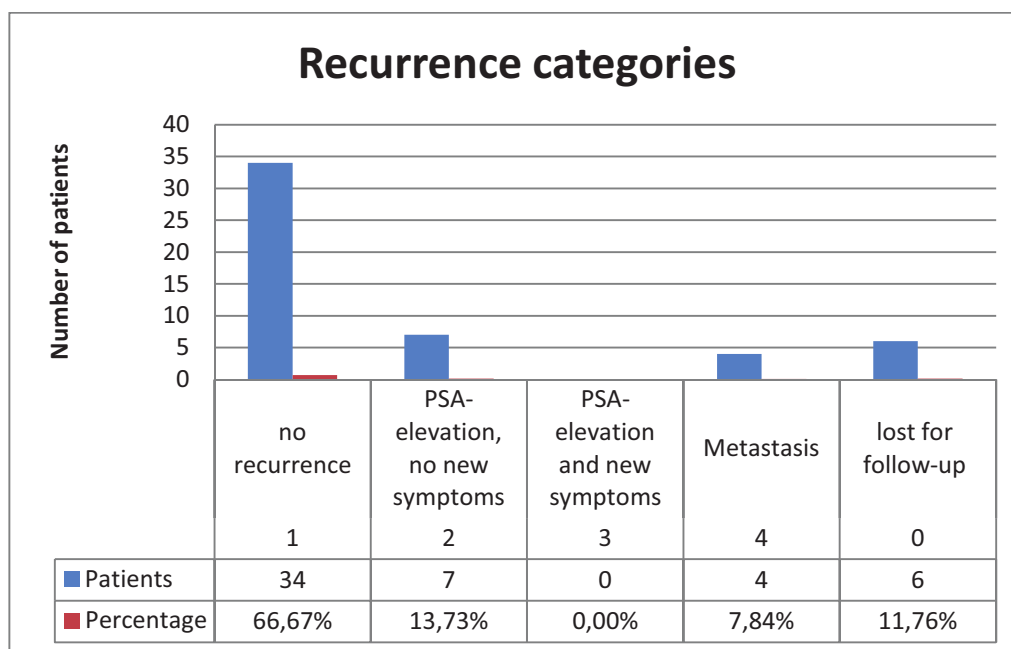
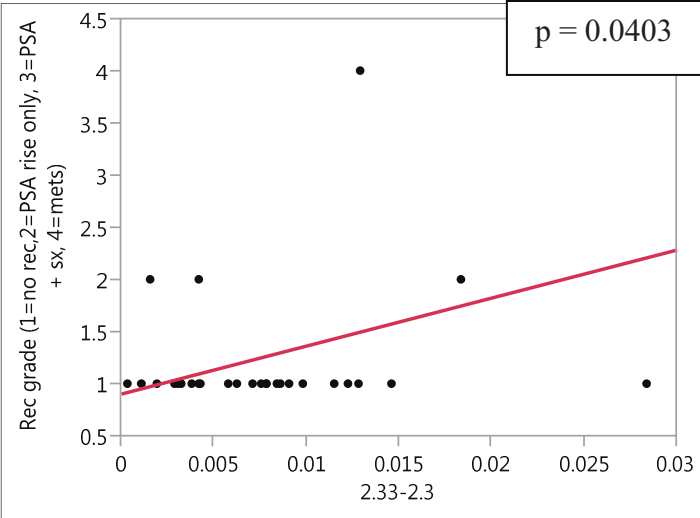


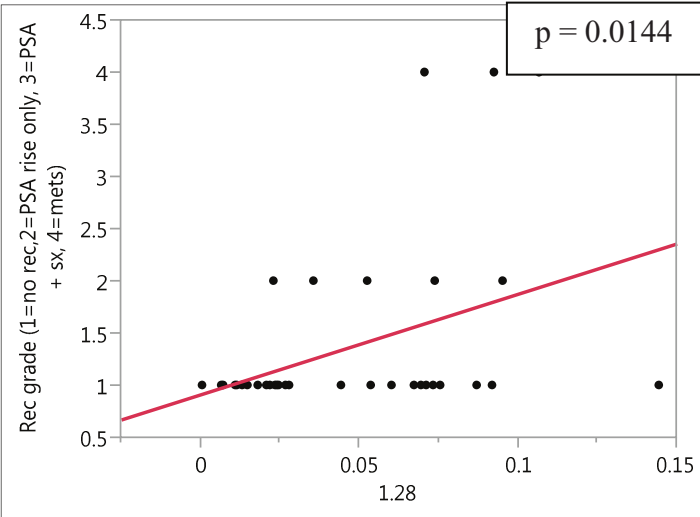
Figure 39: Recurrence categories and percentages

A correlation between the recurrence categories and the relative spectral intensities obtained with ¹H HRMAS MRS was performed in order to investigate for metabolomic markers of recurrence.

Two metabolomic regions showed a significant correlation between the recurrence category and the relative spectral intensities present: the region 2.33 – 2.3 ppm ($p = 0.0403$) and the region 1.28 ppm ($p = 0.0144$). The metabolites most closely corresponding to these metabolomic regions are phosphocreatine (2.33 – 2.3 ppm) and lipids (1.28 ppm, Figure 40).



A



B

Figure 40: Recurrence category correlates significantly with the relative spectral intensities at the regions 2.33 – 2.3 ppm (A, $p = 0.0403$) and 1.28 ppm ($p = 0.0144$), indicating that these regions might represent metabolomic markers of PCa recurrence.

7 Discussion

Summary of findings

In this study, a novel approach to identify metabolomic markers of prostate cancer was established, using prostate immunomarkers to quantify PCa metabolomic profiles measured from prostate tissue by ^1H HRMAS MRS.

In a first step, the potential of three prostate immunomarkers- P504S, CK903 and p63- to serve as tools for quantitative analysis of immunohistochemistry following ^1H HRMAS MRS was explored. This study aimed to verify that both quality and accessibility of the prostate immunomarkers used for the quantitative analysis were not impacted by prior ^1H HRMAS MR scanning, to ensure that these markers were suitable for post- spectroscopic IHC. For that, the quality and accessibility of immunostainings in prostate tissue samples that had undergone HRMAS ^1HMR spectroscopy were analyzed and compared to “unscanned” tissue sections from the same samples. In this investigation, the immunomarkers P504S and CK903 showed equally excellent immunostaining quality in both “scanned” and “unscanned” tissue samples, indicating that these markers are stable for immunohistochemical use following ^1H HRMAS MRS. The prostate immunomarker p63, however, showed significantly decreased quality of immunostaining after prior ^1H HRMAS MRS, suggesting that this marker might not be useful for IHC analysis after ^1H HRMAS MRS.

Using the ^1H HRMAS MRS- stable immunomarkers P504S and CK903, quantitative measures of the percentage of cancer present in the immunostained tissue sections were obtained, using the newly developed MATLAB-based quantitative image analysis program QIAP. The quantitative IHC results were validated, using quantitative measures of conventional histopathology and IHC judged by a pathologist.

The percentage of cancerous (CaE%) and benign epithelia (BenE%) measured by QIAP correlated significantly with the results for cancer and benign tissue in the conventional histopathology slide review ($p= 0.001$ and $p = 0.0183$, respectively). Furthermore, CaE% and BenE% correlated significantly with the quantitative evaluation of cancer and benign tissue percentages as determined by the pathologist ($p < 0.001$ for both), indicating that the results of quantitative IHC measurements obtained with the program QIAP are valid and valuable for quantitative IHC analysis.

Ultimately, in an attempt to validate the utility of quantitative IHC to identify metabolomic markers or PCa, relative spectral intensities obtained by ^1H HRMAS MR spectroscopy were

correlated to the quantitative measures of cancer epithelium determined from immunostained slides of the same prostate sample, using QIAP.

Out of 36 regions investigated, two regions showed a statistically significant correlation between quantitative IHC results and spectral intensities: 3.22 ppm ($p = 0.0150$) and 2.68 ppm ($p = 0.0144$). The metabolites corresponding to these regions, phosphocholine (PCho, 3.22 ppm) and citrate (2.68 ppm) therefore have the potential to serve as metabolomic markers of cancerous epithelium in prostate tissue.

Furthermore, patient outcomes five years after their initial surgery were obtained and PCa recurrence categories were identified in our cohort. Using the newly established quantitative IHC approach to identify metabolomic markers, metabolomic markers of recurrence could be identified in this study. Two metabolomic regions presented a significant correlation between recurrence grade and the relative spectral intensities: the region 2.33 – 2.3 ppm ($p = 0.0403$) and the region 1.28 ppm ($p = 0.0144$). The metabolites most closely corresponding to these metabolomic regions are phosphocreatine (2.33 – 2.3 ppm) and lipids (1.28 ppm). These results suggest that these metabolites could represent metabolomic markers of recurrence in PCa patients.

Interpretation of the results

The comparison of the quality and evaluability of immunostainings following ^1H HRMAS MRS with those of “unscanned” tissue sections from the same prostate samples supports the hypothesis that the prostate tissue architecture remains intact during an ^1H HRMAS MRS experiment. Multiple previous studies have established this knowledge [16, 37].

The equally excellent staining qualities in the stainings with the immunomarkers P504S and CK903 indicate that the immunologic potential is indeed preserved during a scan. These findings suggest that both markers, P504S and CK903, are stable for immunohistochemical use on prostate tissue samples previously studied by ^1H HRMAS MRS.

In contrast, the quality and evaluability of the immunostainings with p63 were significantly decreased following ^1H HRMAS MRS, indicating that this immunomarker might be susceptible to damage induced during the process of ^1H HRMAS MRS scanning or post-processing, or might lose its immunologic potential during the spectroscopy experiment. As the quality and the diagnostic value of p63-immunostainings appear to be altered through spectroscopy procedures, this immunomarker seems to be unuseful for IHC following ^1H HRMAS MRS. The results of this study indicate that, although the tissue architecture remains stable after ^1H HRMAS MRS, not all immunohistochemical procedures are feasible following

spectroscopic procedures. Prior to analyzing tissue scanned samples with IHC, the proposed immunomarker should therefore be tested for stability during the spectroscopic analysis.

Ultimately, the quantitative analysis of combined immunostainings with P504S and CK903 on adjacent tissue cross- sections presents a suitable diagnostic approach to quantitatively evaluate prostate tissue pathologic conditions and distinguish between benign and cancerous conditions in prostate tissue. While P504S indicates the presence of cancerous tissue, CK903 identifies benign glands. Thus, the combination of these complementary antibodies highly increases the diagnostic value of the prostate cancer immunostaining.

The significant correlations between the results of quantitative IHC analysis using the evaluation program QIAP and the results of a quantitative IHC review by an experienced pathologist strongly confirm that the program QIAP presents a valuable and valid method to determine quantitative measures of IHC. The fact that the results of QIAP also correlate significantly with the results of a quantitative conventional histopathology analysis further validates the utility of QIAP for quantitative pathological analysis. These findings show that QIAP presents a valid, objective and computer-automated approach for quantitative IHC analysis.

Using quantitative IHC analysis and metabolomic profiles obtained with ^1H HRMAS MRS, two metabolomic regions that significantly correlated with quantitative measures of cancerous epithelium in the samples were identified. The two metabolites corresponding to these regions, PCho and citrate, therefore could be identified as metabolomic markers of prostate cancer conditions in our cohort. PCho is a ubiquitous metabolite, mostly present in cell membranes, and involved in the pathway of choline synthesis. PCa causes high cell proliferation and an increase in cell membrane synthesis, which results in elevated choline levels and an elevation of choline synthesis meta-products, like PCho, glycerophosphocholine and free choline [93]. Although PCho is an unspecific metabolite, its increased concentration in cancerous conditions might contribute to its potential as a metabolomic marker of PCa.

Citrate is a metabolite highly characteristic of healthy prostate tissue and prostate fluids. Under normal conditions, high levels of citrate are generally found. Malignant conditions, such as PCa, cause a pathological oxidation of citrate in the KREBS cycle, resulting in a significant decrease of citrate levels. A decrease in the citrate signals as well as in the citrate/creatine- and (choline + creatine)/citrate- ratios in prostate spectroscopy are commonly acknowledged indicators of the presence of cancer. The identification of citrate as a metabolomic marker of PCa seems therefore plausible. A quantification of citrate seems to be

a feasible approach and could potentially increase the diagnostic value of prostate spectroscopy.

Comparison of the results with findings of other studies

Multiple previous studies have focused on creating metabolomic profiles for PCa, using NMR spectroscopy [61, 94] and mass spectrometry methods [67, 95]. However, due to technical challenges in this field, previous results are highly diverse and different metabolites have been proposed as potential biomarkers for PCa [36, 96-98].

The association between changes in choline-containing metabolites and malignant transformation is well established [99]. Increased expression of genes involved in choline metabolism and transport, such as choline kinase, kinase have been found in different cancers, including breast cancer or high- grade gliomas [100, 101], but also PCa. Choline and choline compounds have been shown to be increased in prostatectomy as well as prostate biopsy specimen in cancer patients versus matched benign tissue samples [60, 68]. Also, previous *ex vivo* studies have found increased Pcho levels to be associated with increased PSA and higher GLEASON score, indicating the importance of this biomarker for the detection and classification of prostate cancer [50, 60]. PCho is a metabolite involved in the pathway of choline synthesis. Because of its association to alterations in cell membrane synthesis, choline levels are increased in PCa, resulting in an elevation of choline synthesis meta-products, like PCho, glycerophosphocholine and free choline [93]. Not only increased cell proliferation, but also changes in tumor microenvironment, like hypoxia or shifts of pH, account for alterations in choline metabolite levels as well as other malignant malformations [102]. Further evaluation is needed for this potential biomarker.

Other metabolites have been suggested to present biomarkers of PCa in past studies. Lactate and alanine are known to be increased in PCa, due to enhanced glycolytic activity and the Warburg effect [61, 68]. However, these biomarkers are unspecific metabolites which are altered in multiple cancer types, thereby reducing their potential to be PCa specific biomarkers. With p- values of 0.5334 (region 1.32 – 1.34 ppm) and 0.7828 (region 1.46 ppm) respectively, the spectroscopic regions corresponding to lactate and alanine did not show significant correlations to CaE% in the present study. With the established dataset, it was not possible to identify these metabolites as biomarkers for PCa.

In contrast to the unspecific metabolites mentioned before, decreased levels of citrate, zinc and spermine are associated more specifically with prostate cancer [103].

Decreased levels of citrate have previously been observed in prostate cancer tissue by *ex vivo* MRS [68] and measurements of citrate signals and metabolite ratios including citrate have successfully been incorporated into routine clinical diagnostics [104, 105]. In accordance with the results of this study, citrate has been suggested to present a PCa biomarker in a previous study using *ex vivo*¹H HRMAS MRS [50]. In a recent study, citrate was additionally found to be associated with cancer aggressiveness. The authors reported a negative correlation between citrate levels and the GLEASON score as well as significant differences between low grade and high grade PCa, indicating that citrate concentrations measured by MRS have the potential to distinguish between highly aggressive and indolent PCa cases [106].

Besides changes in citrate levels, a decrease of polyamine signals has been found to be associated with PCa [50]. Significantly lower concentrations of spermine have been reported in high grade compared to low grade PCa, suggesting spermine to be a discriminative biomarker for PCa aggressiveness [106]. Polyamines, especially spermine, have a strong potential for incorporation into clinical practice. In the present study, an association between cancer epithelium percentage and spectral intensities for the region of spermine (3.05 – 3.09 ppm, $p = 0.6025$) could not be confirmed.

Other metabolomic biomarkers described in the literature include myo-inositol, taurine, valine-leucine, glutamine and hydroxybutyrate [63]. None of these metabolites could be identified using the presented novel approach, most likely due to the predominantly benign nature of the sample set. A recent study using LC/ GC-MS to identify PCa metabolomic markers, found six metabolites that were associated with PCa and its progression: sarcosine, uracil, kynurenine, glycerol-3-phosphate, leucine and proline [67]. Among them, sarcosine demonstrated the most pronounced differences, suggesting its strong potential as a biomarker for PCa and leading to further extensive investigations of this metabolite [107-109]. In the present study, none of these recently suggested metabolomic biomarkers could be confirmed to be associated with PCa when using quantitative IHC as investigative tool. Multiple reasons and limitations of our approach might account for that, which will be illustrated in the following section.

Limitations of the study

Limitations of this study are due in part to the heterogenous sample cohort with predominantly benign tissues. Out of each prostatectomy sample, only a small amount of tissue was studied, therefore not guaranteeing definitive evaluation of the cancerous portion. Also, the sample cohort contained preliminary stages of malignant conditions, such as BPH or

PIN. Because of this, a clear evaluation of metabolite markers for cancer was difficult to realize. In order to establish validate prostate cancer metabolomics profiles, more cases with predominantly cancerous conditions would need to be studied.

Due to difficulties in spectroscopy or quantitative image evaluation, only 42 out of the 51 cases could be subjected to quantitative analysis, substantially reducing the sample cohort.

The MATLAB-based evaluation program used for the quantitative image evaluation is a self-developed pioneer image evaluation program. Therefore, the results of this method have to be considered with caution. Further improvements of the program are necessary in the future. For instance, image brightness should be adjusted and a fixed, and a user- independent threshold for each immunomarker employed. To ensure program improvement, bigger sample sizes need to be evaluated using this device. First and foremost, the current results should be validated using a larger sample cohort of predominantly cancerous tissue. Also, a cumulative analysis of the tissue samples, including all cross- sections of each individual sample, would be useful. Ultimately, a 3- dimensional sample analysis seems to be desirable, as it allows full analysis of all tissue components.

This study was performed *ex vivo*, using a 600MHz MR spectrometer. Translation of the results into an *in vivo* clinical application is challenging. Routine clinical scanners usually have field strengths of 3T or 1.5T, and thus provide a lower spectral resolution and more prominent baseline noise than high field spectrometers. 7T *in vivo* scanners provide more accurate results and could help overcoming these challenges, but are not available for routine clinical diagnostics in most centers. To date, the strongest MR scanner available for *in vivo* use in human subjects has a field strength of 10.5T and is located at the University of Minnesota in Duluth, MN, USA [110].The NeuroSpin facility in France is currently constructing an 11.7T whole- body human scanner which is expected to be available for research purposes in 2014 [111]. Due to artifacts and side effects experienced by the subjects, the use of even stronger magnets will not be possible in the near future, thus impairing a direct translation of the 14.1T spectroscopy results established in this study into an *in vivo* application. Besides, spectroscopy is more time- consuming, more difficult to evaluate and more expensive than other methods.

Magic Angle Spinning, the central method used in this study, is a highly optimized technique which enables an extremely high resolution in an *ex vivo* setting. However, MAS can never be performed in humans, as a human body would not be able to tolerate spinning in a scanner. Therefore, the extremely high resolution achieved in with a MAS- rotor will never be reproducible in an *in vivo* application.

Ultimately, in order to establish clinical applicability of our results, metabolomic profiles established by *ex vivo* ^1H HRMAS MRS would have to be translated into an *in vivo* setting, while at the same time increasing the quality of low field spectroscopy and reducing scan time and costs.

As part of our investigations, patient outcomes were determined 5 years after prostatectomy. Early identified and correctly treated prostate cancer has a very favorable prognosis, with a 5-year-survival time of close to 100% [112]. Therefore, at the time of last follow-up, the vast majority of patients in our cohort were still alive, limiting the conclusions that could be drawn from correlations of spectroscopy and outcome measures.

Strengths

Despite those limitations, the presented approach using quantitative evaluation of IHC clearly yields great potential for clinical applicability. In contrast to conventional histopathology using H&E staining, IHC is an objective, observer- independent method and has the potential to be computer- automated. Through visualization of immunohistochemical reactions with DAB, subsequent quantitative, in contrast to qualitative, evaluation is possible, as shown by this study. Using this approach, high- throughput evaluation of large cohorts of immunostained prostate tissue samples could be possible, realizing the establishment of valid and accurate metabolomic profiles that could then be used in a clinical setting. These metabolomic profiles could aid in accurate differentiation between benign and malignant conditions, as well as between low and high grade cancer. Ultimately, objective and extremely fast evaluation of prostatectomy- specimen or biopsies could be feasible in the future, without the need for an independent pathologist. A translation of metabolomics profiles established with our method into an *in vivo* setting is possible, and could present a non- invasive diagnostic approach for accurate classification of disease, even in a pre-operative setting. Longitudinal, non-invasive monitoring of PCa patients would be possible, and recurrent disease could be better distinguished from other non- malignant conditions.

In this study, the patient outcome and recurrence categories were determined and correlated in order to identify metabolomic markers of recurrence. The vast majority of patients (88.24%) were followed tightly for the entire time- period of 5 years, adding great additional value to the results of spectroscopy and IHC.

Outlook

Given the exploratory nature of the study, the presented findings must be considered in a hypothesis generating context. Further studies are needed to verify the identified prostate cancer metabolomic markers phosphocholine and citrate, as well as to establish the clinical applicability of this novel method. A high- throughput analysis of a large cohort of PCa samples (e.g. biopsies or prostatectomy samples) with this novel approach could aid in the development of accurate metabolomics profiles to differentiate several conditions, such as highly aggressive cancer from indolent cases or precursor lesions. Even an objective, accurate staging could be accomplished, by differentiating biopsy samples or prostatectomy samples according to metabolomics profiles of different GLEASON grades. A future aim should be a translation of metabolomic profiles of PCa into an *in vivo* setting. Ultimately, a non-invasive approach to longitudinally monitor disease status and help to identify recurrence in PCa patients would be of great clinical importance.

The patients enrolled in this study were followed for 5 years after initial surgery to determine outcome and recurrence. A prospective patient follow- up for an even longer time (10 years or more) could add additional knowledge to and determine more accurate measures of outcome and survival. In order to improve PCa metabolomics profiles and confirm previous results of metabolomic predictors of aggressive behavior, these outcomes could be correlated with ^1H HRMAS MRS results as well as quantitative pathology using IHC in future studies.

Conclusion

In this study, a novel method was introduced that allows for an observer- independent, quantitative analysis of IHC to help establish metabolomic profiles and identify metabolomic markers of PCa from spectral intensities obtained with ^1H HRMAS MRS. The combination of ^1H HRMAS MRS and IHC has the potential to serve as faster, more accurate, observer-independent diagnostic tool. ^1H HRMAS MRS could become a useful tool in the diagnostics of PCa. Biopsies of patients that are suspected of having PCa could be subjected to ^1H HRMAS MRS and the results compared to pre-established cancer profiles. Thus, a differentiation between highly malignant and aggressive conditions that requires radical therapy or rather low malignant, non-aggressive tumors that can be treated with “watchful waiting”, would be possible. A prospective *in vivo* application of PCa metabolite profiles and metabolomic markers could serve as highly sensitive, non- invasive diagnostic tool.

Observer- independent, computer- automated tissue evaluation could help to avoid overtreatment and reduce complications and risks from invasive methods for PCa patients in the future.

8 Summary / Abstract

Background

Prostate cancer (PCa) is the most frequently diagnosed malignant disease among adult males in the USA and the second leading cause of cancer deaths in men. Due to the lack of diagnostic tools that are able to differentiate highly malignant and aggressive cases from indolent tumors, overtreatment has become very common in the era of prostate specific antigen (PSA) screening. New diagnostic methods to determine biological status, malignancy, aggressiveness and extent of PCA are urgently needed. ^1H High Resolution Magic Angle Spinning Nuclear Magnetic Resonance Spectroscopy (^1H HRMAS MRS) can be used to establish PCa metabolomic profiles while preserving tissue architecture for subsequent histopathological analysis. Immunohistochemistry (IHC), as opposed to conventional histopathology methods, has the potential to provide objective, more accurate and quantitative knowledge of tissue pathology. This diagnostic- accuracy study sought to evaluate a novel approach to quantitatively identify metabolomic markers of PCa by exploring the potential of PCa immunomarkers to quantify metabolomic profiles established by ^1H HRMAS MRS.

Material and Methods

^1H HRMAS MRS was performed on tissue samples of 51 prostate cancer patients using a 14.1 T BRUKER NMR spectrometer with a rotor synchronized CPMG pulse sequence. Spectral intensities of 36 regions of interest were measured as integrals of curve fittings with Lorentzian-Gaussian line shapes. Immunohistochemistry (IHC) was carried out following the spectroscopy scan, using three prostate immunomarkers to identify cancerous and benign glands: P504S (Alpha-methylacyl-CoA-racemase), CK903 (high-molecular weight cytokeratin) and p63. The immunostaining quality following ^1H HRMAS MRS was evaluated and compared to unscanned sections of the same sample, to verify the stability and accessibility of the proposed immunomarkers. IHC images were automatically and quantitatively evaluated, using a quantitative image analysis program (QIAP), to determine the percentage of cancerous and benign epithelia in the cross- sections. The results of the program were validated by a correlation to the results of a quantitative IHC review and quantitative conventional histopathology analysis performed by an experienced pathologist.

Ultimately, spectral intensities and the cancer epithelium percentage, obtained from quantitative immunohistochemistry, were correlated in order to validate PCa metabolomics markers identified by ^1H HRMAS MRS.

Patient outcomes and incidence of recurrence were determined by retrospective review of medical records five years after initial surgery. States of recurrence were correlated to spectral intensities to explore potential metabolomics markers of recurrence in the cohort.

Results

Immunostainings with P504S and CK903 showed excellent staining quality and accessibility following ^1H HRMAS MRS, making these markers suitable for our novel quantitative approach to determine metabolomics profiles of PCa. In contrast, the quality of p63 IHC was impaired after previously performed spectroscopy.

IHC using the immunomarkers P504S and CK903 on adjacent slides presents a feasible quantitative diagnostic method to distinguish between benign and cancerous conditions in prostate tissue. The cancer epithelium percentage as determined by QIAP showed a significant correlation to the results of quantitative IHC analysis performed by a pathologist ($p < 0.001$), as well as to a quantitative conventional histopathology review ($p = 0.001$). The same was true for the benign epithelium percentage ($p < 0.001$ and $p = 0.0183$), validating our novel approach.

Two metabolomic regions showed a significant correlation between relative spectral intensities and the cancer epithelium percentage as determined by QIAP: 3.22 ppm ($p = 0.015$) and 2.68 ppm ($p = 0.0144$). The metabolites corresponding to these regions, phosphocholine and citrate, could be identified as metabolomic markers of PCa in our cohort. 45 patients were followed for more than 12 months. Of these, 97.8% were still alive five years after initial surgery. 11 patients (24.4%) experienced a recurrence during the follow-up time. The categories of recurrence showed a correlation to the spectral intensities of two regions, 2.33 – 2.3 ppm ($p = 0.0403$) and 1.28 ppm ($p = 0.0144$), corresponding to the metabolites phosphocreatine and lipids.

Conclusion

This study introduces a method that allows an observer-independent, quantitative analysis of IHC to help establish metabolomic profiles and identify metabolomic markers of PCa from spectral intensities obtained with ^1H HRMAS NMR Spectroscopy. The immunomarkers P504S and CK903 have been found suitable IHC analysis following ^1H HRMAS MRS. A

prospective *in vivo* application of PCa metabolite profiles and metabolomic markers determined by our analysis could serve as highly sensitive, non-invasive diagnostic tool. This observer-independent, computer-automated, quantitative analysis could help to distinguish highly aggressive tumors from low-malignant conditions, avoid overtreatment and reduce risks and complications for cancer patients in the future. However, further studies are needed to verify the identified PCa metabolomic markers and to establish clinical applicability.

9 Zusammenfassung

Einführung

Prostatakrebs ist eine häufigsten Krebserkrankungen in den USA und die zweithäufigste malignom- assoziierte Todesursache männlicher Patienten weltweit. Seit der Einführung des Prostata- spezifischen Antigen (PSA)- Screeningtests wird diese Krebsart in früheren Stadien diagnostiziert und therapiert, wodurch die Mortalitätsrate in den letzten Jahren deutlich reduziert werden konnte. Da moderne diagnostische Methoden bislang jedoch nicht ausreichend in der Lage sind, suffizient zwischen hochmalignen und weniger aggressiven Varianten dieses bösartigen Krebsleidens zu unterscheiden, werden häufig auch Patienten aggressiv therapiert, deren niedriggradiges Prostatakarzinom keine klinische Relevanz gehabt hätte. Es besteht daher ein großes wissenschaftliches Interesse an der Entwicklung neuer diagnostischer Methoden zur akkuraten Bestimmung von biologischem Status, Malignität, Aggressivität und Ausmaß einer Prostatakrebserkrankung.

"¹H High Resolution Magic Angle Spinning Nuclear Magnetic Resonance Spectroscopy" (¹H HRMAS MRS) ist eine vielversprechende diagnostische Methode, welche es ermöglicht, metabolomische Profile von Prostatakrebs zu erstellen, ohne die Gewebsstruktur der analysierten Proben zu zerstören. Durch anschließende histopathologische Begutachtung lassen sich die erstellten Metabolitprofile validieren und evaluieren.

Im Gegensatz zu konventionellen histopathologischen Methoden können durch immunhistochemische Verfahren dabei objektivere, akkuratere und quantifizierbare histopathologische Erkenntnisse gewonnen werden.

Die vorliegende Studie präsentiert einen neuentwickelten diagnostischen Ansatz zur quantitativen Bestimmung von metabolomischen Markern von Prostatakrebs, basierend auf der Durchführung von ¹H HRMAS NMR Spektroskopie und quantitativer Immunhistochemie.

Material und Methoden

Einundfünfzig Gewebeproben von Prostatakrebspatienten wurden mittels ¹H HRMAS MRS an einem 14.1 T BRUKER NMR Spektrometer unter Einsatz einer CPMG-Pulssequenz untersucht. Spektrale Intensitäten in 36 Metabolitregionen wurden gemessen. Anschließend wurden die analysierten Gewebeproben mit drei Immunfärbemarkern für sowohl malignes (P504S, Alpha-methylacyl-CoA-racemase) als auch benignes (CK903, High-molecular weight cytokeratin, und p63) Prostatagewebe angefärbt und quantitativ mit Hilfe eines

Bildanalyseprogramms (QIAP) ausgewertet. Die Anwendbarkeit und Auswertbarkeit der genannten Immunomarker nach Spektroskopie wurde evaluiert und mit der Färbungsqualität von nicht-gescannten Schnitten verglichen.

Die Resultate der automatischen Auswertung durch QIAP konnten durch einen erfahrenen Pathologen in einer quantitativen Analyse der Immunfärbungen sowie konventioneller histologischer Färbungen derselben Gewebeproben validiert werden. Die spektralen Intensitäten aus den Messungen mit ^1H HRMAS MRS wurden mit den korrespondierenden Ergebnissen der quantitativen Auswertung der Immunfärbungen korreliert, um metabolische Marker von Prostatakrebs zu identifizieren.

Der klinische Verlauf und die Rezidivrate der Patienten wurden 5 Jahre nach der initialen Prostatektomie retrospektiv bestimmt. Rezidivkategorien wurden erstellt und mit den bestimmten spektralen Intensitäten korreliert, um metabolische Marker für das Auftreten von Prostatakrebsrezidiven zu identifizieren.

Ergebnisse

Die Immunfärbungen mit P504S und CK903 zeigten exzellente Qualität und Auswertbarkeit nach vorheriger ^1H HRMAS MRS. Beide Marker eigneten sich zur Durchführung von quantitativer Immunhistochemie an spektroskopierten Gewebeproben. Im Gegensatz dazu war die Qualität der Immunfärbungen mit p63 nach Spektroskopie vermindert. Quantitative Immunfärbungen unter Einsatz der Immunmarker P504S und CK903 stellten eine praktikable diagnostische Methode dar, um zwischen malignen und benignem Prostatagewebe zu unterscheiden.

Der Anteil von bösartig verändertem Prostatagewebe, bestimmt durch QIAP, korrelierte signifikant mit den Ergebnissen der quantitativen Analyse der Immunfärbungen durch den Pathologen ($p < 0.001$), sowie mit der quantitativen Auswertung der konventionellen histopathologischen Färbung ($p = 0.001$). Ebenso ließ sich die Bestimmung des Anteils von benignem Gewebe mit QIAP zu den Ergebnissen der pathologischen Analyse korrelieren ($p < 0.001$ und $p = 0.0183$).

Für zwei metabolische Regionen konnte eine signifikante Korrelation zwischen relativen spektralen Intensitäten, bestimmt mit ^1H HRMAS NMR Spektroskopie, und dem Anteil von malignem Epithelium in derselben Gewebeprobe, ermittelt durch QIAP, festgestellt werden: 3.22 ppm ($p = 0.015$) und 2.68 ppm ($p = 0.0144$). Die zu diesen Regionen korrespondierenden Metaboliten, Phosphocholin und Zitrat, konnten als potentielle metabolische Marker für Prostatakrebs identifiziert werden.

Die retrospektiven Analyse der klinischen Daten der Patienten fünf Jahre nach Prostatektomie ergab eine Überlebensrate von 97.8%. Elf dieser Patienten (24.4%) erlitten ein Rezidiv ihrer Erkrankung. Die bestimmten Rezidivkategorien korrelierten signifikant mit zwei metabolomischen Regionen (2.33 – 2.3 ppm, $p = 0.0403$ und 1.28 ppm, $p = 0.0144$), welche zu den Metaboliten Phosphokreatin und Lipiden korrespondierten.

Schlussfolgerung

Die vorliegende Studie präsentiert einen diagnostischen Ansatz zur objektiven und quantitativen Bestimmung metabolomischer Marker von Prostatakrebs unter Verwendung von ^1H HRMAS MRS und Immunhistochemie.

P504S und CK903 eignen sich als Immunmarker für quantitative Immunfärbungen nach vorheriger Durchführung von ^1H HRMAS MRS.

Die Metaboliten Phosphocholin und Ziträt konnten in der vorliegenden Patientenkohorte als potentielle metabolomische Marker für Prostatakrebs identifiziert werden.

Eine mögliche *in vivo* Anwendung der gefundenen metabolomischen Marker könnte als hochsensitives, objektives und nicht-invasives diagnostisches Werkzeug der Prostatakrebsdiagnostik dienen. Der vorliegende untersucherunabhängige, automatisierte und quantitative diagnostischer Ansatz hat das Potential, zwischen hochmalignen und weniger aggressiven Krebsfällen zu unterscheiden und somit unnötige Risiken und Komplikationen für Prostatakrebspatienten zu reduzieren.

Weitere Untersuchungen sind notwendig, um die identifizierten metabolomischen Marker zu verifizieren und eine klinische Anwendung zu etablieren.

10 References

1. Jemal, A., et al., *Global cancer statistics*. CA Cancer J Clin, 2011. 61(2): p. 69-90.
2. Cancer, I.A.f.R.o., *Facts Sheets Cancer*. 2014(http://globocan.iarc.fr/Pages/fact_sheets_cancer.aspx).
3. Nelson, W.G., A.M. De Marzo, and W.B. Isaacs, *Prostate cancer*. N Engl J Med, 2003. 349(4): p. 366-81.
4. Carroll, P.R., Lee, K., Fuks, Z., Kantoff, P., *Cancer of the Prostate*. , in *Cancer: Principle and Practise of Oncology*., V. DeVita, Hellman, S., Rosenberg, S., Editor. 2001, Lippincott Williams & Wilkins: Philadelphia.
5. Roodman, G.D., *Mechanisms of bone metastasis*. N Engl J Med, 2004. 350(16): p. 1655-64.
6. McNeal, J.E., *Prostatic microcarcinomas in relation to cancer origin and the evolution to clinical cancer*. Cancer, 1993. 71(3 Suppl): p. 984-91.
7. Siegel, R., D. Naishadham, and A. Jemal, *Cancer statistics, 2013*. CA Cancer J Clin, 2013. 63(1): p. 11-30.
8. Steiner, H., et al., *Clinical and pathologic features of prostate cancer detected after repeat false-negative biopsy in a screening population*. Prostate, 2004. 58(3): p. 277-82.
9. Welch, H.G. and P.C. Albertsen, *Prostate cancer diagnosis and treatment after the introduction of prostate-specific antigen screening: 1986-2005*. J Natl Cancer Inst, 2009. 101(19): p. 1325-9.
10. DeVita, V., Hellman, S., Rosenberg, S., *Cancer: Principles and Practise of Oncology*. 7th ed. 2005, Philadelphia: Lippincott Williams & Wilkins.
11. Draisma, G., et al., *Lead time and overdiagnosis in prostate-specific antigen screening: importance of methods and context*. J Natl Cancer Inst, 2009. 101(6): p. 374-83.
12. Pound, C.R., et al., *Natural history of progression after PSA elevation following radical prostatectomy*. JAMA, 1999. 281(17): p. 1591-7.
13. Shibata, A., J. Ma, and A.S. Whittemore, *Prostate cancer incidence and mortality in the United States and the United Kingdom*. J Natl Cancer Inst, 1998. 90(16): p. 1230-1.
14. Bangma, C.H., S. Roemeling, and F.H. Schroder, *Overdiagnosis and overtreatment of early detected prostate cancer*. World J Urol, 2007. 25(1): p. 3-9.
15. Schroder, F.H., *PSA screening--a review of recent studies*. Eur J Cancer, 2009. 45 Suppl 1: p. 402-4.
16. Burns, M.A., et al., *Quantitative pathology in tissue MR spectroscopy based human prostate metabolomics*. Technol Cancer Res Treat, 2004. 3(6): p. 591-8.
17. Prostata-Center, *Treatment of Prostate Cancer: Precise and Safe*. 2014(http://www.prostate-center.org/Prostate_Cancer_Treatment/3D-Biopsy.htm).

18. Coakley, F.V., et al., *Prostate cancer tumor volume: measurement with endorectal MR and MR spectroscopic imaging*. Radiology, 2002. 223(1): p. 91-7.
19. Akin, O. and H. Hricak, *Imaging of prostate cancer*. Radiol Clin North Am, 2007. 45(1): p. 207-22.
20. Mazaheri, Y., et al., *Prostate cancer: identification with combined diffusion-weighted MR imaging and 3D 1H MR spectroscopic imaging--correlation with pathologic findings*. Radiology, 2008. 246(2): p. 480-8.
21. Jordan, K.W. and L.L. Cheng, *NMR-based metabolomics approach to target biomarkers for human prostate cancer*. Expert Rev Proteomics, 2007. 4(3): p. 389-400.
22. A., A., *Diagnosis of cancer of the prostate: biopsy by rectal route*. The Urologic and Cutaneous Review, 1937. 41(421).
23. Djavan, B., et al., *Prospective evaluation of prostate cancer detected on biopsies 1, 2, 3 and 4: when should we stop?* J Urol, 2001. 166(5): p. 1679-83.
24. Roehl, K.A., J.A. Antenor, and W.J. Catalona, *Serial biopsy results in prostate cancer screening study*. J Urol, 2002. 167(6): p. 2435-9.
25. Gleason, D.F., *Classification of prostatic carcinomas*. Cancer Chemother Rep, 1966. 50(3): p. 125-8.
26. Humphrey, P.A., *Gleason grading and prognostic factors in carcinoma of the prostate*. Mod Pathol, 2004. 17(3): p. 292-306.
27. Delahunt, B., et al., *Gleason grading: past, present and future*. Histopathology, 2012. 60(1): p. 75-86.
28. Wikipedia, *Gleason score*. 2014(<http://en.wikipedia.org/wiki/File:Gleasonscore.jpg>).
29. Prevention, C.f.D.C.a., *National Hospital Discharge Survey 2010*. 2009 (http://www.cdc.gov/nchs/data/nhds/4procedures/2009pro4_numbrerate.pdf).
30. Ransohoff, D.F., M. McNaughton Collins, and F.J. Fowler, *Why is prostate cancer screening so common when the evidence is so uncertain? A system without negative feedback*. Am J Med, 2002. 113(8): p. 663-7.
31. Gore, J.L., et al., *Survivorship beyond convalescence: 48-month quality-of-life outcomes after treatment for localized prostate cancer*. J Natl Cancer Inst, 2009. 101(12): p. 888-92.
32. Potosky, A.L., et al., *Five-year outcomes after prostatectomy or radiotherapy for prostate cancer: the prostate cancer outcomes study*. J Natl Cancer Inst, 2004. 96(18): p. 1358-67.
33. Schover, L.R., et al., *Defining sexual outcomes after treatment for localized prostate carcinoma*. Cancer, 2002. 95(8): p. 1773-85.
34. Cheng, L.L., et al., *Enhanced resolution of proton NMR spectra of malignant lymph nodes using magic-angle spinning*. Magn Reson Med, 1996. 36(5): p. 653-8.

35. Cheng, L.L., et al., *Quantitative neuropathology by high resolution magic angle spinning proton magnetic resonance spectroscopy*. Proc Natl Acad Sci U S A, 1997. 94(12): p. 6408-13.
36. Decelle, E.A. and L.L. Cheng, *High-resolution magic angle spinning (1) H MRS in prostate cancer*. NMR Biomed, 2014. 27(1): p. 90-9.
37. Taylor, J.L., et al., *High-resolution magic angle spinning proton NMR analysis of human prostate tissue with slow spinning rates*. Magn Reson Med, 2003. 50(3): p. 627-32.
38. Shi, X., E. Gong, and X. Wu, *Alpha-methylacyl-CoA racemase/P504S overexpression in colorectal carcinoma is correlated with tumor differentiation*. Appl Immunohistochem Mol Morphol, 2007. 15(2): p. 175-80.
39. Kuefer, R., et al., *alpha-Methylacyl-CoA racemase: expression levels of this novel cancer biomarker depend on tumor differentiation*. Am J Pathol, 2002. 161(3): p. 841-8.
40. UC Davis, C., *Zeeman effect*. 2014 (http://chemwiki.ucdavis.edu/@api/deki/files/9303/Zeeaman_Effect.jpg).
41. Heisenberg, W., *Ueber den anschaulichen Inhalt der quantentheoretischen Kinematik und Mechanik*. Zeitschrift fuer Physik, 1927. 43(3-4): p. 172-198.
42. Wikipedia, *Magic Angle Spinning*. 2014 (<http://en.wikipedia.org/wiki/File:MagicAngleSpinning.svg>).
43. Melkus, G., *Development and application of spectroscopic 1H-NMR methods for in vivo characterisation of xenograft tumor models at 17.6 T*, F.f.P.u.A. Universität Würzburg, Editor. 2009: Würzburg.
44. Andrew, E.A., Bradbury, A., Eades, R.G., *Nuclear Magnetic Resonance Spectra from Crystal rotated at High Speed*. Nature, 1958. 182(4650): p. 1659.
45. Lowe, I.J., *Free Induction Decays of Rotating Solids*. Physical Review Letters, 1959. 2(7): p. 285 - 287.
46. Jordan, K.W., et al., *Evaluation of Tissue Metabolites with High Resolution Magic Angle Spinning MR Spectroscopy Human Prostate Samples After Three-Year Storage at -80 degrees C*. Biomark Insights, 2007. 2: p. 147-54.
47. Cheng, L.L., et al., *Quantification of microheterogeneity in glioblastoma multiforme with ex vivo high-resolution magic-angle spinning (HRMAS) proton magnetic resonance spectroscopy*. Neuro Oncol, 2000. 2(2): p. 87-95.
48. Cheng, L.L., et al., *Non-destructive quantitation of spermine in human prostate tissue samples using HRMAS 1H NMR spectroscopy at 9.4 T*. FEBS Lett, 2001. 494(1-2): p. 112-6.
49. Cheng, L.L., et al., *Correlation of high-resolution magic angle spinning proton magnetic resonance spectroscopy with histopathology of intact human brain tumor specimens*. Cancer Res, 1998. 58(9): p. 1825-32.

50. Cheng, L.L., et al., *Metabolic characterization of human prostate cancer with tissue magnetic resonance spectroscopy*. *Cancer Res*, 2005. 65(8): p. 3030-4.
51. M.H., L., *Spin dynamics: basic of nuclear magnetic resonance*. 2nd ed. 2008, West Sussex, England: John Wiley & Sons, Ltd.
52. Burns, M.A., et al., *Reduction of spinning sidebands in proton NMR of human prostate tissue with slow high-resolution magic angle spinning*. *Magn Reson Med*, 2005. 54(1): p. 34-42.
53. Chen, G.Y., et al., *[Assessment of P504S immunohistochemistry in diagnosis and differential diagnosis of prostatic adenocarcinoma]*. *Zhonghua Bing Li Xue Za Zhi*, 2004. 33(5): p. 419-23.
54. Oliver, S., *Functional Genomics: all the king's horses and all the king's men can put Humpty together again*. *Mol Cell*, 2003. 12(6): p. 1343-4.
55. Wikipedia. *Citrate*. 2014 <http://en.wikipedia.org/wiki/File:Citrate-3D-balls.png>].
56. Glunde, K., M.A. Jacobs, and Z.M. Bhujwalla, *Choline metabolism in cancer: implications for diagnosis and therapy*. *Expert Rev Mol Diagn*, 2006. 6(6): p. 821-9.
57. Glunde, K. and N.J. Serkova, *Therapeutic targets and biomarkers identified in cancer choline phospholipid metabolism*. *Pharmacogenomics*, 2006. 7(7): p. 1109-23.
58. Wikipedia. *Choline*. 2014 <http://en.wikipedia.org/wiki/File:Choline-cation-3D-balls.png>].
59. Swanson, M.G., et al., *Proton HR-MAS spectroscopy and quantitative pathologic analysis of MRI/3D-MRSI-targeted postsurgical prostate tissues*. *Magn Reson Med*, 2003. 50(5): p. 944-54.
60. van Asten, J.J., et al., *High resolution magic angle spinning NMR spectroscopy for metabolic assessment of cancer presence and Gleason score in human prostate needle biopsies*. *MAGMA*, 2008. 21(6): p. 435-42.
61. Tessem, M.B., et al., *Evaluation of lactate and alanine as metabolic biomarkers of prostate cancer using 1H HR-MAS spectroscopy of biopsy tissues*. *Magn Reson Med*, 2008. 60(3): p. 510-6.
62. Santos, C.F., et al., *Metabolic, pathologic, and genetic analysis of prostate tissues: quantitative evaluation of histopathologic and mRNA integrity after HR-MAS spectroscopy*. *NMR Biomed*, 2010. 23(4): p. 391-8.
63. Swanson, M.G., et al., *Quantification of choline- and ethanolamine-containing metabolites in human prostate tissues using 1H HR-MAS total correlation spectroscopy*. *Magn Reson Med*, 2008. 60(1): p. 33-40.
64. Wikipedia. *Creatine*. 2014 <http://en.wikipedia.org/wiki/File:Creatine-3D-balls.png>].
65. Males, R.G., et al., *Clinical application of BASING and spectral/spatial water and lipid suppression pulses for prostate cancer staging and localization by in vivo 3D 1H magnetic resonance spectroscopic imaging*. *Magn Reson Med*, 2000. 43(1): p. 17-22.

66. Kurth, J., E. Defeo, and L.L. Cheng, *Magnetic resonance spectroscopy: a promising tool for the diagnostics of human prostate cancer?* Urol Oncol, 2011. 29(5): p. 562-71.
67. Sreekumar, A., et al., *Metabolomic profiles delineate potential role for sarcosine in prostate cancer progression.* Nature, 2009. 457(7231): p. 910-4.
68. Swanson, M.G., et al., *Quantitative analysis of prostate metabolites using 1H HR-MAS spectroscopy.* Magn Reson Med, 2006. 55(6): p. 1257-64.
69. Cheng, L.L., et al., *Evaluating human breast ductal carcinomas with high-resolution magic-angle spinning proton magnetic resonance spectroscopy.* J Magn Reson, 1998. 135(1): p. 194-202.
70. Cheng, L.L., et al., *Quantification of neurons in Alzheimer and control brains with ex vivo high resolution magic angle spinning proton magnetic resonance spectroscopy and stereology.* Magn Reson Imaging, 2002. 20(7): p. 527-33.
71. Tzika, A.A., et al., *Biochemical characterization of pediatric brain tumors by using in vivo and ex vivo magnetic resonance spectroscopy.* J Neurosurg, 2002. 96(6): p. 1023-31.
72. Ramos-Vara, J.A., *Technical aspects of immunohistochemistry.* Vet Pathol, 2005. 42(4): p. 405-26.
73. Jiang, Z., et al., *Using an AMACR (P504S)/34betaE12/p63 cocktail for the detection of small focal prostate carcinoma in needle biopsy specimens.* Am J Clin Pathol, 2005. 123(2): p. 231-6.
74. Carswell, B.M., et al., *Detection of prostate cancer by alpha-methylacyl CoA racemase (P504S) in needle biopsy specimens previously reported as negative for malignancy.* Histopathology, 2006. 48(6): p. 668-73.
75. Beach, R., et al., *P504S immunohistochemical detection in 405 prostatic specimens including 376 18-gauge needle biopsies.* Am J Surg Pathol, 2002. 26(12): p. 1588-96.
76. Jiang, Z., et al., *Discovery and clinical application of a novel prostate cancer marker: alpha-methylacyl CoA racemase (P504S).* Am J Clin Pathol, 2004. 122(2): p. 275-89.
77. Koenig, C., et al., *Carcinoma Arising in Microglandular Adenosis: An Immunohistochemical Analysis of 20 Intraepithelial and Invasive Neoplasms.* Int J Surg Pathol, 2000. 8(4): p. 303-315.
78. Wu, M., et al., *p63 and TTF-1 immunostaining. A useful marker panel for distinguishing small cell carcinoma of lung from poorly differentiated squamous cell carcinoma of lung.* Am J Clin Pathol, 2003. 119(5): p. 696-702.
79. Deutsch, G.B., et al., *Quality control in oocytes: domain-domain interactions regulate the activity of p63.* Cell Cycle, 2011. 10(12): p. 1884-5.
80. Ud Din, N., A. Qureshi, and S. Mansoor, *Utility of p63 immunohistochemical stain in differentiating urothelial carcinomas from adenocarcinomas of prostate.* Indian J Pathol Microbiol, 2011. 54(1): p. 59-62.

81. Jiang, Z., et al., *P504S/alpha-methylacyl-CoA racemase: a useful marker for diagnosis of small foci of prostatic carcinoma on needle biopsy*. *Am J Surg Pathol*, 2002. 26(9): p. 1169-74.
82. Tacha, D.E. and R.T. Miller, *Use of p63/P504S monoclonal antibody cocktail in immunohistochemical staining of prostate tissue*. *Appl Immunohistochem Mol Morphol*, 2004. 12(1): p. 75-8.
83. Iomonitoring. *MR Physics*. 2014 <http://www.iomonitoring.pro/mrphysics.htm>].
84. Marshall, I., et al., *Use of Voigt lineshape for quantification of in vivo 1H spectra*. *Magn Reson Med*, 1997. 37(5): p. 651-7.
85. Kumaresan, K., et al., *Diagnostic utility of alpha-methylacyl CoA racemase (P504S) & HMWCK in morphologically difficult prostate cancer*. *Diagn Pathol*, 2010. 5: p. 83.
86. Shi, S.R., M.E. Key, and K.L. Kalra, *Antigen retrieval in formalin-fixed, paraffin-embedded tissues: an enhancement method for immunohistochemical staining based on microwave oven heating of tissue sections*. *J Histochem Cytochem*, 1991. 39(6): p. 741-8.
87. Leong, T.Y. and A.S. Leong, *How does antigen retrieval work?* *Adv Anat Pathol*, 2007. 14(2): p. 129-31.
88. Shi, S.R., R.J. Cote, and C.R. Taylor, *Antigen retrieval immunohistochemistry: past, present, and future*. *J Histochem Cytochem*, 1997. 45(3): p. 327-43.
89. Shi, S.R., R.J. Cote, and C.R. Taylor, *Antigen retrieval techniques: current perspectives*. *J Histochem Cytochem*, 2001. 49(8): p. 931-7.
90. D'Amico, F., E. Skarmoutsou, and F. Stivala, *State of the art in antigen retrieval for immunohistochemistry*. *J Immunol Methods*, 2009. 341(1-2): p. 1-18.
91. Dakshinamurti, K. and S.P. Mistry, *Amino acid incorporation and biotin deficiency*. *J Biol Chem*, 1963. 238: p. 297-301.
92. Sourceforge. *Hugin - Panorama photo stitcher*. 2013 <http://hugin.sourceforge.net/>].
93. Koppenol, W.H., P.L. Bounds, and C.V. Dang, *Otto Warburg's contributions to current concepts of cancer metabolism*. *Nat Rev Cancer*, 2011. 11(5): p. 325-37.
94. Kurhanewicz, J., et al., *Combined magnetic resonance imaging and spectroscopic imaging approach to molecular imaging of prostate cancer*. *J Magn Reson Imaging*, 2002. 16(4): p. 451-63.
95. McDunn, J.E., et al., *Metabolomic signatures of aggressive prostate cancer*. *Prostate*, 2013. 73(14): p. 1547-60.
96. DeFeo, E.M., et al., *A decade in prostate cancer: from NMR to metabolomics*. *Nat Rev Urol*, 2011. 8(6): p. 301-11.
97. DeFeo, E.M. and L.L. Cheng, *Characterizing human cancer metabolomics with ex vivo 1H HRMAS MRS*. *Technol Cancer Res Treat*, 2010. 9(4): p. 381-91.

98. Spur, E.M., E.A. Decelle, and L.L. Cheng, *Metabolomic imaging of prostate cancer with magnetic resonance spectroscopy and mass spectrometry*. Eur J Nucl Med Mol Imaging, 2013. 40 Suppl 1: p. S60-71.
99. Glunde, K. and Z.M. Bhujwala, *Metabolic tumor imaging using magnetic resonance spectroscopy*. Semin Oncol, 2011. 38(1): p. 26-41.
100. Glunde, K., et al., *MRS and MRSI guidance in molecular medicine: targeting and monitoring of choline and glucose metabolism in cancer*. NMR Biomed, 2011. 24(6): p. 673-90.
101. Righi, V., et al., *¹H HR-MAS and genomic analysis of human tumor biopsies discriminate between high and low grade astrocytomas*. NMR Biomed, 2009. 22(6): p. 629-37.
102. Moestue, S.A., et al., *Glycerophosphocholine (GPC) is a poorly understood biomarker in breast cancer*. Proc Natl Acad Sci U S A, 2012. 109(38): p. E2506; author reply E2507.
103. Costello, L.C., et al., *Zinc causes a shift toward citrate at equilibrium of the m-aconitase reaction of prostate mitochondria*. J Inorg Biochem, 2000. 78(2): p. 161-5.
104. Verma, S., et al., *Prostate MRI and 3D MR spectroscopy: how we do it*. AJR Am J Roentgenol, 2010. 194(6): p. 1414-26.
105. Kobus, T., et al., *In vivo assessment of prostate cancer aggressiveness using magnetic resonance spectroscopic imaging at 3 T with an endorectal coil*. Eur Urol, 2011. 60(5): p. 1074-80.
106. Giskeodegard, G.F., et al., *Spermine and citrate as metabolic biomarkers for assessing prostate cancer aggressiveness*. PLoS One, 2013. 8(4): p. e62375.
107. Jentzmik, F., et al., *Sarcosine in urine after digital rectal examination fails as a marker in prostate cancer detection and identification of aggressive tumours*. Eur Urol, 2010. 58(1): p. 12-8; discussion 20-1.
108. Cao, D.L., et al., *Efforts to resolve the contradictions in early diagnosis of prostate cancer: a comparison of different algorithms of sarcosine in urine*. Prostate Cancer Prostatic Dis, 2011. 14(2): p. 166-72.
109. Wu, H., et al., *GC/MS-based metabolomic approach to validate the role of urinary sarcosine and target biomarkers for human prostate cancer by microwave-assisted derivatization*. Anal Bioanal Chem, 2011. 401(2): p. 635-46.
110. Startribune. *Giant magnet makes U attractive to brain mapping researchers*. <http://www.startribune.com/lifestyle/health/235171471.html> 2013 [cited 2014 02.03.2014].
111. Nature. *Brain imaging: fMRI 2.0*. <http://www.nature.com/news/brain-imaging-fmri-2-0-1.10365> 2012 [cited 2014 02.03.2014].
112. Siegel, R., et al., *Cancer statistics, 2014*. CA Cancer J Clin, 2014. 64(1): p. 9-29.

11 Erklärung über die eigenständige Abfassung der Arbeit

Hiermit erkläre ich, dass ich die vorliegende Arbeit selbständig und ohne unzulässige Hilfe oder Benutzung anderer als der angegebenen Hilfsmittel angefertigt habe. Ich versichere, dass Dritte von mir weder unmittelbar noch mittelbar geldwerte Leistungen für Arbeiten erhalten haben, die im Zusammenhang mit dem Inhalt der vorgelegten Dissertation stehen, und dass die vorgelegte Arbeit weder im Inland noch im Ausland in gleicher oder ähnlicher Form einer anderen Prüfungsbehörde zum Zweck einer Promotion oder eines anderen Prüfungsverfahrens vorgelegt wurde. Alles aus anderen Quellen und von anderen Personen übernommene Material, das in der Arbeit verwendet wurde oder auf das direkt Bezug genommen wird, wurde als solches kenntlich gemacht. Insbesondere wurden alle Personen genannt, die direkt an der Entstehung der vorliegenden Arbeit beteiligt waren.

.....

Datum

.....

Unterschrift

12 Danksagung

Diese Arbeit wäre in der vorliegenden Form niemals ohne die tatkräftige Unterstützung einer Reihe von Personen möglich gewesen, bei denen ich mich hiermit herzlichst bedanken möchte. Ein großes Dankeschön geht daher an:

Meinen Promotionsbetreuer, Professor Daniel Huster vom Institut für Medizinische Physik und Biophysik an der Universität Leipzig, welcher mir beständig bei der Abfassung der Arbeit zur Seite stand.

Professor Leo L. Cheng, Leiter des Radiopathology Laboratory des Massachusetts General Hospitals in Boston, für die Möglichkeit zum Erlernen der Hochfeldspektroskopie, die Bereitstellung eines Laborplatzes und jederzeit ausreichenden Arbeitsmaterialien, aber vor allem für den wissenschaftlichen Freiraum und die intellektuelle Unterstützung bei der Entwicklung und Durchführung eines eigenständigen Forschungsprojektes.

Yannick Berker für seine enorme Hilfe bei der Erstellung des Auswertungsprogramms für die Immunhistochemie.

Johannes Nowak und Piet Habel für die Gelegenheit zum Forschungsaufenthalt in Boston. Den Mitgliedern des Cheng- Labors, sowie den Teams der Abteilungen für Pathologie am Brigham and Women's Hospital und Massachusetts General Hospital.

Dr. Thomas Riemer vom Institut für Medizinische Physik für seine ausführlichen Korrekturhinweise zum NMR-Kapitel.

Andreas Maxeiner und Süleyman Bilal für unermüdliche Unterstützung und Freundschaft während des Aufenthaltes in Boston.

Meine Schwester Ulrike, Jan Sedlacik und Julius Chapiro für die wissenschaftliche Unterstützung bei der Erstellung der Arbeit, hervorragende Korrekturhinweise, sowie jederzeit motivierende Worte.

Und schließlich möchte ich mich ganz besonders bei meinen Eltern bedanken, die mir ein Medizinstudium und den Forschungsaufenthalt in Boston ermöglichten und mir in jeder Lebenslage unterstützend zur Seite standen. Ihnen möchte ich die vorliegende Arbeit widmen. Vielen Dank!

13 Lebenslauf und Publikationsverzeichnis

Appendix

A.1 Staining Protocols

Table A1: IHC staining procedure summary

	P504S	CK903	P63
Preparation	Deparaffinization and dehydration		
Antigen retrieval	TRIS/EDTA buffer (pH 9.0, 10mM/1mM) 30 min	Citrate buffer (pH 6.0, 0.1mM) 30 min	
Quenching of endogenous peroxides	3% H ₂ O ₂ in methanol 10min		
Protein block	Protein block solution 3-4 drops (150-200µl), 10min		
First incubation: primary antibody	Rabbit monoclonal anti-human AMACR, 200 µl, 75 min	Mouse monoclonal anti-human CK903, 200 µl, 75 min	Mouse monoclonal anti-human p63, 200 µl, 75 min
Buffer wash	PBS, 5 min		
Second incubation: secondary antibody	Biotinylated anti-rabbit IgG (1:50), 150µl, 30 min	Biotinylated anti-mouse IgG (1:50), 150µl, 30 min	
Buffer wash	PBS, 5 min		
Third incubation	Avidin / Biotin / Peroxidase complex (ABC), RTU agent 5-6 drops, 30 min		
Visualization	Diaminobenzidine-3,3' 250µl, 10 min		
Post-processing	Counterstain, Dehydration, Cover slip		

Table A2: Hematoxylin & Eosin – staining protocol

Immunostaining step	Chemicals / Agents applied	Time
Deparaffinazation and rehydration	Xylene I	5 min
	Xylene II	5 min
	Xylene III	5 min
	100% EtOHI	5 min
	100% EtOHII	5 min
	95% EtOH	5 min
	70% EtOH	5 min
	deionized H ₂ O I	5 min
	deionized H ₂ O II	5 min
Hematoxylin & Eosin staining	Hematoxylin	4 min
	deionized H ₂ O	3 min
	Sodium Borate 4% in H ₂ O	1 dip
	95% EtOH	2 min
	Eosin	3.5 min
Dehydration and fixation	95% EtOH	3 dips
	95% EtOH	3 dips
	100% EtOHI	1 min
	100% EtOHII	1 min
	Xylene I	5 min
	Xylene II	5 min
	Permanent mounting media	Overnight

A.2 Spectral Intensities Measured by ¹H HRMAS MRS in 51 Samples

Table A3: Spectral intensities in samples 1-10

ROI / Sample	1	2	3	4	5	6	7	8	9	10
4.14-4.11	0.04221	0.01318	0.02364	0.01668	0.01899	0.02933	0.02575	0.02318	0.02979	0.02798
4.05	0.02668	0.00873	0.02842	0.01221	0.01602	0.02174	0.01436	0.02063	0.02134	0.02690
3.99-3.96	0.00000	0.00523	0.00000	0.00000	0.00072	0.01272	0.00914	0.00000	0.00248	0.00000
3.94-3.93	0.01262	0.06418	0.00595	0.00000	0.01033	0.00586	0.01346	0.02494	0.00889	0.01444
3.78	0.00012	0.00000	0.00000	0.00000	0.00020	0.00130	0.00093	0.00374	0.00289	0.00000
3.75	0.00082	0.00000	0.03191	0.00000	0.00000	0.00103	0.00170	0.00023	0.00079	0.00420
3.74-3.71	0.00018	0.00000	0.00000	0.00000	0.00250	0.20307	0.00444	0.00160	0.00085	0.00156
3.63	0.00549	0.00217	0.00521	0.01534	0.01035	0.00000	0.00000	0.00369	0.00262	0.00436
3.62	0.01556	0.00674	0.01818	0.02754	0.01437	0.00427	0.00312	0.01353	0.00975	0.01501
3.6	0.01018	0.00356	0.01442	0.02066	0.00836	0.02012	0.01004	0.00690	0.00421	0.00678
3.34	0.00115	0.01318	0.00576	0.00695	0.00770	0.01243	0.00336	0.00561	0.00475	0.00708
3.29	0.00264	0.00000	0.00106	0.00344	0.00153	0.00035	0.00000	0.00120	0.00124	0.00316
3.27	0.00176	0.00216	0.00806	0.01576	0.00807	0.00459	0.00012	0.00920	0.00773	0.01324
3.26	0.04476	0.00904	0.01348	0.01920	0.01405	0.01301	0.00000	0.02680	0.00745	0.02342
3.24	0.00000	0.00193	0.00734	0.00000	0.00000	0.02925	0.00760	0.00000	0.00158	0.00000
3.22	0.00947	0.01749	0.01281	0.01486	0.01970	0.02749	0.00294	0.01533	0.01077	0.01174
3.2	0.03190	0.02538	0.02014	0.02161	0.01597	0.07432	0.02424	0.01634	0.01309	0.02254
3.15-3.1	0.01193	0.00000	0.00291	0.00630	0.00329	0.01149	0.00000	0.00724	0.06425	0.00723
3.09-3.05	0.00000	0.00000	0.00010	0.00000	0.00000	0.03821	0.00000	0.01463	0.02582	0.00838
3.03	0.01341	0.01487	0.01284	0.00958	0.00992	0.00811	0.00197	0.01965	0.00996	0.01897
2.71	0.01142	0.01469	0.00677	0.02526	0.00878	0.00372	0.00000	0.00824	0.01521	0.01603
2.68	0.00559	0.01028	0.00667	0.01534	0.01268	0.02947	0.00000	0.00958	0.01071	0.01272
2.55	0.00418	0.00964	0.00530	0.01813	0.00117	0.01012	0.00465	0.01747	0.01565	0.01079
2.52	0.00509	0.02215	0.00678	0.01519	0.01157	0.00336	0.00386	0.01267	0.00883	0.02335
2.45-2.43	0.00000	0.00000	0.00000	0.00000	0.00000	0.01784	0.00000	0.00273	0.00000	0.00000
2.42-2.4	0.00096	0.00000	0.00070	0.00090	0.00000	0.00773	0.00217	0.00927	0.00144	0.00000
2.36	0.00000	0.00000	0.00000	0.00000	0.00000	0.00000	0.00000	0.00000	0.00000	0.00159
2.35	0.00594	0.00000	0.00181	0.00128	0.00113	0.00000	0.00000	0.01173	0.00000	0.00251
2.34	0.00000	0.00947	0.00327	0.00481	0.00341	0.00000	0.00117	0.00000	0.00445	0.00334
2.33-2.3	0.00630	0.00000	0.00193	0.00418	0.01287	0.00861	0.02204	0.00906	0.00000	0.00331
1.48-1.46	0.00222	0.00490	0.00617	0.00487	0.00402	0.00000	0.00388	0.00201	0.00653	0.00292
1.34-1.32	0.15193	0.06688	0.10292	0.12103	0.10623	0.00117	0.03057	0.09805	0.07438	0.09194
1.28	0.02794	0.02327	0.01163	0.00000	0.02217	0.00000	0.07079	0.02371	0.00000	0.02380
1.2	0.00000	0.00000	0.00085	0.00014	0.00000	0.00000	0.00002	0.00000	0.00661	0.00000
0.96-0.93	0.00838	0.00657	0.01206	0.01440	0.01556	0.00000	0.00803	0.00947	0.00783	0.01552
0.9	0.01847	0.01545	0.00001	0.00040	0.00443	0.00000	0.00409	0.00911	0.00792	0.00329

Table A4: Spectral intensities in samples 11 - 20

ROI / Sample	11	12	13	14	15	16	17	18	19	20
4.14-4.11	0.01227	0.02898	0.03277	0.04463	0.03383	0.01727	0.02322	0.01972	0.01443	0.03933
4.05	0.02054	0.02961	0.01816	0.07243	0.01526	0.01144	0.02421	0.01508	0.01120	0.02084
3.99-3.96	0.00000	0.03721	0.00693	0.17284	0.00976	0.00298	0.00805	0.00493	0.00000	0.00000
3.94-3.93	0.00669	0.04435	0.01336	0.03225	0.01231	0.02520	0.00743	0.00922	0.01251	0.00661
3.78	0.00254	0.00000	0.01220	0.00000	0.00176	0.00309	0.00724	0.00110	0.00386	0.00222
3.75	0.03987	0.00000	0.00043	0.06838	0.00258	0.01287	0.00378	0.00179	0.00000	0.01290
3.74-3.71	0.00000	0.00000	0.00000	0.00000	0.00000	0.00994	0.00000	0.00000	0.00000	0.00000
3.63	0.00559	0.00530	0.01025	0.00379	0.00436	0.00335	0.00756	0.00323	0.00414	0.00588
3.62	0.01518	0.01204	0.01759	0.01429	0.01175	0.00948	0.01767	0.01180	0.00614	0.01451
3.6	0.01152	0.00660	0.01091	0.01238	0.00659	0.00675	0.01883	0.00601	0.00455	0.01205
3.34	0.00620	0.00799	0.01587	0.00543	0.00601	0.00147	0.01489	0.00306	0.00282	0.00345
3.29	0.00056	0.00000	0.00000	0.00000	0.00110	0.00000	0.00823	0.00176	0.00170	0.00134
3.27	0.01015	0.01650	0.00107	0.00000	0.01411	0.00999	0.02512	0.01043	0.00765	0.01132
3.26	0.00000	0.01680	0.00000	0.00251	0.01389	0.01485	0.02303	0.01562	0.01315	0.01230
3.24	0.03820	0.00000	0.02180	0.01878	0.00000	0.00000	0.01070	0.00405	0.00000	0.00866
3.22	0.00660	0.00944	0.00000	0.01273	0.02871	0.01564	0.03487	0.00552	0.01301	0.01691
3.2	0.02099	0.01190	0.01699	0.01932	0.02597	0.00458	0.03401	0.01602	0.01404	0.01940
3.15-3.1	0.03229	0.00000	0.07126	0.04399	0.00609	0.00000	0.01180	0.01775	0.00000	0.00561
3.09-3.05	0.00728	0.00000	0.04379	0.05184	0.00127	0.00000	0.00000	0.00170	0.00000	0.00268
3.03	0.01156	0.00000	0.07289	0.02561	0.01392	0.01084	0.00630	0.01163	0.00748	0.01524
2.71	0.00216	0.00000	0.01146	0.01000	0.00195	0.00000	0.00233	0.00699	0.01267	0.00364
2.68	0.00000	0.00000	0.00625	0.01832	0.00353	0.00000	0.00692	0.00842	0.01061	0.00939
2.55	0.00165	0.00000	0.01052	0.00707	0.00254	0.00062	0.00651	0.00930	0.00185	0.00698
2.52	0.00659	0.00000	0.00844	0.02735	0.00353	0.00090	0.00754	0.00917	0.00102	0.01314
2.45-2.43	0.00157	0.00000	0.00000	0.00000	0.00000	0.00000	0.00000	0.00000	0.00242	0.00000
2.42-2.4	0.00097	0.00000	0.00119	0.00109	0.00251	0.00551	0.00175	0.00102	0.00000	0.00205
2.36	0.00211	0.00000	0.00000	0.00000	0.00520	0.00000	0.00231	0.00068	0.00000	0.00134
2.35	0.00000	0.00000	0.00523	0.00073	0.00417	0.01663	0.00429	0.00339	0.00232	0.00352
2.34	0.00522	0.00000	0.00000	0.00289	0.00948	0.00000	0.00787	0.00379	0.00000	0.00511
2.33-2.3	0.00384	0.00000	0.00432	0.01152	0.00000	0.01230	0.00000	0.00161	0.00000	0.00000
1.48-1.46	0.00202	0.00000	0.00688	0.00305	0.00506	0.01540	0.01325	0.00227	0.00749	0.00715
1.34-1.32	0.04700	0.00000	0.09321	0.12368	0.10976	0.11945	0.13979	0.09176	0.09347	0.10916
1.28	0.01116	0.00000	0.02466	0.07138	0.09506	0.02698	0.05279	0.07373	0.13369	0.00746
1.2	0.00264	0.00000	0.00227	0.00000	0.00000	0.00086	0.02582	0.00000	0.00144	0.00033
0.96-0.93	0.00283	0.00000	0.01190	0.01614	0.01171	0.01643	0.01534	0.01369	0.00631	0.01896
0.9	0.00234	0.00000	0.00889	0.00685	0.03072	0.00240	0.00445	0.00615	0.05283	0.00585

Table A5: Spectral intensities in samples 21 - 30

Roi / Sample	21	22	23	24	25	26	27	28	29	30
4.14-4.11	000321	0.02608	0.02793	0.01813	0.01170	0.02353	0.02281	0.02262	0.02722	0.01435
4.05	0.00128	0.01847	0.02444	0.01459	0.02067	0.01307	0.01510	0.01389	0.02879	0.01445
3.99-3.96	0.00339	0.00000	0.00949	0.00363	0.00031	0.00075	0.00097	0.00000	0.00179	0.00537
3.94-3.93	0.00548	0.00621	0.02174	0.00379	0.00253	0.00876	0.00479	0.00820	0.00936	0.01237
3.78	0.00293	0.00321	0.00000	0.00495	0.00570	0.00622	0.00231	0.00912	0.00468	0.00389
3.75	0.00370	0.00200	0.00180	0.00228	0.00245	0.00349	0.00054	0.00338	0.00191	0.01118
3.74-3.71	0.01465	0.00000	0.00000	0.00000	0.00000	0.00531	0.00000	0.00000	0.00000	0.02584
3.63	0.00395	0.00604	0.00378	0.00349	0.00937	0.01083	0.01666	0.00426	0.02922	0.01395
3.62	0.00755	0.01409	0.01389	0.00808	0.01707	0.00699	0.00934	0.01394	0.00000	0.01711
36	0.00600	0.01152	0.01383	0.00626	0.01916	0.00271	0.00712	0.01052	0.01647	0.02497
3.34	0.00132	0.00317	0.00000	0.00168	0.01018	0.00469	0.00580	0.00430	0.01002	0.00413
3.29	0.00094	0.00196	0.00000	0.00239	0.00330	0.00134	0.00513	0.00238	0.00444	0.00586
3.27	0.00471	0.00925	0.00000	0.00208	0.00581	0.00547	0.00866	0.01409	0.01466	0.00778
3.26	0.00542	0.05014	0.00000	0.01658	0.02375	0.01833	0.00822	0.02623	0.01165	0.00875
3.24	0.00381	0.00000	0.00000	0.00120	0.00702	0.00483	0.00524	0.00000	0.00834	0.00614
3.22	0.00773	0.02838	0.00000	0.00703	0.01741	0.01018	0.01121	0.01767	0.00637	0.00940
32	0.00887	0.02147	0.00000	0.00043	0.03266	0.01224	0.01370	0.01154	0.01542	0.01238
3.15-3.1	0.00035	0.00101	0.00000	0.00563	0.07256	0.04165	0.02799	0.00504	0.00294	0.01490
3.09-3.05	0.00000	0.00000	0.00000	0.00519	0.00122	0.00129	0.02180	0.00000	0.00355	0.00172
303	0.00469	0.01666	0.00000	0.00435	0.01334	0.01264	0.00303	0.02480	0.02404	0.00550
2.71	0.00197	0.00089	0.00000	0.00931	0.01017	0.00235	0.01288	0.00513	0.01801	0.01076
2.68	0.00104	0.00820	0.00000	0.01095	0.00013	0.00000	0.00000	0.00172	0.02288	0.00000
2.55	0.00272	0.00498	0.00000	0.00996	0.01235	0.00421	0.00783	0.00545	0.01402	0.00203
2.52	0.00140	0.00992	0.00000	0.00691	0.01135	0.00272	0.00000	0.00909	0.01504	0.00166
2.45-2.43	0.00000	0.00000	0.00000	0.00259	0.00264	0.00229	0.00103	0.00052	0.00000	0.00215
2.42-2.4	0.00000	0.00000	0.00000	0.00205	0.00066	0.00000	0.00000	0.00356	0.00000	0.00639
2.36	0.00196	0.00267	0.00000	0.00134	0.01099	0.00559	0.00328	0.00240	0.00767	0.01915
2.35	0.00181	0.00319	0.00000	0.00628	0.00000	0.00346	0.00743	0.00575	0.00000	0.00000
2.34	0.00280	0.00462	0.00000	0.00000	0.00197	0.00000	0.00000	0.00000	0.01624	0.00000
2.33-2.3	0.00000	0.00000	0.00000	0.00364	0.01461	0.00982	0.00111	0.00792	0.00000	0.02840
1.48-1.46	0.00121	0.00892	0.00000	0.00259	0.00767	0.00537	0.01004	0.00715	0.00780	0.00059
1.34-1.32	0.08476	0.12480	0.00000	0.07110	0.05916	0.07489	0.06441	0.10963	0.12399	0.06112
1.28	0.09282	0.01348	0.00000	0.05935	0.05350	0.01511	0.02401	0.07369	0.06723	0.08683
1.2	0.00128	0.00000	0.00000	0.00000	0.01362	0.00022	0.00932	0.00000	0.06307	0.01187
0.96-0.93	0.00621	0.01083	0.00000	0.01542	0.00772	0.00800	0.00870	0.00859	0.01416	0.01768
0.9	0.01010	0.01085	0.00000	0.00291	0.00335	0.00000	0.01066	0.00382	0.02046	0.03727

Table A6: Spectral intensities in samples 31-40

ROI	31	32	33	34	35	36	37	38	39	40
4.14-4.11	0.02748	0.01776	0.01125	0.01300	0.02373	0.01075	0.01428	0.01470	0.02681	0.01504
4.05	0.03705	0.00000	0.01359	0.00744	0.01341	0.02103	0.00895	0.01130	0.00455	0.01812
3.99-3.96	0.00376	0.00309	0.00228	0.00187	0.00044	0.00028	0.00037	0.00000	0.00382	0.00077
3.94-3.93	0.00823	0.00272	0.01037	0.00075	0.00549	0.00456	0.00353	0.00627	0.00633	0.00532
3.78	0.01076	0.00015	0.00607	0.00216	0.00416	0.00353	0.00209	0.00330	0.00292	0.00641
3.75	0.00404	0.00000	0.00646	0.00170	0.00226	0.00057	0.00029	0.00142	0.00162	0.00082
3.74-3.71	0.01116	0.00192	0.02155	0.00355	0.00085	0.00071	0.00000	0.01426	0.00000	0.00383
3.63	0.00559	0.00162	0.00200	0.00777	0.02087	0.00792	0.00964	0.00399	0.00419	0.01264
3.62	0.01603	0.00089	0.01560	0.00700	0.02558	0.01578	0.01302	0.00789	0.01385	0.01748
3.6	0.00857	0.00975	0.01372	0.00360	0.00435	0.00733	0.00325	0.00310	0.00156	0.01306
3.34	0.00331	0.03402	0.00000	0.00155	0.01024	0.00150	0.00041	0.00149	0.00353	0.00504
3.29	0.00137	0.01295	0.00000	0.00392	0.00897	0.00053	0.00157	0.00075	0.00687	0.00245
3.27	0.00979	0.02100	0.00000	0.00409	0.01172	0.00435	0.00404	0.00741	0.01046	0.00608
3.26	0.02271	0.01922	0.00000	0.00525	0.01231	0.01443	0.01084	0.00000	0.01146	0.01052
3.24	0.00000	0.02048	0.00000	0.00345	0.00893	0.00572	0.00065	0.01727	0.01275	0.00689
3.22	0.01249	0.00397	0.00000	0.00591	0.02233	0.00615	0.00798	0.01034	0.01483	0.00823
3.2	0.01078	0.01144	0.00000	0.00721	0.02605	0.00745	0.00686	0.01220	0.01509	0.01457
3.15-3.1	0.00641	0.00000	0.00000	0.00844	0.02683	0.02570	0.00115	0.00363	0.00053	0.03223
3.09-3.05	0.02494	0.01526	0.00000	0.00096	0.01360	0.00071	0.01145	0.00104	0.01082	0.00323
3.03	0.00980	0.00000	0.00000	0.00317	0.01507	0.01044	0.00138	0.01204	0.00159	0.00208
2.71	0.00905	0.00245	0.00000	0.00409	0.02081	0.01342	0.01644	0.00798	0.00236	0.01080
2.68	0.01340	0.00251	0.00000	0.00000	0.02540	0.00988	0.01560	0.00231	0.00191	0.00965
2.55	0.00927	0.00129	0.00000	0.00129	0.01604	0.00545	0.01668	0.00757	0.00201	0.01217
2.52	0.00527	0.00338	0.00000	0.00177	0.01841	0.00496	0.01829	0.00310	0.00243	0.00178
2.45-2.43	0.00000	0.00000	0.00000	0.00000	0.00000	0.00044	0.00077	0.00068	0.00328	0.00000
2.42-2.4	0.00770	0.00584	0.00000	0.00000	0.00000	0.00040	0.00017	0.00018	0.00000	0.00000
2.36	0.00063	0.00339	0.00000	0.00577	0.00630	0.00425	0.00346	0.00305	0.00342	0.00243
2.35	0.00194	0.00647	0.00000	0.00306	0.00000	0.00335	0.00223	0.00365	0.00000	0.00172
2.34	0.00455	0.01035	0.00000	0.00000	0.00869	0.00000	0.00078	0.00000	0.00301	0.00000
2.33-2.3	0.01838	0.00846	0.00000	0.00983	0.01298	0.00709	0.00382	0.00423	0.00310	0.00000
1.48-1.46	0.00495	0.00000	0.00000	0.00295	0.00720	0.00419	0.00465	0.00543	0.00248	0.00350
1.34-1.32	0.09820	0.07400	0.00000	0.05067	0.09751	0.06178	0.06864	0.05167	0.08219	0.05444
1.28	0.03550	0.04424	0.00000	0.08703	0.10690	0.02427	0.06987	0.07582	0.14441	0.02116
1.2	0.00067	0.00918	0.00000	0.00000	0.05177	0.00195	0.01348	0.00527	0.00910	0.00250
0.96-0.93	0.00823	0.01261	0.00000	0.00231	0.00972	0.00752	0.00330	0.00494	0.00629	0.02704
0.9	0.01260	0.01155	0.00000	0.00995	0.01605	0.00256	0.00364	0.00405	0.00384	0.01373

Table A7: Spectral intensities in samples 41-46

ROI	41	42	43	44	45	46
4.14-4.11	0.00557	0.01659	0.02709	0.02361	0.01180	0.01990
4.05	0.01562	0.01359	0.02887	0.02120	0.00732	0.01513
3.99-3.96	0.00673	0.00191	0.00136	0.00346	0.00349	0.00317
3.94-3.93	0.01158	0.00611	0.01518	0.00960	0.00361	0.00933
3.78	0.02570	0.00322	0.00245	0.00338	0.00251	0.00389
3.75	0.00619	0.00035	0.00131	0.00107	0.00081	0.00347
3.74-3.71	0.03482	0.00000	0.00000	0.00000	0.00000	0.00000
3.63	0.00150	0.00876	0.00508	0.02564	0.00578	0.00765
3.62	0.00811	0.01281	0.01294	0.01166	0.00336	0.00407
3.6	0.01286	0.00660	0.00550	0.00202	0.00315	0.00172
3.34	0.00300	0.00265	0.00581	0.00599	0.00145	0.00204
3.29	0.00247	0.00167	0.00000	0.00227	0.00053	0.00118
3.27	0.00507	0.00578	0.00590	0.00716	0.00225	0.00612
3.26	0.00578	0.01447	0.00004	0.01615	0.00537	0.00999
3.24	0.00212	0.00241	0.01023	0.00395	0.00429	0.01152
3.22	0.01192	0.00826	0.00445	0.00518	0.01268	0.00960
3.2	0.00738	0.00595	0.00564	0.00641	0.00931	0.00751
3.15-3.1	0.00382	0.02095	0.02813	0.01649	0.00000	0.00284
3.09-3.05	0.00095	0.00130	0.01729	0.01160	0.00001	0.00000
3.03	0.00576	0.01024	0.00801	0.01349	0.00649	0.00341
2.71	0.00447	0.03292	0.01081	0.00381	0.00125	0.00576
2.68	0.00546	0.00878	0.00186	0.00187	0.00127	0.00743
2.55	0.00539	0.01952	0.00850	0.00259	0.00107	0.00492
2.52	0.00286	0.02285	0.00266	0.00340	0.00017	0.00535
2.45-2.43	0.00000	0.00000	0.00180	0.00000	0.00000	0.00172
2.42-2.4	0.00119	0.00000	0.00431	0.00000	0.00023	0.00313
2.36	0.00156	0.00341	0.00186	0.00703	0.00588	0.00105
2.35	0.00369	0.00000	0.00630	0.00000	0.00547	0.00246
2.34	0.00228	0.00000	0.00000	0.00429	0.00371	0.00604
2.33-2.3	0.00034	0.00584	0.00000	0.00785	0.00764	0.00292
1.48-1.46	0.00523	0.00844	0.00393	0.01071	0.00980	0.00882
1.34-1.32	0.06154	0.07592	0.08922	0.09819	0.05053	0.09893
1.28	0.00687	0.01189	0.00062	0.06018	0.09210	0.01837
1.2	0.00000	0.00102	0.00000	0.00000	0.00036	0.00391
0.96-0.93	0.01063	0.00937	0.00575	0.01267	0.01019	0.00843
0.9	0.00314	0.00772	0.00036	0.00864	0.00446	0.00431

A.3 Graphs for Correlations of Spectral Intensities and CaE% determined by QIAP in 34 Additional Regions of Interest

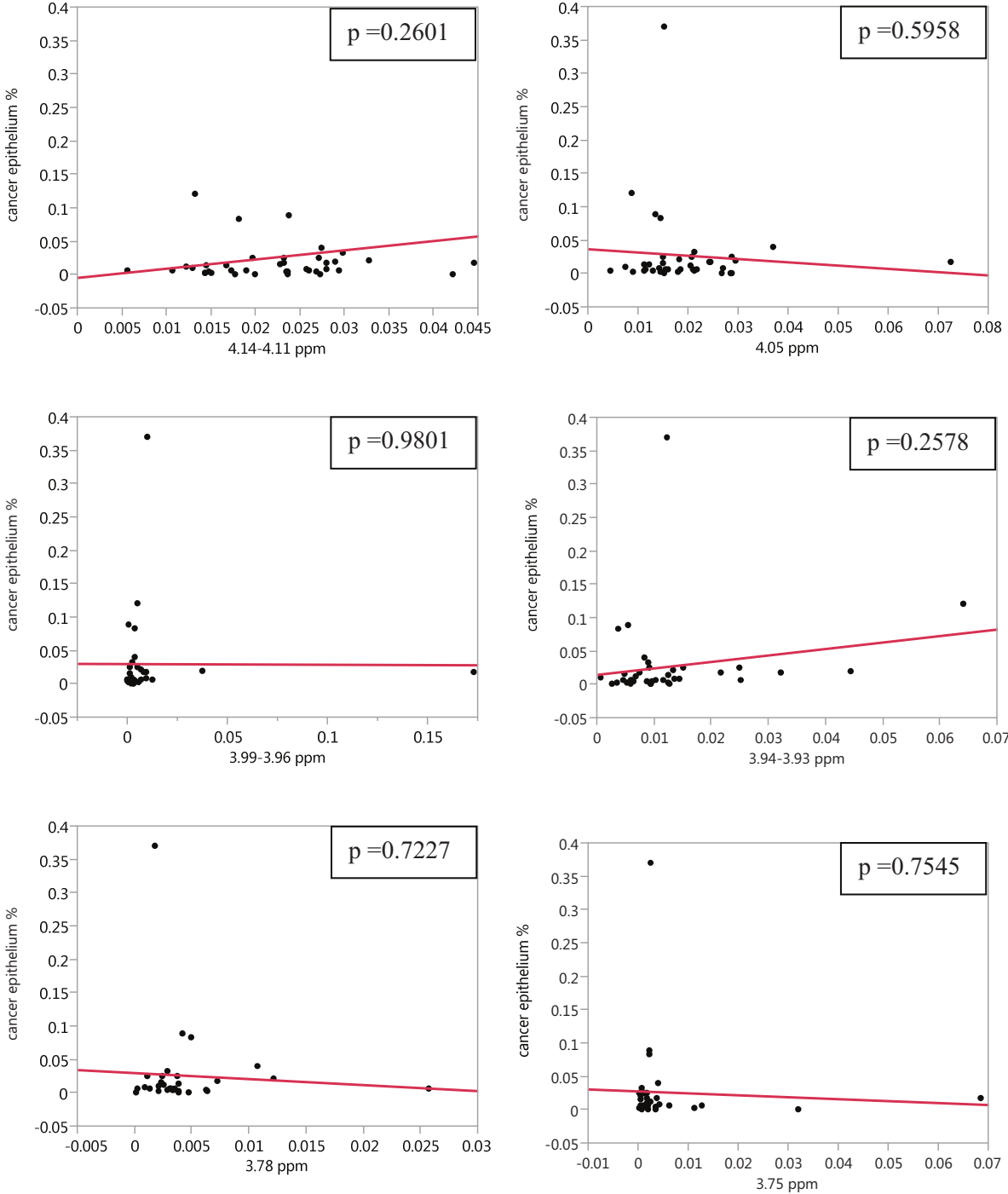


Figure A1: Graphs depicting the non-significant correlations of relative spectral intensities in regions 4.14 – 4.11 ppm ($p = 0.2601$), 4.05 ppm ($p = 0.5958$), 3.99-3.96ppm ($p = 0.9801$), 3.94 – 3.93 ppm ($p = 0.2578$), 3.78 ppm ($p = 0.7227$) and 3.75 ppm ($p = 0.7545$)

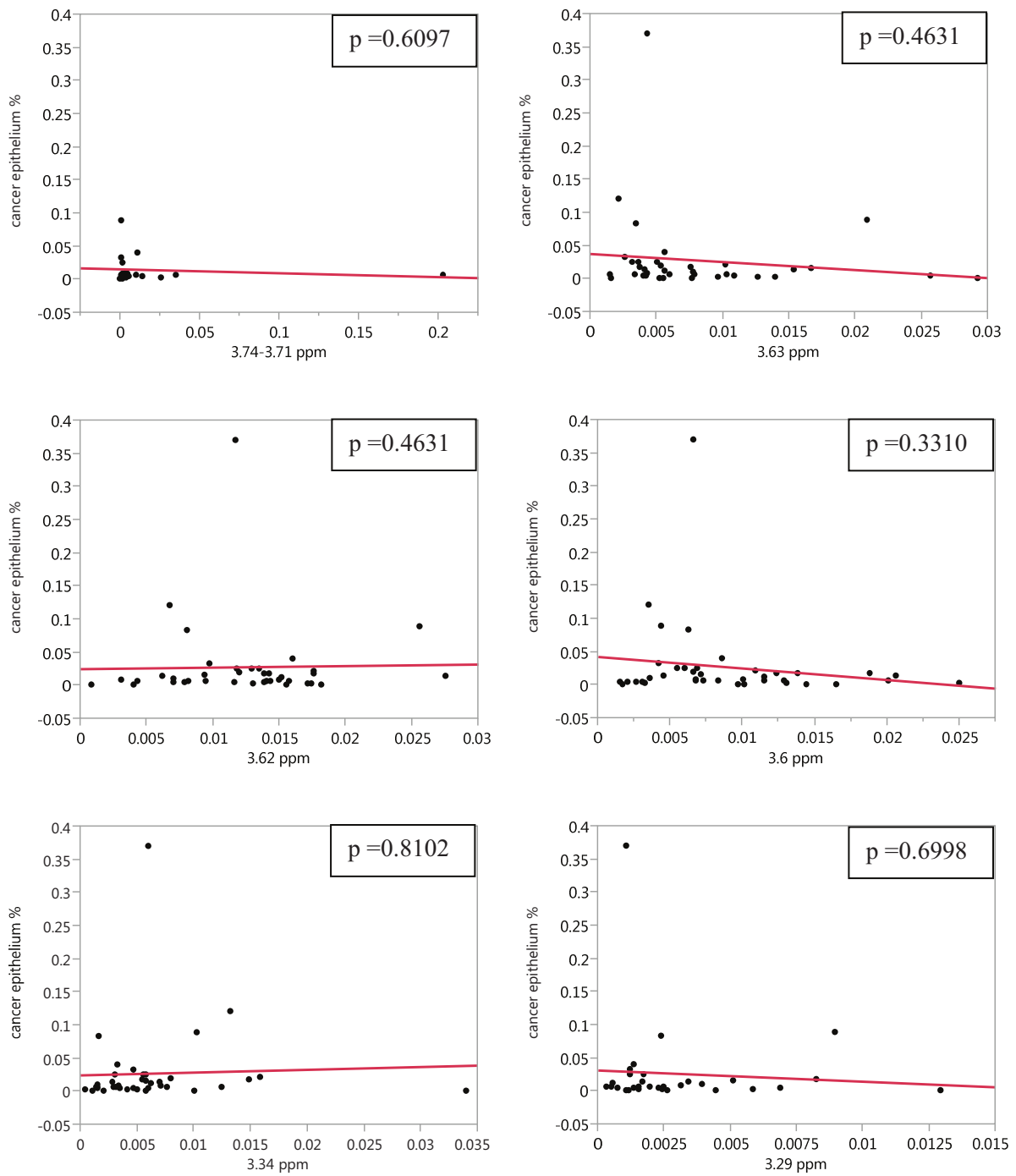


Figure A2: Graphs depicting the non-significant correlations of relative spectral intensities in regions 3.74 – 3.71 ($p = 0.6097$), 3.63 ppm ($p = 0.4631$), 3.62 ppm ($p = 0.4631$), 3.6 ppm ($p = 0.3310$), 3.34 ppm ($p = 0.8102$) and 3.29 ppm ($p = 0.6998$)

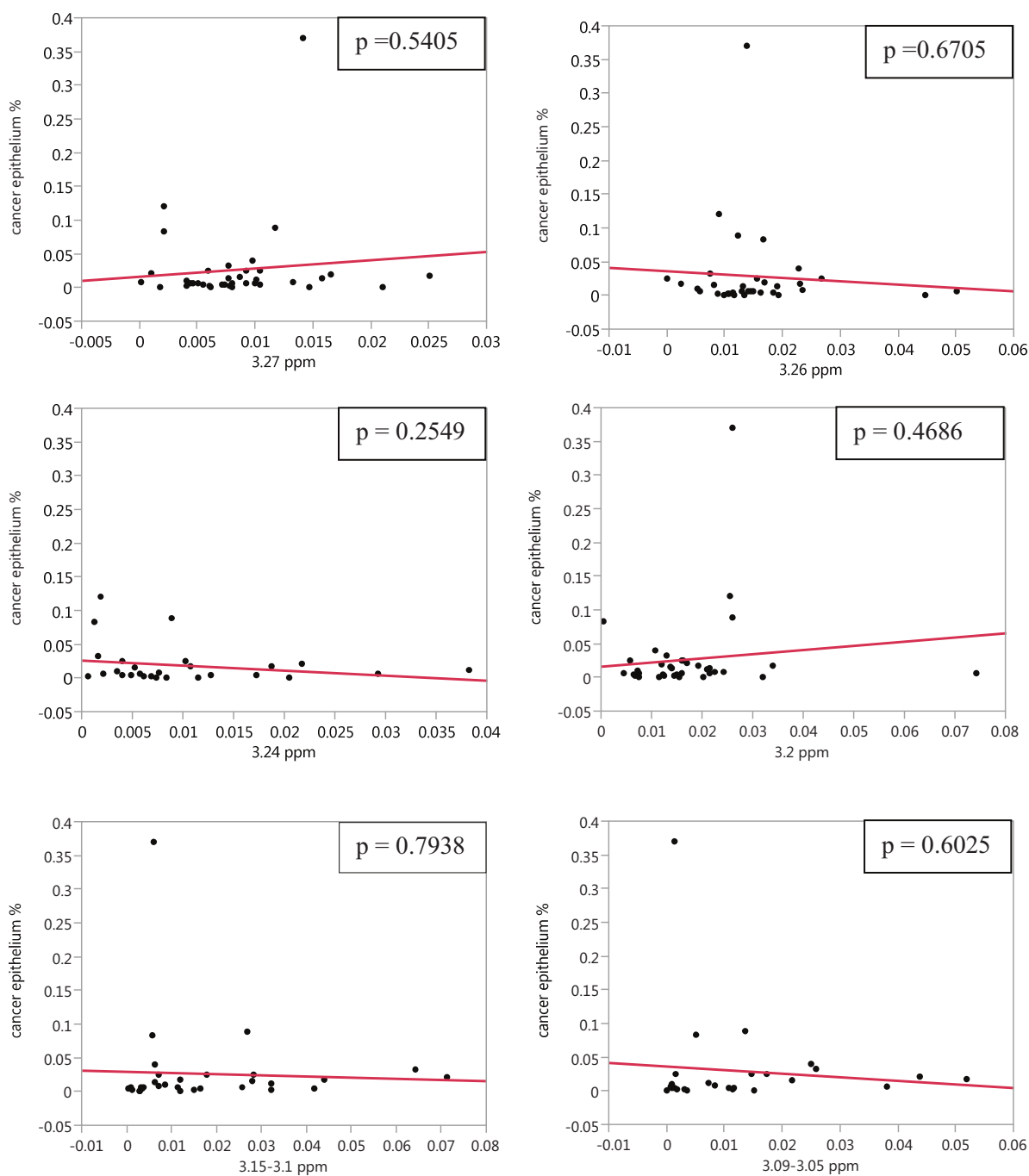


Figure A3: Graphs depicting the non-significant correlations of relative spectral intensities in regions 3.27 ppm ($p = 0.5405$), 3.26 ppm ($p = 0.6705$), 3.24 ppm ($p = 0.2549$), 3.2 ppm ($p = 0.4686$), 3.15 – 3.1 ppm ($p = 0.7938$) and 3.09 – 3.05 ppm ($p = 0.6025$)

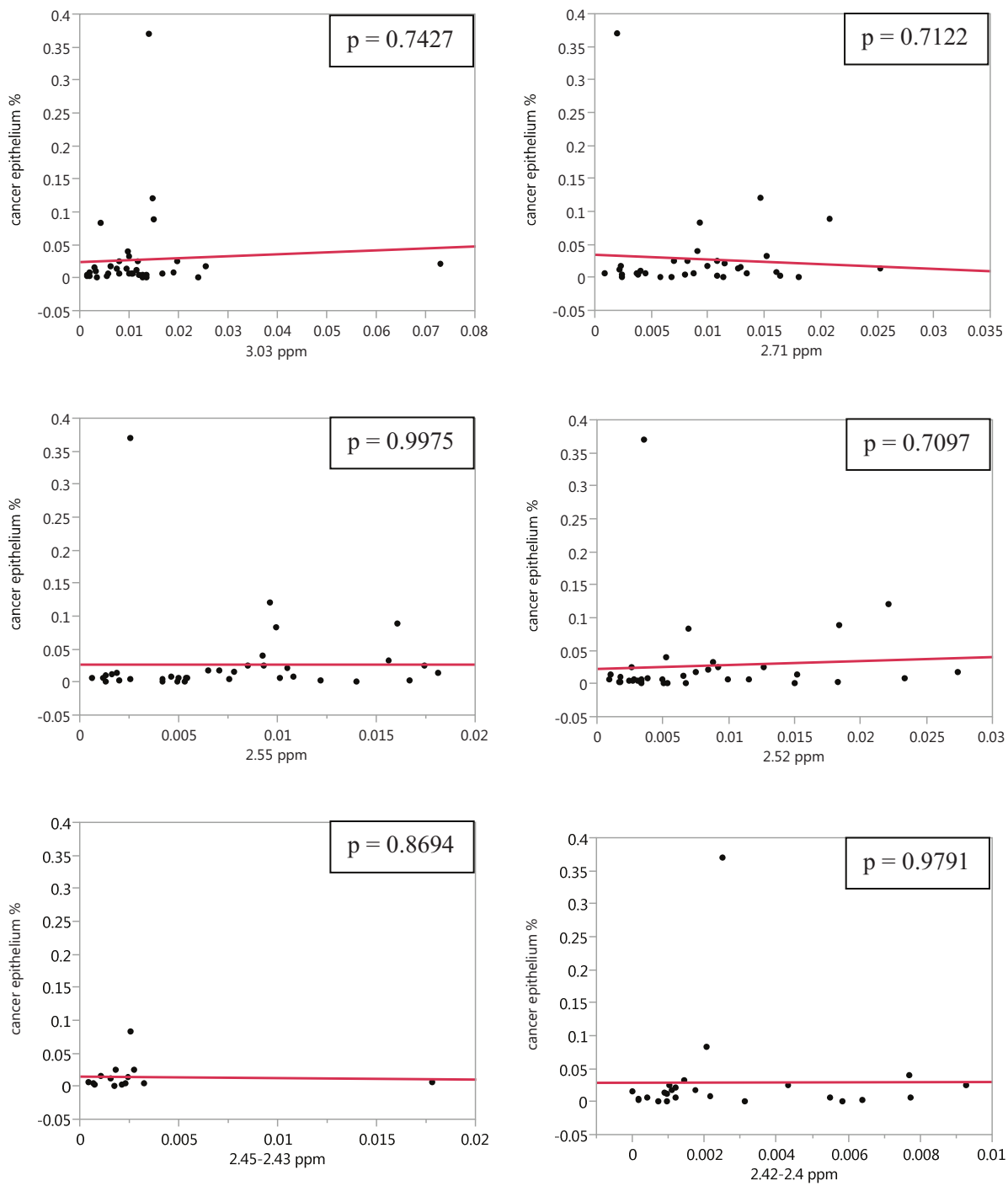


Figure A4: Graphs depicting the non-significant correlations of relative spectral intensities in regions 3.03 ppm ($p = 0.7427$), 2.71 ppm ($p = 0.7122$), 2.55 ppm ($p = 0.9801$), 2.52 ppm ($p = 0.2578$), 2.45 – 2.43 ppm ($p = 0.7227$) and 2.42 – 2.4 ppm ($p = 0.7545$)

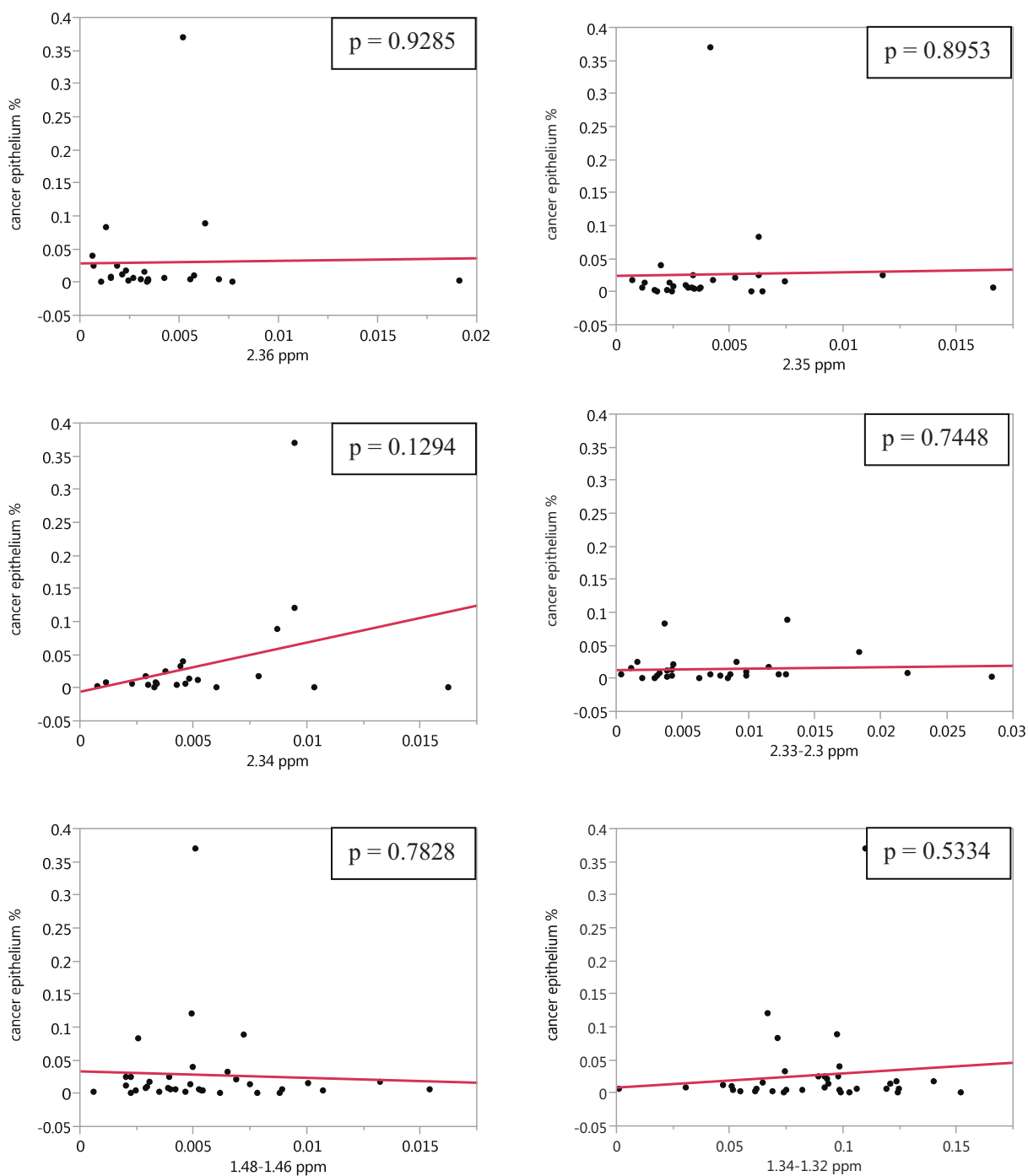


Figure A5: Graphs depicting the non-significant correlations of relative spectral intensities in regions 2.63 ppm ($p = 0.9285$), 2.35 ppm ($p = 0.8953$), 2.34 ppm ($p = 0.1294$), 2.33 – 2.3 ppm ($p = 0.7448$), 1.48 – 1.46 ppm ($p = 0.7828$) and 1.34 – 1.32 ppm ($p = 0.5334$)

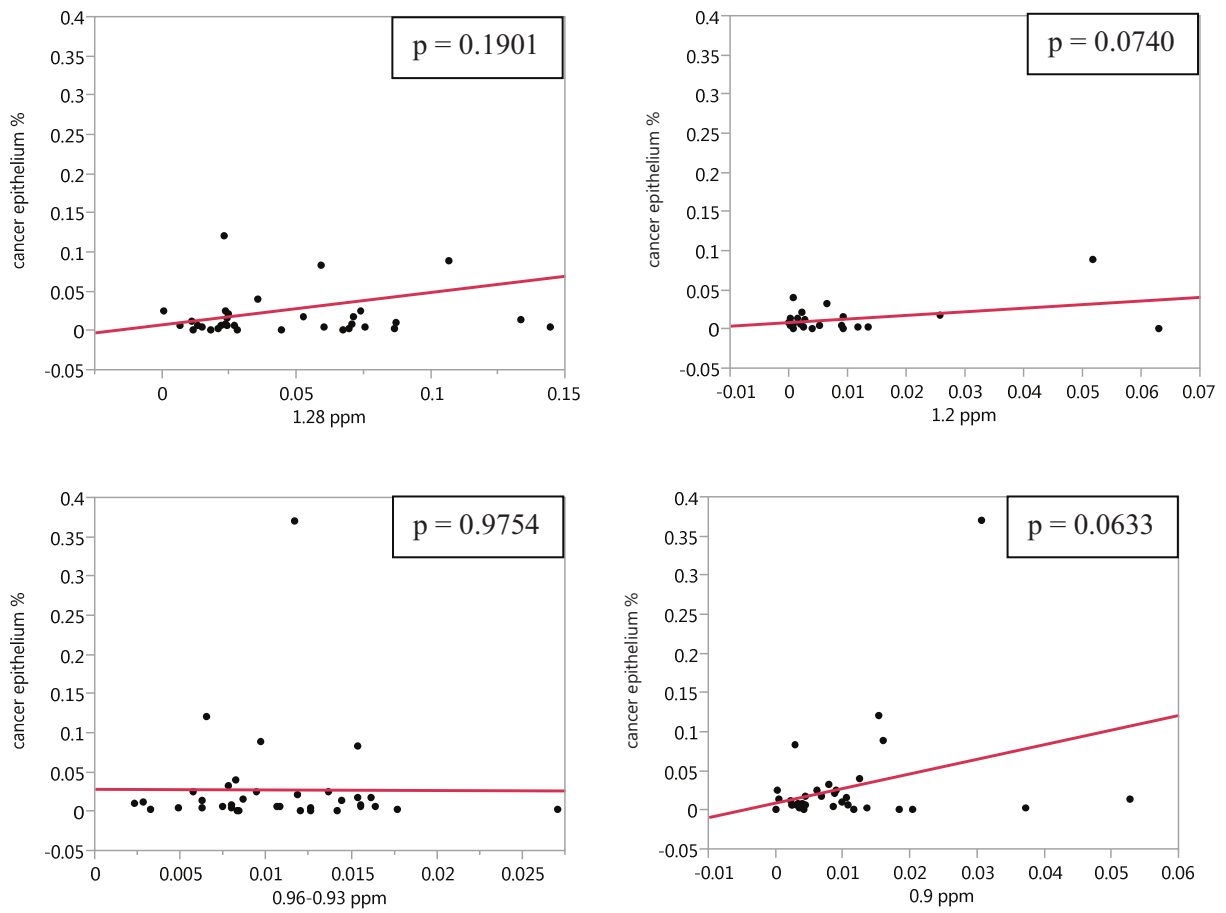


Figure A6: Graphs depicting the non-significant correlations of relative spectral intensities in regions 1.28 ppm ($p = 0.1901$), 1.2 ppm ($p = 0.0740$), 0.96 – 0.93 ppm ($p = 0.9754$), and 0.9 ppm ($p = 0.0633$)